University of Illinois at Urbana-Champaign

ACRC

Air Conditioning and Refrigeration Center A National Science Foundation/University Cooperative Research Center

An Experimental Investigation of Pressure Drop and Heat Transfer in an In-Tube Condensation System of Pure Ammonia

J. E. Vollrath, P. S. Hrnjak, and T. A. Newell

ACRC CR-51 October 2003

For additional information:

Air Conditioning and Refrigeration Center
University of Illinois
Mechanical & Industrial Engineering Dept.
1206 West Green Street
Urbana, IL 61801

(217) 333-3115

The Air Conditioning and Refrigeration Center was founded in 1988 with a grant from the estate of Richard W. Kritzer, the founder of Peerless of America Inc. A State of Illinois Technology Challenge Grant helped build the laboratory facilities. The ACRC receives continuing support from the Richard W. Kritzer Endowment and the National Science Foundation. The following organizations have also become sponsors of the Center.

Alcan Aluminum Corporation
Amana Refrigeration, Inc.
Arçelik A. S.
Carrier Corporation
Copeland Corporation
Dacor
Daikin Industries, Ltd.
Delphi Harrison Thermal Systems
Embraco S. A.
General Motors Corporation
Hill PHOENIX
Honeywell, Inc.
Hydro Aluminum Adrian, Inc.
Ingersoll-Rand Company
Kelon Electrical Holdings Co., Ltd.
Lennox International, Inc.
LG Electronics, Inc.
Modine Manufacturing Co.
Parker Hannifin Corporation
Peerless of America, Inc.
Samsung Electronics Co., Ltd.
Sanyo Electric Co., Ltd.
Tecumseh Products Company
The Trane Company
Visteon Automotive Systems
Wieland-Werke, AG
Wolverine Tube, Inc.

For additional information:

Air Conditioning & Refrigeration Center
Mechanical & Industrial Engineering Dept.
University of Illinois
1206 West Green Street
Urbana, IL 61801

217 333 3115

Abstract

Pressure drop and heat transfer measurements were taken for smooth and internally enhanced aluminum test sections using pure R22 and ammonia. Two-phase condensation tests were conducted in the horizontally-oriented test sections. Inside diameters for the two test sections were measured at 7.52 mm (0.3”). The test conditions included mass fluxes from 20 to 270 kg/m^2-s (15 to 199 klbm/ft^2-hr), inlet qualities of 0 to 95%, and test section heat fluxes from 2.0 to 10.0 kW/m^2 (635 to 3175 Btu/ft^2-hr). The majority of the two-phase experiments were run at an inlet temperature of 35 °C (95 °F) with a few points taken at saturation temperatures of 40 – 53 ºC (104 – 127 °F).

The data is compared to pressure drop and heat transfer correlations to help explain the characteristics of the two test sections. Experimental data showed an average increase of pressure drop by a factor of 1.4 for the enhanced test section regardless of mass flux or quality. Heat transfer data showed a decreased heat transfer coefficient in the enhanced test section. When coupled with the area enhancement, the enhanced test section performed much worse when compared to the basic or smooth test section.

Acknowledgement

This work has been supported by ASHRAE TC1.3; Project 1207-TRP

Table of Contents

List of Figures

Page

List of Tables

Page

Nomenclature

A	Area (m^2)
C_p	Specific Heat (kJ/kg-K)
D	Diameter (m)
EF	Enhancement Factor
e/d	Roughness Ratio
f	Single Phase Friction Factor
G	Mass Flux (kg/m^2s)
g	Gravitational Constant (9.81 m/s^2)
h	Enthalpy (kJ/kg)
h	Heat Transfer Coefficient (kW/m^2-K)
h_F	Fin Height (m)
h_l	Liquid Pool Height (m)
h_{lv}	Latent Heat (kJ/kg)
j_v	Superficial Vapor Velocity (m/s)
k	Conductivity (W/m-K)
L	Length (m)
$\dot{m}$	Mass Flow Rate (kg/s)
P	Pressure (kPa)
P_{red}	Reduced Pressure
PF	Penalty Factor
q''	Heat Flux (kW/m^2)
$\dot{Q}$	Heat Transfer Rate (kW)
S	Slip Ratio
u	Horizontal Velocity Component (m/s)
V	Fluid Velocity (m/s)
x	Quality
z	Distance (m)

Greek Symbols

α	Void Fraction
ß	Helical Fin Angle (radians)
Δ	Change
δ	Liquid Film Thickness (m)
ε	Effective Surface Roughness (m)
Φ	Two Phase Multiplier
?	Specific Volume (m^3/kg)
μ	Viscosity (kg/ms)
ρ	Density (kg/m^3)
σ	Surface Tension (N/m)
τ_w	Perimeter Average Shear Stress (Pa)
?	Stratification Angle (radians)

Dimensionless Parameters

Bo	Boiling Number
Fr	Froude Number
Fr_{so}	Soliman Froude Number
F_{td}	Taitel-Dukler Froude Number
Ga	Galileo Number
Ja	Jakob Number
J_G	Dimensionless Vapor Velocity
Nu	Nusselt Number
Re	Reynolds Number
Pr	Prandtl Number
We	Weber Number
X_{tt}	Lockhart-Martinelli Parameter

Subscripts

2ϕ	Two Phase
a	Accelerational
cw	Cold Water
eq	Equivalent
f	Frictional
g	Gravitational
i	Inlet
l	Laminar
l	Liquid
lo	Liquid Only
o	Outlet
PH	Preheater
refr	Refrigerant
sat	Saturation
sub	Subcooled
t	Turbulent
tp	Two Phase
ts	Test Section
v	Vapor
vo	Vapor Only
w	Wall
x	Generic Subscript

Chapter 1. Introduction

The purpose of this project is to examine the behavior (pressure drop, heat transfer coefficient) of pure ammonia under condensation conditions. This study, supported by the American Society of Heating, Refrigerating, and Air Conditioning Engineers, is motivated by the desire to explore the advantages and disadvantages of environmentally friendly refrigerants. In the recent past, an industry driven push has been made to find and characterize 'natural' refrigerants. Examples of the natural refrigerants include carbon dioxide, propane and other hydrocarbons, and ammonia. Potential advantages for using ammonia as a refrigerant are increased refrigerant side heat transfer, reduced refrigerant side pressure drop and its natural existence (environmentally friendly). Disadvantages for using ammonia include its flammability, toxicity at relatively low levels, and its harsh incompatibility with copper.

Two different aluminum test sections are investigated using two refrigerants, R22 and ammonia. The tubes used are a smooth tube and a microfin tube. The microfin tube is an axially enhanced tube (helix angle of 0^o) with 60 fins placed circumferentially around the tube. The tubes both have nominal outside diameter of 9.52 mm (3/8") with nominal internal diameters of 7.52mm (0.3"). The enhanced tube has approximately 2.2 times the surface area of the basic tube.

This document is divided into seven chapters. Chapter 2 discusses the pertinent literature regarding two-phase condensation flow. Chapter 3 details the experimental facilities and measurement techniques. Chapter 4 examines the heat transfer coefficient data gathered on R22. Chapters 5 and 6 will present the ammonia heat transfer coefficient and pressure drop data, respectively. Chapter 7 offers a brief summary of the report.

Chapter 2. Literature Review

This chapter discusses the pertinent literature relating to the condensation heat transfer and pressure drop of ammonia in small tubes. The goal of this chapter is to provide sufficient insight into the theoretical aspects necessary for understanding the results. Included in this section are discussions about several dimensionless parameters used throughout this thesis, two-phase flow regimes, pressure drop models and heat transfer models.

2.1 Two Phase Flow Parameters

The dimensionless parameters used most frequently in the various correlations listed in this chapter appear in Table 2.1. These two-phase fluid parameters are often a simple variation of the parameters used for single-phase flow (Reynolds Number, Nusselt Number, Prandtl Number, etc.). Parameters that appear infrequently in this manuscript are listed with the correlation they are used with and are given a special subscript to alleviate any confusion with those listed in Table 2.1.

2.2 Void Fraction Review

The void fraction is not directly measured in the present research investigation; however, it is a parameter that is often required for the calculation of pressure drop and heat transfer coefficients. A review of refrigerant void fraction (a) in smooth tubes appear in the UIUC ACRC technical reports by Graham et al. (1998), Kopke et al. (1998), Wilson et al. (1998) and Yashar et al. (1998). These reports all refer to the work published by Rice (1987) which reviewed several void fraction models found in the open literature. Only one model by Zivi (1964), will be presented here.

Zivi (1964) developed a model that was categorized by Rice as being of the slip velocity ratio form. Correlations that fall into this category are typically of the following form:

$$\alpha = \frac{1}{1+\left(\frac{1-x}{x}\right)\left(\frac{\rho_v}{\rho_l}\right)\cdot S} \tag{2.1}$$

where S is the slip ratio. In a physical sense, the slip ratio is the ratio of vapor velocity to liquid velocity. Zivi derived a model based on the assumption that in a steady state thermodynamic process, the rate of entropy production is minimized. Zivi assumed that the flow was steady and annular, and the wall friction was negligible. Zivi did not account for liquid entrainment. Using these assumptions, Zivi found the slip ratio to be

$$S = \left(\frac{\rho_l}{\rho_v}\right)^{\frac{1}{3}} \tag{2.2}$$

and the void fraction can be calculated by

$$\alpha = \frac{1}{1+\left(\frac{1-x}{x}\right)\left(\frac{\rho_v}{\rho_l}\right)^{\frac{2}{3}}} \tag{2.3}$$

Many other void fraction models are also based on the determination of a slip ratio parameter. Sometimes, the slip ratio is a function of other factors such as Reynolds number. In other models, a slip ratio does not explicitly appear in the void fraction, but it is still an inherent parameter of void fraction models.

2.3 Pressure Drop Models

The pressure drop of a two phase flow is comprised of three different factors: frictional, accelerational, and gravitational terms.

$$\left(\frac{\mathrm{dP}}{\mathrm{dz}}\right)_{\mathrm{tp}} = \left(\frac{\mathrm{dP}}{\mathrm{dz}}\right)_{\mathrm{f}} + \left(\frac{\mathrm{dP}}{\mathrm{dz}}\right)_{\mathrm{a}} + \left(\frac{\mathrm{dP}}{\mathrm{dz}}\right)_{\mathrm{g}} \tag{2.4}$$

In horizontal tube studies, the gravitational pressure drop is ignored. The accelerational portion relates to the pressure change caused when the fluid undergoes a change in quality in either condensation or evaporation. If the void fraction is known, a momentum balance can be used to calculate this accelerational term.

$$\left(\frac{dP}{dz}\right)_a = -\frac{G^2}{L}\left[\left\{\frac{x_o^2}{r_v a_o} + \frac{(1-x_o)^2}{r_l(1-a_o)}\right\} - \left\{\frac{x_i^2}{r_v a_i} + \frac{(1-x_i)^2}{r_l(1-a_i)}\right\}\right] \tag{2.5}$$

The frictional component can be calculated using a two-phase multiplier F_x proposed by Lockhart and Martinelli (1949). Lockhart and Martinelli defined two-phase multipliers that related the actual two-phase fractional pressure gradient to single-phase pressure gradients. The following equations show these two-phase multipliers

$$\left(\frac{dP}{dz}\right)_f = \Phi_l^2\left(\frac{dP}{dz}\right)_l \tag{2.6a}$$

$$\left(\frac{dP}{dz}\right)_f = \Phi_v^2\left(\frac{dP}{dz}\right)_v \tag{2.6b}$$

$$\left(\frac{dP}{dz}\right)_f = \Phi_{lo}^2\left(\frac{dP}{dz}\right)_{lo} \tag{2.6c}$$

$$\left(\frac{dP}{dz}\right)_f = \Phi_{vo}^2\left(\frac{dP}{dz}\right)_{vo} \tag{2.6d}$$

where *l* is for liquid, *v* for vapor, *lo* for liquid only, or *vo* for vapor only. These single-phase pressure drops can be calculated by the following

$$\left(\frac{\mathrm{dP}}{\mathrm{dz}}\right)_{\mathrm{l}} = -\frac{2\mathrm{f}_{\mathrm{l}}(1-\mathrm{x})^2\mathrm{G}^2}{\rho_{\mathrm{l}}\mathrm{D}} \tag{2.7a}$$

$$\left(\frac{\mathrm{dP}}{\mathrm{dz}}\right)_{\mathrm{v}} = -\frac{2\mathrm{f}_{\mathrm{v}}(\mathrm{xG})^2}{\rho_{\mathrm{v}}\mathrm{D}} \tag{2.7b}$$

$$\left(\frac{\mathrm{dP}}{\mathrm{dz}}\right)_{\mathrm{lo}} = -\frac{2\mathrm{f}_{\mathrm{lo}}\mathrm{G}^2}{\rho_{\mathrm{l}}\mathrm{D}} \tag{2.7c}$$

$$\left(\frac{dP}{dz}\right)_{vo} = -\frac{2f_{vo}G^2}{\rho_v D} \tag{2.7d}$$

The single-phase friction factor (f) can be calculated by either

$$f = 0.079\,Re^{-0.25} \tag{2.8a}$$

or

$$f = 0.046\,Re^{-0.2} \tag{2.8b}$$

where the Reynolds number (Re) is defined by

$$Re_l = \frac{G(1-x)D}{\mu_l} \tag{2.9a}$$

$$Re_v = \frac{GxD}{\mu_v} \tag{2.9b}$$

$$Re_{lo} = \frac{GD}{\mu_l} \tag{2.9c}$$

$$Re_{vo} = \frac{GD}{\mu_v} \tag{2.9d}$$

Incropera and Dewitt (1996) reports that equation 2.8a is preferred for flows with $Re<2\cdot10^4$ and 2.8b when $Re>2\cdot10^4$. Wilson (2001) reports that equation 2.8a is usually used with f_{lo} and f_{vo}, while equation 2.8b is usually used with f_l and f_v. Other friction factor models may also be used for the single phase pressure drop correlations as well. All of the literature that was researched for this section uses the liquid only pressure drop as a basis for the two phase pressure drop multiplier, so the ensuing discussion will be limited to the equations relevant for liquid only analysis.

2.3.1 Round Smooth Tube Correlations

The majority of the existing correlations refer back to the work by Lockhart and Martinelli (1949). Lockhart and Martinelli studied the two phase flow of air with the following fluids: benzene, kerosene, water and oils in tubes with diameters ranging from 1.4 mm to 25.8 mm. They observed that four types of flow could exist depending on the flow pattern (laminar or turbulent) of both the liquid and vapor phase. Lockhart and Martinelli furthered their work by developing four separate correlations, one for each of these flow patterns. The basis for this correlation is a two-phase pressure drop parameter X which is defined as the square root of the ratio between vapor pressure drop to liquid pressure drop.

$$X = \frac{\Phi_v^2}{\Phi_l^2} \tag{2.10}$$

It was found that for each flow type X reduces to a ratio of phase flow rates and properties.

$$X_{ll} = \left(\frac{1-x}{x}\right)^{0.5}\left(\frac{\rho_v}{\rho_l}\right)^{0.5}\left(\frac{\mu_l}{\mu_v}\right)^{0.5} \tag{2.11a}$$

$$X_{lt} = 18.65\left(\frac{1-x}{x}\right)\left(\frac{\rho_v}{\rho_l}\right)^{0.5}\frac{Re_v^{0.1}}{Re_l^{0.5}} \tag{2.11b}$$

$$X_{tl} = \frac{1}{18.65}\left(\frac{1-x}{x}\right)\left(\frac{\rho_v}{\rho_l}\right)^{0.5}\frac{Re_v^{0.5}}{Re_l^{0.1}} \tag{2.11c}$$

$$X_{tt} = \left(\frac{1-x}{x}\right)^{0.9}\left(\frac{\rho_v}{\rho_l}\right)^{0.5}\left(\frac{\mu_l}{\mu_v}\right)^{0.1} \tag{2.11d}$$

The first subscript is for the liquid and the second for the vapor phase. Here *l* represents the laminar flow regime, while *t* represents the turbulent flow regime. X_{tt} is the commonly used parameter for refrigerant flows since it is generally assumed that both phases are indeed turbulent.

Friedel (1979) developed a very unique two-phase pressure drop correlation based on his studies which included data from experiments with water, R12, air-water, and air-oil mixtures. Results were gathered in horizontal flow as well as vertical up and vertical down flows. The test specimens used in this study included the standard circular tube as well as a rectangular and an annular tube. For horizontal flow, Friedel found that the two-phase multiplier depended on the density, viscosity, and single phase only friction factors, as well as the quality. In addition to these terms, Friedel developed his correlation to be a function of the two-phase Froude and Weber numbers.

$$\Phi_{lo}^{\ 2} = C_1 + \frac{3.24C_2}{Fr^{0.045}We^{0.035}} \tag{2.12}$$

$$C_1 = (1-x)^2 + x^2\left(\frac{r_l}{r_v}\right)\left(\frac{f_{vo}}{f_{lo}}\right) \tag{2.13}$$

$$C_2 = x^{0.78}(1-x)^{0.224}\left(\frac{\rho_l}{\rho_v}\right)^{0.91}\left(\frac{\mu_v}{\mu_l}\right)^{0.19}\left(1-\frac{\mu_v}{\mu_l}\right)^{0.7} \tag{2.14}$$

where the two-phase Froude and Weber numbers are defined as

$$Fr = \frac{G^2}{\rho_{2\phi}^{\ 2}Dg} \tag{2.15}$$

$$We = \frac{G^2D}{\rho_{2\phi}\sigma} \tag{2.16}$$

$$r_{2f} = \frac{r_l r_v}{x r_l + (1-x) r_v} \tag{2.17}$$

Friedel's correlation defines the friction factors used in equations 2.13 as follows:

$$f_{xo} = \frac{16}{Re_x} \tag{2.18}$$

$$f_{xo} = 0.25\left[0.86859\ln\left(\frac{\mathrm{Re}_x}{1.964\ln(\mathrm{Re}_x) - 3.8215}\right)\right]^{-2} \tag{2.19}$$

Equation 2.18 is used for flows of $Re_x<1055$ while equation 2.19 is used for flows with $Re_x>1055$. The subscript *x* is used here to specify the phase of interest and should be changed to *l* or *v* for actual implementation of this correlation.

Jung and Radermacher (1989) developed a correlation based on their experimental results of various two-phase flows. Jung and Radermacher analyzed the mixtures which included the refrigerants R12, R22, R114 and R152a. As a result of their work, Jung and Radermacher found no dependence on composition and that the following two-phase multiplier sufficiently predicted their experimental data.

$$\Phi_{lo}^{\ 2} = 12.82 X_{tt}^{\ -1.47}(1-x)^{1.8} \tag{2.20}$$

Souza et. al. (1993) conducted pressure drop tests on R12 and R134a with and without oil. In Souza's experiments the oil concentration was varied from 0% to 5% by weight. Both a PAG and an ester oil were used with R134a, while a mineral oil was utilized with R12. Adiabatic tests were run at a saturation temperature of 5 ºC with a mass flux ranging form 200-600 kg/m^2-s. A copper tube with an internal diameter of 10.9 mm (0.43 in) was used as the test specimen. From the experimental data gathered in this study, Souza determined that the two-phase multiplier to be a function of both X_{tt} and the liquid Froude Number Fr_l. Souza uses the Froude Number to distinguish between different flow regimes.

$$\Phi_{lo}^{\ 2} = \left(1.376 + c_1 X_{tt}^{\ -c_2}\right)(1-x)^{1.75} \tag{2.21}$$

$$c_1 = \begin{cases} 4.172 + 5.480\mathrm{Fr}_l - 1.564\mathrm{Fr}_l^{\ 2} & (0 < \mathrm{Fr}_l \le 0.7) \\ 7.242 & (\mathrm{Fr}_l > 0.7) \end{cases} \tag{2.22}$$

$$c_2 = \begin{cases} 1.773 - 0.169\mathrm{Fr}_l & (0 < \mathrm{Fr}_l \le 0.7) \\ 1.655 & (Fr_l > 0.7) \end{cases} \tag{2.23}$$

$$\mathrm{Fr}_l = \frac{\mathrm{G}^2}{\rho_l^{\ 2}\mathrm{gD}} \tag{2.24}$$

Souza et. al. (1993) somewhat altered the Lockhart-Martinelli parameter for their correlation.

$$X_{tt} = \left(\frac{1-x}{x}\right)^{0.875}\left(\frac{r_v}{r_l}\right)^{0.5}\left(\frac{m_l}{m_v}\right)^{0.125} \tag{2.25}$$

2.3.2 Micofin Tube Correlations

Cavallini et. al. (1999) developed a correlation from a pool of data. This pool of data consists of experimental data gathered on various fluids in different sized tubes throughout a number of diverse labs around the world. The basis of this study was to develop a correlation that is not biased from lab to lab, but rather all including in terms of fluid types and tube sizes. Cavallini et. al. (1999) developed a relation for e/d, the roughness ratio, used in calculating a rough tube friction factor. Cavallini recommends using this rough tube friction factor in conjunction with the Friedel correlation.

$$\frac{e}{d} = 0.18\left(\frac{h_F}{D}\right)\left(\frac{1}{0.1+\cos\beta}\right) \qquad (2.26)$$

In the above equation (2.26), h_F is the fin height and ß the fin helix angle (0 for axial grooved tubes).

Nozu et. al. (1998) analyzed pressure drop data on R11 gathered in two different microfin tubes. They discovered that along with fin geometry, X_{tt} and void fraction the two-phase multiplier was also a function of the heat transfer rate.

2.3.3 Comparison of Pressure Drop Models

Figures 2.1 and 2.2 show how the predicted correlations of Friedel, Jung and Radermacher, and Souza compare to one another. Figure 2.1 depicts the three different correlations trends in predicting the pressure drop of ammonia at a flow rate of G=80 kg/m^2-s. Figure 2.2 shows how the three correlations predict the pressure drop of ammonia at a flow rate of G=270 kg/m^2-s. These two plots show that the Jung and Radermacher correlation tends to be the high end of the three, while the Souza predicts at the low end. The correlation developed by Friedel predicts pressure drop in between the Souza and Jung and Radermacher.

2.4 Two Phase Flow Regimes

Flow patterns or flow regimes are a very important characteristic of two-phase fluid flow and are linked to the mechanisms of pressure drop and heat transfer. Flow patterns describe how the liquid and vapor fractions of a two-phase flow position themselves in relation to each other. Several flow patterns can exist in condensation and can be affected by flow rates, physical properties of the two phases, and the geometry of the tube. The most pertinent flow regimes include stratified flow, wavy flow, annular flow, mist flow, and slug-plug flow. Figure 2.3 illustrates these typical flow patterns.

2.4.1 Flow Characteristics

The flow regimes listed in Figure 2.3 can be divided up into two groups: those at high void fractions and those at low void fractions. The first category includes the regimes of importance in horizontal condensation flow. In this category, the flow regimes are arranged such that each successive flow regime corresponds to an increase in vapor velocity. At low mass fluxes and qualities a stratified flow regime is observed. In stratified flow, the liquid portion flows along the bottom of the tube at relatively low velocities, while the vapor portion travels above the liquid, at the top of the tube at higher velocities. Stratified flow often resembles that seen in a sewage pipe. As mass flux and quality increase, (also leading to an increase in void fraction) the liquid vapor interface becomes unstable allowing surface waves to form. Still as mass flux and quality increase, these waves begin to wash up along the circumference but not fully wetting the entire tube surface. This is the wavy annular flow regime. In stratified and wavy flows heat transfer is mainly governed by the gravitational forces due to the large liquid layer at the bottom of the tube. The annular flow regime occurs when the liquid pool spreads out more evenly around the tube perimeter creating a liquid ring around the circumference with a vapor core. This occurs at even higher mass fluxes and qualities than the wavy annular flow regime. Continuing down Figure 2.3, the last flow regime in this category is called annular-mist. This occurs at high vapor velocities which shear off the crests of the waves along

this liquid ring. These liquid droplets then become entrained in the vapor core. The dominating heat transfer mechanism of the annular and misty flow patterns is the vapor shear throughout the core.

The second category of flow regimes includes the slug, plug, and bubbly flow regimes. In this category the flow regimes are arranged with respect to void fraction. As void fraction decreases, the liquid portion of the flow continues to grow until it effectively floods the entire cross section of the tube with vapor pockets on either side. As void fraction continues to decrease, the vapor pockets shrink until the turbulence of the liquid portion shear or break up these vapor pockets into much smaller vapor bubbles which are dispersed throughout the tube. This is considered bubbly flow, with the intermediary portion between slug and bubbly being the plug flow regime.

2.4.2 Flow Regime Maps

Because of the strong influence flow patterns have on the mechanisms of heat transfer and pressure drop it was desirable to create flow maps that predict the pattern of the flow. Several of these maps exist. Baker (1954) designed the first known method. Air-water and oil-water flows were examined in 25 mm – 100 mm (1" – 4") tubes. Baker plotted a scaled quantity of both the liquid and vapor mass fluxes on the horizontal and vertical coordinate respectively. Although Baker's map today is not as accurate as others, it is still of great importance for understanding the first step in flow mapping.

Mandhane (1974) expanded on Baker's map by analyzing a much larger test matrix. Mandhane used air-water in 25 mm-100 mm tubes. Mandhane did however change the axes from superficial mass fluxes to superficial velocities. In an extensive condensation study completed by Wattelet (1994), Mandhane's map appeared to have systematic problems when applied to refrigerant data in small diameter tubes. Wattelet suggested that this error was due to the much higher vapor density of a refrigerant when compared to air. Dobson (1994) and Dobson and Chato (1998) witnessed the same error as Wattelet. To account for this they used a correction factor based on the square root of the density ratio that seemed to significantly improve the accuracy of the map.

Taitel and Dukler (1976) developed a map based on a theoretical approach. They reasoned that different forces acting on the flow lead to the different flow regimes. Taitel and Dukler defined five regimes in their map including stratified, stratified-wavy, annular, slug-plug, and bubbly. Originally the map was developed for adiabatic flows, but studies completed by Barnhart (1992) and Wattelet (1994) show that the map performed fairly well under both evaporation and condensation.

Taitel and Dukler use the turbulent Lockhart-Martinelli parameter (X_{tt}) for the abscissa and what they defined to be a Taitel-Dukler Froude Number (F_{td}) for the ordinate.

$$F_{td} = \sqrt{\frac{\rho_v}{\rho_l - \rho_v}} \frac{Gx/\rho_v}{\sqrt{Dg \cdot \cos(\theta)}} \tag{2.27}$$

Taitel and Dukler determined that the transition from stratified-wavy to an intermittent or annular flow occurred at the following:

$$F_{td}^2 \left[\frac{1}{\left(1-\tilde{h}_l\right)^2} \frac{\tilde{u}_v \sqrt{1-\left(2\tilde{h}_l - 1\right)^2}}{\tilde{A}_v} \right] \geq 1 \tag{2.28}$$

$$\tilde{h}_l = \frac{h_l}{D} \tag{2.29}$$

$$\tilde{A}_v = \frac{A_v}{D^2} \tag{2.30}$$

$$\tilde{u}_v = \frac{u_v}{j_v} = \frac{1}{\alpha} \tag{2.31}$$

Here, h_l is the liquid height, j_v is the superficial vapor velocity, and A_v is the vapor area, which can be calculated by using geometrical relations if the void fraction (a) is known.

Soliman (1982) believed that the transition between wavy-stratified and annular was based on a balanced between inertial and gravitational forces on the liquid film. The dimensionless Froude number represents this balance.

$$Fr = \frac{V^2}{gL} \tag{2.32}$$

Soliman developed inequalities using his own very unique Froude number to determine this transition.

$$Fr_{so} = 0.025\,Re_l^{1.59}\left(\frac{1+1.09X_{tt}^{0.039}}{X_{tt}}\right)^{1.5}\frac{1}{Ga^{0.5}} \qquad \text{for } Re_l = 1250 \tag{2.33}$$

$$Fr_{so} = 1.26\,Re_l^{1.04}\left(\frac{1+1.09X_{tt}^{0.039}}{X_{tt}}\right)^{1.5}\frac{1}{Ga^{0.5}} \qquad \text{for } Re_l > 1250 \tag{2.34}$$

Soliman concluded that wavy-stratified flow was observed for $Fr_{so}<7$, and annular flow was observed for $Fr_{so}>7$. Dobson et al. (1994) reported that $Fr_{so}=7$ served as a good indicator of the transition between these two regimes, yet a uniform annular flow did not form until $Fr_{so}=18$.

Cavallini, et al. (2002) developed a flow map to be used with his two-phase condensation heat transfer model. Cavallini sought out to develop an 'all inclusive' flow map. To accomplish this, he explored visual observation data gathered from five different independent laboratories using various fluids in a number of different sized tubes. From these studies, Cavallini developed a flow map that positioned the dimensionless two-phase flow multiplier X_{tt} on the horizontal axis and the dimensionless vapor velocity J_G on the vertical axis.

$$J_G = \frac{x \cdot G}{[g \cdot d \cdot \rho_v(\rho_l - \rho_v)]^{0.5}} \tag{2.35}$$

Based on these parameters, Cavallini mapped out the following flow regimes: annular flow, transition and wavy-stratified flow, and stratified-slug flow. Cavallini concluded that annular flow existed when $J_G>2.5$, the transition region occurred when $J_G<2.5$ and $X_{tt}<1.6$, and the stratified-slug regime appears when $J_G<2.5$ with $X_{tt}>1.6$. Figure 2.4 illustrates the layout of this flow map.

Thome, et al. (2003) developed a flow map to be used in conjunction with a two-phase condensation heat transfer model. Based on an earlier evaporation flow map developed by Thome et al. (2002), Thome defines the vertical axis as simply being the mass flux G (kg/m^2-s) and the horizontal axis as the vapor quality. Using a void

fraction approach, Thome defines individual mass flux lines separating the different flow regimes. Thome prescribes five different flow patterns: stratified, stratified-wavy, intermittent, annular, and misty flow. Figures 2.5 to 2.8 show the configurations of this map for ammonia at different mass fluxes. Four maps are listed because Thome's map is a function of void fraction which is a function of mass flux (G). Therefore, Thome's map is a function of mass flux itself and the individual mass flux lines separating the different flow regimes changes depending on refrigerant mass flux.

2.5 Heat Transfer Models

Over the years several heat transfer correlations have been developed to characterize the condensation of various fluids. As discussed in section 2.4, the stratified and annular flow regimes typically dominate the flow pattern. Although the flow will experience other regimes such as mist or intermittent flow, the actual length of the tube/condenser where this occurs is small relative to the length of both the annular and stratified regimes. Therefore, correlations were designed to specifically predict the heat transfer in those regimes. Of importance is a set of three different classifications of correlations: stratified flow only, annular flow only, and a combination of stratified-annular flow.

2.5.1 Stratified Flow Smooth Tube Correlations

Chato (1962) completed one of the earliest studies of condensation focusing on stratified flow at low vapor velocities. Chato chose to concentrate on the thin liquid film at the sides of the tubes by assuming that the heat transferred by the bulk liquid pool at the bottom of the tube was negligible. From this he developed a similarity solution that was patterned after Chen's (1961) analysis of falling film condensation in a horizontal tube. He adjusted his model to account for the variations in height of the liquid pool. Chato used R113 as the refrigerant for both his experimental and analytical model. He found that his model reasonably predicted his heat transfer data.

$$Nu = 0.555\left(\frac{\rho_l(\rho_l-\rho_v)gh_{lv}D^3}{k_l\mu_l(T_{sat}-T_w)}\right)^{0.25} = 0.555\left(\frac{Ga_D\,Pr_l}{Ja}\right)^{0.25} \qquad (2.36)$$

The coefficient of 0.555 is 76% of the value of 0.728 which is accepted for external condensation on a cylinder (Incropera & Dewitt equation 10.40).

Jaster and Kosky (1976) proposed a stratified flow only correlation similar to that of Chato. Jaster and Kosky used Zivi's void fraction term to account for variations of height in the liquid pool. They proposed the following correlation:

$$Nu = 0.728\alpha^{0.75}\left(\frac{\rho_l(\rho_l-\rho_v)gh_{lv}D^3}{k_l\mu_l(T_{sat}-T_w)}\right)^{0.25} = 0.728\alpha^{0.75}\left(\frac{Ga_D\,Pr_l}{Ja}\right)^{0.25} \qquad (2.37)$$

Like Chato's correlation, Jaster and Kosky choose to ignore the heat transferred from the liquid pool. This assumption was determined to be valid for low speed stratified flows, but may not be accurate at higher speed flows. To account for this possibility, Rosson and Meyers (1965) collected heat transfer data in stratified, wavy, and slug-plug flow regimes. Rosson and Meyers collected temperature measurements circumferentially along the outside of the tube. This was done to better understand the how different mechanisms (i.e. film condensation, vapor shear,

etc.) affect the heat transfer. Rosson and Meyers formed a correlation that predicted a different Nusselt number for both the top and bottom of the tube.

$$Nu_{top} = 0.31 Re_v^{0.12} \left(\frac{\rho_l (\rho_l - \rho_v) g h_{lv} D^3}{k_l \mu_l (T_{sat} - T_w)} \right)^{0.25} = 0.31 Re_v^{0.12} \left(\frac{Ga_D \, Pr_l}{Ja} \right)^{0.25} \quad (2.38)$$

$$Nu_{bot} = \frac{\phi_{l,lt} \sqrt{8 Re_l}}{5 \left(1 + \frac{\ln[1 + 5 Pr_l]}{Pr_l} \right)} \quad (2.39)$$

$$\phi_{l,lt} = \sqrt{1 + \frac{1}{X_{lt}} + \frac{12}{X_{lt}^2}} \quad (2.40)$$

They then developed a function to determine the fraction over which each condensation mechanism occurred.

$$Nu = \varepsilon Nu_{top} + (1 - \varepsilon) Nu_{bot} \quad (2.41)$$

$$\varepsilon = Re_v^{0.1} \quad \text{if} \ \frac{Re_v^{0.6} \, Re_l^{0.5}}{Ga} < 6.4 x 10^{-5} \quad (2.42a)$$

$$\varepsilon = \frac{1.74 \cdot 10^{-5} Ga}{\sqrt{Re_v \, Re_l}} \quad \text{if} \ \frac{Re_v^{0.6} \, Re_l^{0.5}}{Ga} > 6.4 x 10^{-5} \quad (2.42b)$$

Rosson and Myers compared their predicted values to their own experimental data for acetone and methanol. They found that their correlation worked well in predicting the heat transfer values.

2.5.2 Annular Flow Smooth Tube Correlations

Numerous models have been developed to predict the heat transfer characteristics during annular flow condensation. Most of these models fall under one of three different categories. These categories of interest include (1) two-phase multiplier approaches, (2) shear-based approaches, and (3) boundary-layer approaches.

2.5.2.1 Two Phase Flow Multiplier Correlations

Perhaps the easiest method to implement, two-phase multiplier correlations represent the first subset of the annular condensation heat transfer models. These correlations generally consist of slight modifications made to the single phase Dittus-Boelter (1930) correlation.

$$Nu = 0.023 \cdot Re^{0.8} \, Pr^n \quad (2.43)$$

The Akers et. al. (1959) correlation was one of the first to implement this modified single phase correlation to predict two phase annular flow. Akers developed a model that would replace the vapor core with an equivalent single-phase liquid flow that had the same pressure drop. To achieve the same pressure drop, Akers used an equivalent mass flux G_{eq} that resulted in an equivalent Reynolds number.

$$G_{eq} = G \left[(1 - x) + x \left(\frac{\rho_l}{\rho_v} \right)^{0.5} \right] \quad (2.44)$$

$$Re_{eq} = \frac{G_{eq} D}{\mu_l} \tag{2.45}$$

These equivalent parameters are then used in the Dittus-Boelter single-phase heat transfer equation.

$$Nu = 0.0265 \cdot Re_{lo,eq}^{0.8} \, Pr_l^{0.333} \tag{2.46}$$

The most widely cited correlation of the two-phase multiplier type is the Shah (1979) correlation. Shah modified the Dittus-Boelter correlation by introducing the two-phase multiplier term in terms of the reduced pressure.

$$Nu = 0.023 Re_l^{0.8} \, Pr_l^{0.4} \left[1 + \frac{3.8}{P_{red}^{0.38}} \left(\frac{x}{1-x} \right)^{0.76} \right] \tag{2.47}$$

Shah compared this correlation with data from the open literature for refrigerants, water, methanol, benzene, toluene, trichloroethylene, and ethanol. He found that the mean deviation of his correlation with the experimental points was 17%.

Due to the wide variety of fluids used to generate Shah's correlation, Bivens and Yokozeki (1994) set out to modify Shah's for just refrigerants. Bivens and Yokozeki modified Shah's by using a slight mass flux adjustment.

$$h = h_{Shah} \cdot BY \tag{2.48}$$

$$BY = .078438 + 6187.89 / G^2 \tag{2.49}$$

The mass flux (G) must be in kg/m^2s.

Tang (1997) studied the condensation heat transfer coefficients for refrigerants R22, R134a, and the newer R410A. Tang found that the model developed by Shah was not able to accurately predict the annular heat transfer coefficients of R410A. To account for this, Tang set out to simply modify the correlation by Shah. The following is the correlation developed by Tang:

$$Nu = 0.023 Re_l^{0.8} \, Pr_l^{0.4} \left[1 + 4.863 \left(-\ln(P_{red}) \frac{x}{1-x} \right)^{0.836} \right] \tag{2.50}$$

2.5.2.2 Shear Based Correlations

The groundwork for the shear based correlations was laid down by Carpenter and Colburn (1951). They developed a model based on their assumption that the resistance to heat transfer in the turbulent liquid flow was entirely inside the laminar sublayer. From this they devised the following correlation:

$$Nu = b \cdot D^+ \, Pr_l^m \tag{2.51}$$

$$D^+ = \frac{\sqrt{\tau_w / \rho_l} \, D}{\nu_l} \tag{2.52}$$

The constants b and m were empirically determined to be equal to 0.043 and 0.5, respectively.

The work done by Soliman et. al. (1968) showed the inaccuracy in Carpenter and Colburn's calculation for the accelerational shear component. Soliman et al. used several different techniques to correct for this. Due to the length of describing these techniques, they will not be presented here. However, the following correlation is still considered to be an offspring of the work done by Carpenter and Colburn:

$$Nu = 0.036\,Re_{lo}\,Pr_l^{0.65}\left(\frac{\rho_l}{\rho_v}\right)^{0.5}\sqrt{\frac{2(.046)x^2}{Re_v^{0.2}}\phi_v^2 + Bo\sum_{n=1}^{5} a_n\left(\frac{\rho_v}{\rho_l}\right)^{n/3}} \tag{2.53}$$

$$a_1 = x(2-\kappa)-1 \tag{2.54}$$

$$a_2 = 2(1-x) \tag{2.55}$$

$$a_3 = 2(\kappa-1)(x-1) \tag{2.56}$$

$$a_4 = \frac{1}{x} - 3 + 2x \tag{2.57}$$

$$a_5 = \kappa\left(2 - \frac{1}{x} - x\right) \tag{2.58}$$

$$\kappa = 1.25 \tag{2.59}$$

$$Bo = \frac{q''}{Gh_{lv}} \qquad \text{(Boiling Number)} \tag{2.60}$$

$$\phi_v^2 = 1 + 2.85 \cdot X_{tt}^{0.523} \tag{2.61}$$

Soliman et al. compared the predictions of their correlation to experimental data for steam, R-113, R-22, ethanol, methanol, toluene, and trichloroethylene. Their correlation performed adequately predicting the trends, but the deviation between predicted and experimental data was found to be quite large.

Chen et al. (1987) developed a shear based correlation for vertical flow condensation. However, they did state that their correlation would be appropriate for horizontal flow. Based of the model developed by Soliman et al., it appears in equation 2.62.

$$Nu = 0.018\left(\frac{\rho_l}{\rho_v}\right)^{0.39}\left(\frac{\mu_v}{\mu_l}\right)^{0.078} Re_l^{0.2}\left[Re_{lo} - Re_l\right]^{0.7} Pr_l^{0.65} \tag{2.62}$$

2.5.2.3 Boundary Layer Correlations

The most theoretical approach to annular flow condensation is that of the boundary-layer analyses. These analyses represent solutions to simplified forms of the continuity, momentum, and energy equations. Examples of these include Traviss et al. (1973), Cavallini and Zecchin (1974), and Hurlburt and Newell (1999).

To simplify the underlying physics that must be considered to apply a boundary layer approach, an abridged description will be presented. Dobson (1994) elaborates on this, delivering a complete description of the thoughts and ideas behind these schemes. The first step to a boundary layer analysis is determining the void fraction. Once the void fraction is determined, the symmetrical liquid height (h_L) can be found:

$$\alpha = \left(1 - \frac{2h_L}{D}\right)^2 \tag{2.63}$$

Next, the average liquid velocity $(\overline{\mu}_l)$ must be calculated.

$$\dot{m}_l = \rho_l \overline{\mu}_l A_l = (1-\alpha)\rho_l \overline{\mu}_l A_t = (1-x)\dot{m} \tag{2.64}$$

Assuming the 'law of the wall' turbulent boundary layer equations, the average velocity from equation (2.64) must match the average velocity from the 'law of the wall' analysis. This analysis will give the shear stress and then the law of the wall energy equations can be used to find the heat transfer. These models generally lead to a Nusselt number of the form:

$$Nu = \frac{D^+ Pr}{F(Re_L, Pr_L)} \tag{2.65}$$

Traviss et al. (1973) developed the most widely used boundary layer model. Traviss performed condensation experiments with R12 and R22 in a 9.52 mm (0.375") tube. Traviss found that his model showed good agreement with his experimental data.

$$Nu = F(X_{tt})\frac{Pr_l\, Re_l^{0.9}}{F_2} \tag{2.66}$$

$$F(X_{tt}) = 0.15\left[\frac{1}{X_{tt}} + 2.85 \cdot X_{tt}^{-0.476}\right] \tag{2.67}$$

$$F_2 = 0.707 \cdot Pr_l\, Re_l^{0.5} \qquad Re_l<50 \tag{2.68a}$$

$$F_2 = 5 \cdot Pr_l + 5 \cdot \ln\left[1 + Pr_l\left(0.0963 \cdot Re_l^{0.585} - 1\right)\right] \qquad 50<Re_l<1125 \tag{2.68b}$$

$$F_2 = 5 \cdot Pr_l + 5 \cdot \ln(1 + 5 \cdot Pr_l) + 2.5 \cdot \ln\left(0.00313 \cdot Re_l^{0.812}\right) \qquad Re_l>1125 \tag{2.68c}$$

Cavallini and Zecchin (1974) combined the ideas behind the boundary layer schemes with the ease of use of the two-phase multiplier schemes. They used results of a theoretical annular flow analysis to deduce the dimensionless groups need for the two-phase multiplier schemes. Their scheme appears as follows:

$$Nu = 0.023\, Re_l^{0.8}\, Pr_l^{0.33}\left\{2.64\left[1 + \left(\frac{\rho_l}{\rho_v}\right)^{0.5}\left(\frac{x}{1-x}\right)\right]\right\}^{0.8} \tag{2.69}$$

The bracketed term represents the two-phase multiplier. Cavallini and Zecchin compared their correlation with a pool of data that included six different studies with R113, R12, and R22. Although their correlation performed well for some sets of data (standard deviation of 8%), it also showed signs of poor performance in others (standard deviations as high as 47%).

In a study completed by Hurlburt and Newell (1999), a boundary layer scheme was developed out of the 'law of the wall' velocity profile. Hurlburt and Newell assumed an interfacial shear relation to determine the velocity profile in the liquid layer which allowed the void fraction and heat transfer to be determined.

2.5.3 Annular-Stratified Flow Smooth Tube Correlations

In the recent past, several models have been developed to effectively predict heat transfer coefficients in more than one regime. Typically, these models combine both a model for stratified flow with a model for annular flow. Some do however incorporate other flow regimes into their models, such as slug flow and mist flow. This subchapter will discuss models developed by Dobson and Chato (1994), Cavallini, et.al. (2002), and Thome, et.al. (2003).

Dobson and Chato (1994) developed one of the earliest two-phase flow condensation heat transfer model that incorporated multiple flow regimes. To accurately predict flow regimes, Dobson did extensive visualization testing on R12, R22, R134a, and azeotropic blends of R32/R125 in 50%/50% and 60%/40% compositions. Dobson recommended the following flow regimes:

For G=365 klb_m/ft^2-h (495 kg/m^2-s) annular flow existed

For G<365 klb_m/ft^2-h (495 kg/m^2-s) and

Fr_{so}<20 stratified/wavy annular flow existed

Fr_{so}>20 annular flow existed

In the stratified regime, Dobson suggests a revamping of the Rosson-Meyer's correlation:

$$Nu = \frac{0.23\,Re_{vo}^{0.12}}{1+1.11X_{tt}^{0.58}}\left[\frac{Ga\,Pr_l}{Ja_l}\right]^{0.25} + \left(1-\frac{\theta}{\pi}\right)\left(.0195\,Re_l^{0.8}\,Pr_l^{0.4}\,\phi_l\right) \tag{2.70}$$

$$\alpha = \frac{\theta}{\pi} - \frac{\sin(2\theta)}{2\pi} \tag{2.71}$$

where f_l is calculated using the Souza pressure drop equations and a from the Zivi void fraction correlation. In the annular regime, Dobson suggests the following correlation based on a two-phase multiplier approach.

$$Nu = 0.023\,Re_l^{0.8}\,Pr_l^{0.4}\left[1+\frac{2.22}{X_{tt}^{0.889}}\right] \tag{2.72}$$

Using this model, Dobson found his mean deviation to be less than 6.1% for all of his refrigerant heat transfer data.

Cavallini (2002) set out to develop an 'all inclusive' two-phase flow condensation model using a pool of data. This pool of data consists of over 2200 data points collected in nine different labs around the world. Multiple refrigerants were tested including R11, R22, R134a, R410A, R125, R32, R236ea, R407C, R32/R125 (60%/40%) and R404A. The tube diameters ranged from 3.3 mm to 21.4 mm (0.13"-0.84"). The saturation temperatures also varied from 23.7 ºC to 60 ºC (75 ºF-140 ºF), while the temperature difference from the refrigerant to the wall was from 1 ºC to 24.9 ºC (1.9 ºF – 44.8 ºF).

In addition to this heat transfer data, Cavallini wanted to develop a model that would be based on multiple flow regimes. This flow regime model is the basis for his correlation and is described in section (2.4.2). In the annular flow regime, Cavallini suggests using a revamping of the Kosky and Staub (1971) equation with an alternate expression of determining the frictional pressure drop using the Friedel (1979) correlation. In what Cavallini defines as the stratified-slug flow regime, the heat transfer coefficient is calculated with a two-phase flow multiplier equation obtained using a best-fitting procedure of the Dobson and Chato (1998) and Tang (1997) correlations. For

the annular-stratified regime, Cavallini suggests using a linear interpolation between the heat transfer coefficients found in the annular and stratified flow regimes. Due to the extensive nature of this correlation, please reference Cavallini (2002).

In a similar manner, Thome, et.al. (2003) developed a two-phase flow condensation heat transfer model using a massive pool of data. This pool includes tests collected on fifteen fluids (R11, R12, R22, R32, R113, R125, R134a, R236ea, R32/R125 near azeotrope, R404A, R410A, propane, n-butane, iso-butane and propylene) obtained in nine different research laboratories. Accordingly, Thome set out to develop a model that would be based on multiple flow regimes. Thome et al. (2003) developed a unique flow map as discussed in section (2.4.2). In this flow map, he defined three key flow regimes: annular flow, stratified-wavy flow, and fully stratified-wavy flow. Thome used a turbulent film equation to determine the convective heat transfer coefficient found in the annular flow regime. In the fully stratified-wavy and stratified-wavy flow regimes, Thome used the Nusselt falling film theory in conjunction with the convective heat transfer coefficient to determine the overall heat transfer coefficients in these two regimes. An interpolation based on ? (defined as the upper angle of the tube not wetted by stratified liquid) was utilized to distinguish between these two heat transfer coefficients. Due to the extensive nature of this correlation the reader should reference Thome, et.al. (2003).

2.5.4 Comparison of Heat Transfer Models

Figures 2.9 through 2.12 depict how the predicted heat transfer coefficient correlations compare to one another. In particular, the correlations based on multiple flow regimes are presented in Figures 2.9 and 2.11. These multiple flow regime correlations include the Cavallini, Dobson, and Thome. Figures 2.10 and 2.12 show the single flow regime correlations of Chen, Shah, Tang and Traviss. Figures 2.9 and 2.10 show both the multiple and the single flow regime correlations predictions for ammonia at a mass flux (G) of 80 kg/m^2-s. Figures 2.11 and 2.12 show both sets of correlations heat transfer coefficient predictions for ammonia at a mass flux of 270 kg/m^2-s. All seven heat transfer correlations predict relatively close to each other through the range of quality. The Traviss correlation appears to be the most aggressive in predicting ammonia's heat transfer coefficient, while the Chen appears to predict the most conservative of the seven.

2.6 Figures and Tables

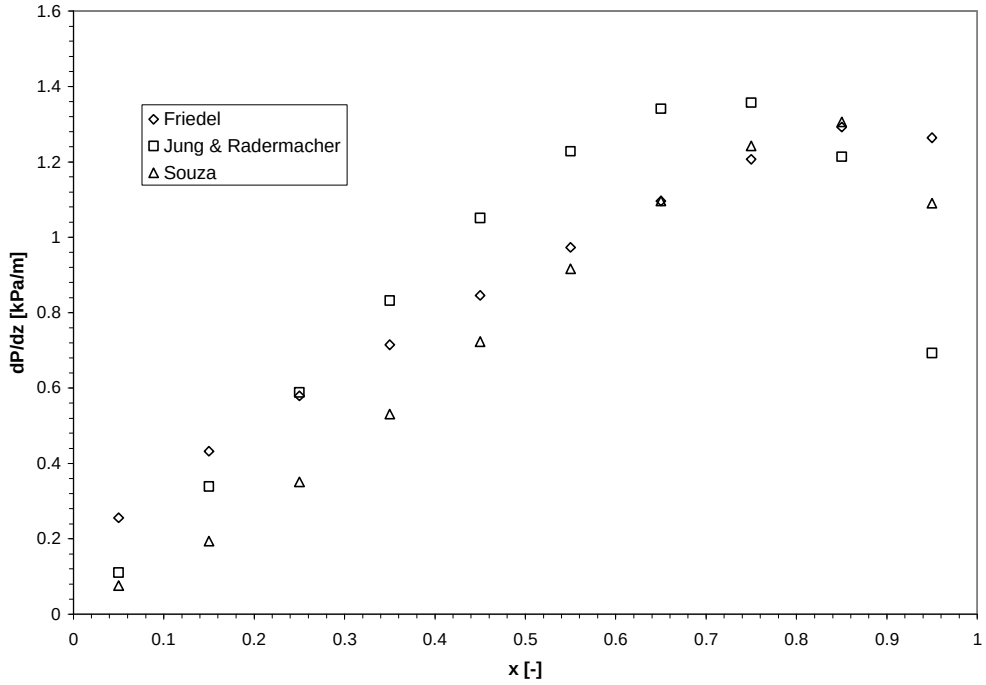

Figure 2.1 Pressure drop correlation comparison for ammonia at G=80 kg/m^2-s

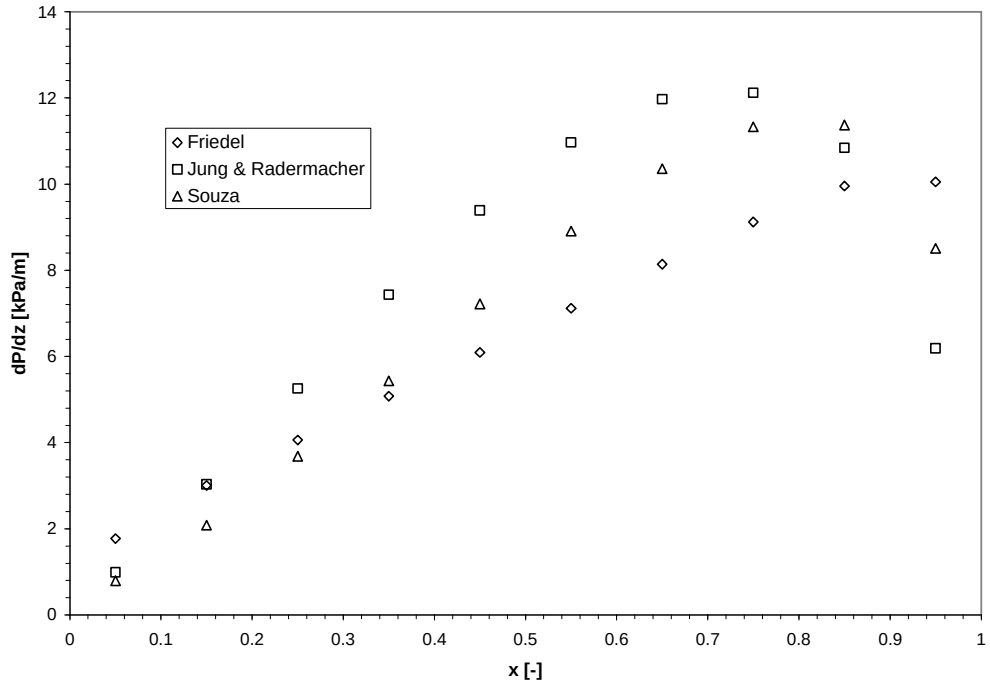

Figure 2.2 Pressure drop correlation comparison for ammonia at G=270 kg/m^2-s

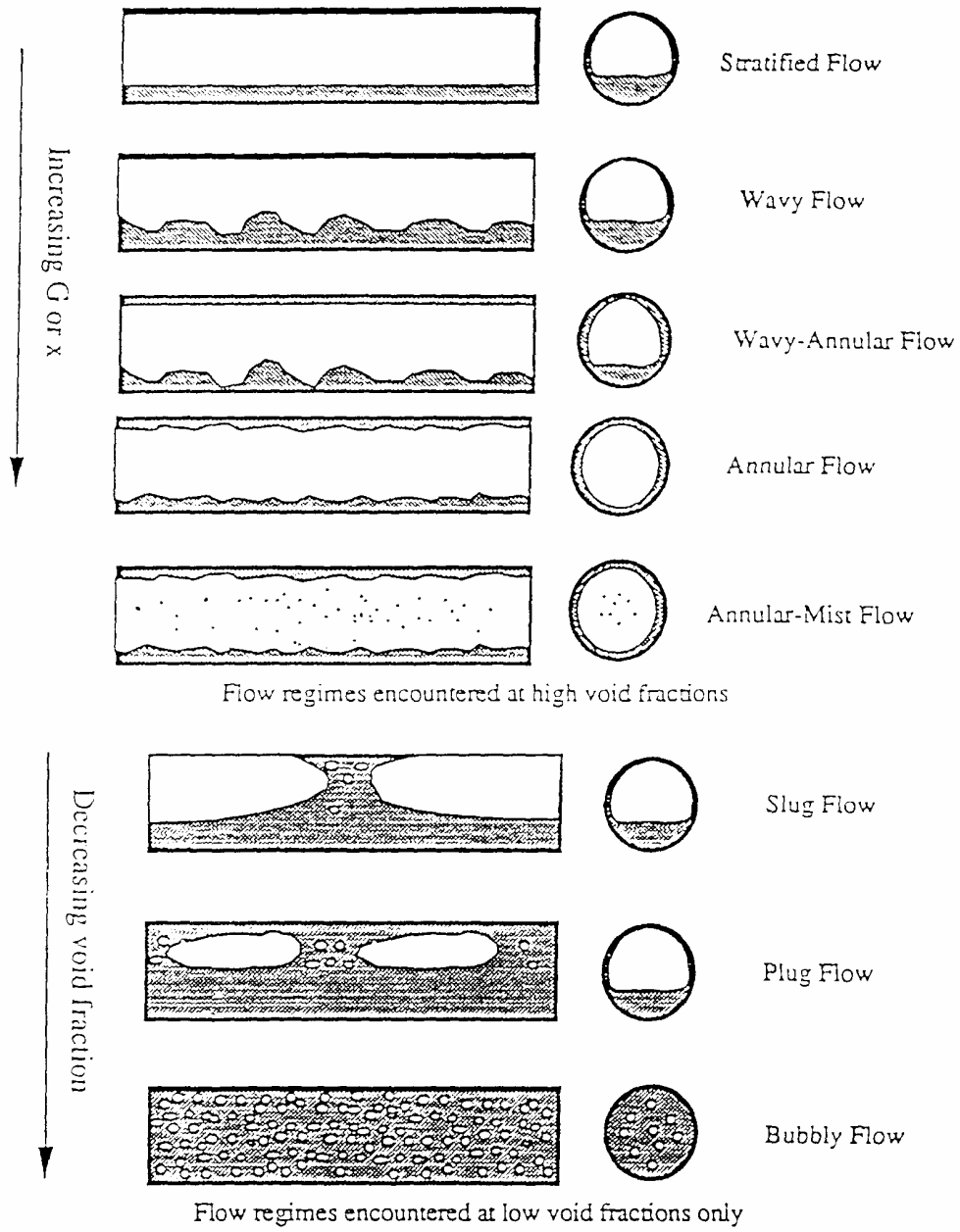

Figure 2.3 Visual maps of different two-phase flow regimes

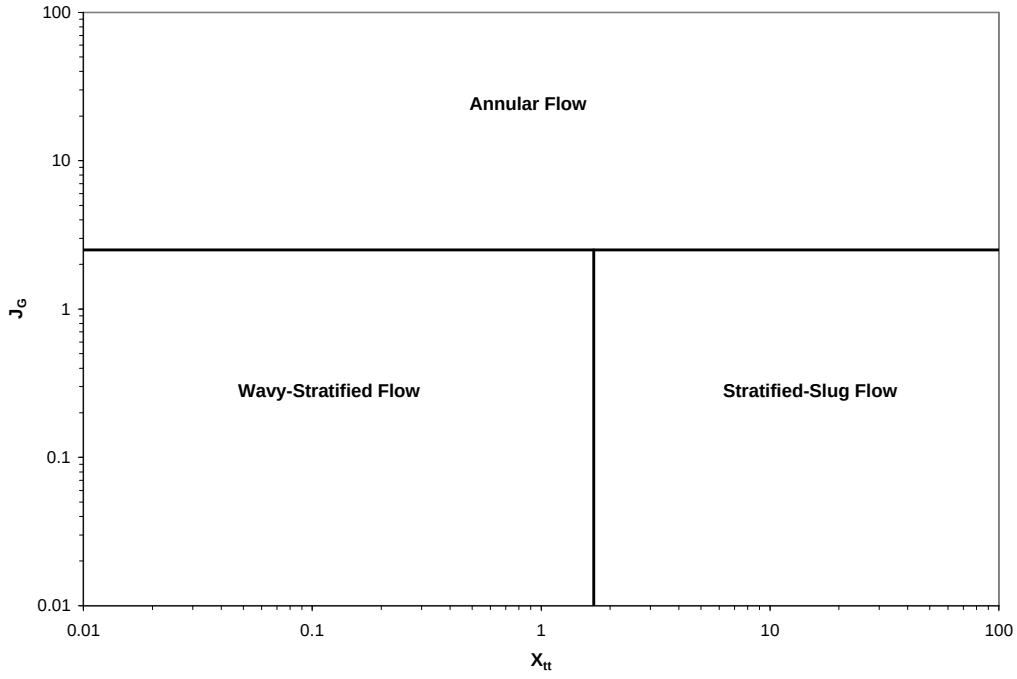

Figure 2.4 Cavallini flow map

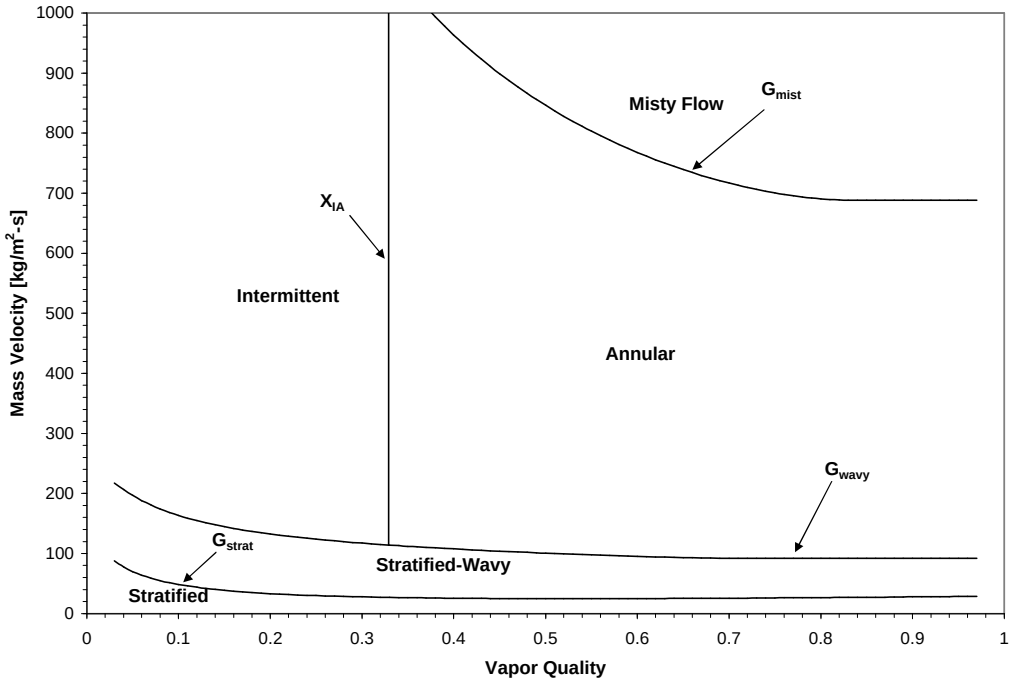

Figure 2.5 Thome flow map for ammonia at G=20 kg/m^2-s

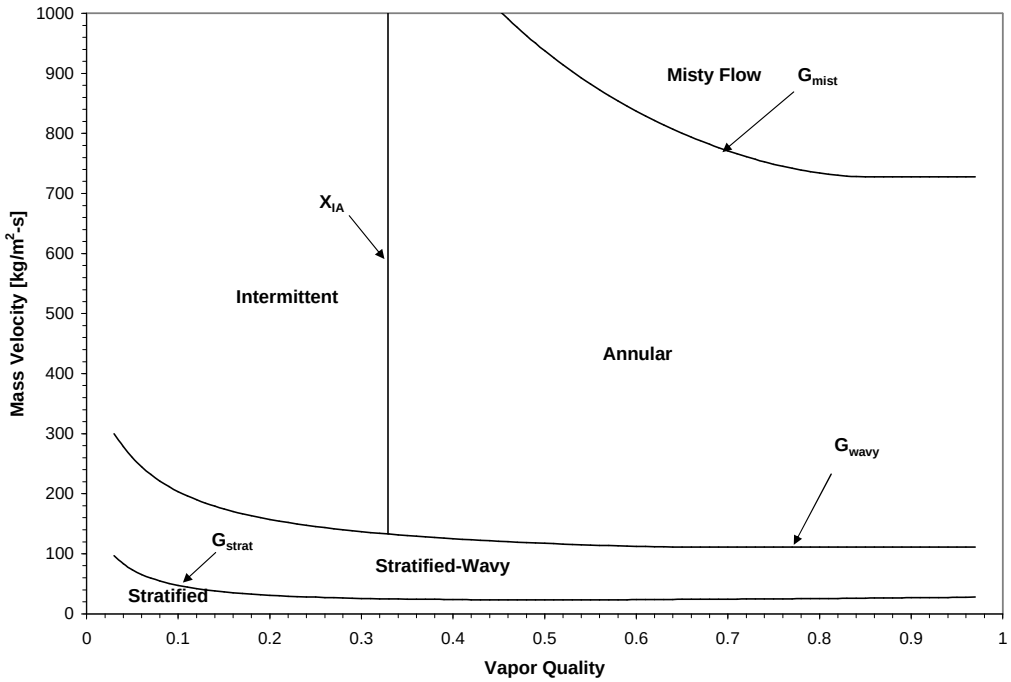

Figure 2.6 Thome flow map for ammonia at G=80 kg/m^2-s

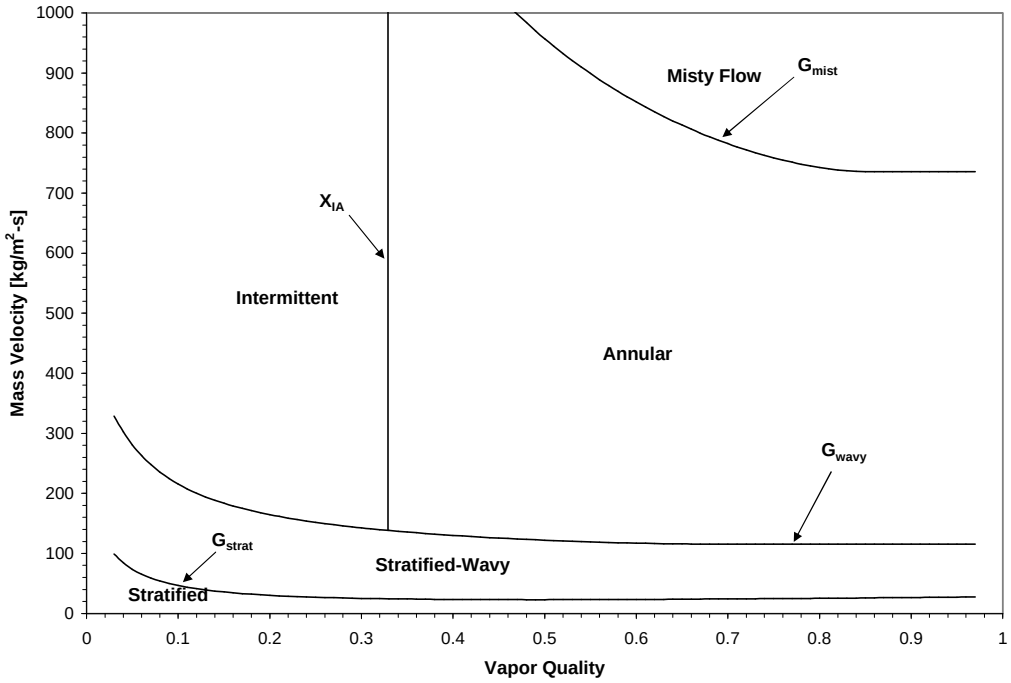

Figure 2.7 Thome flow map for ammonia at G=160 kg/m^2-s

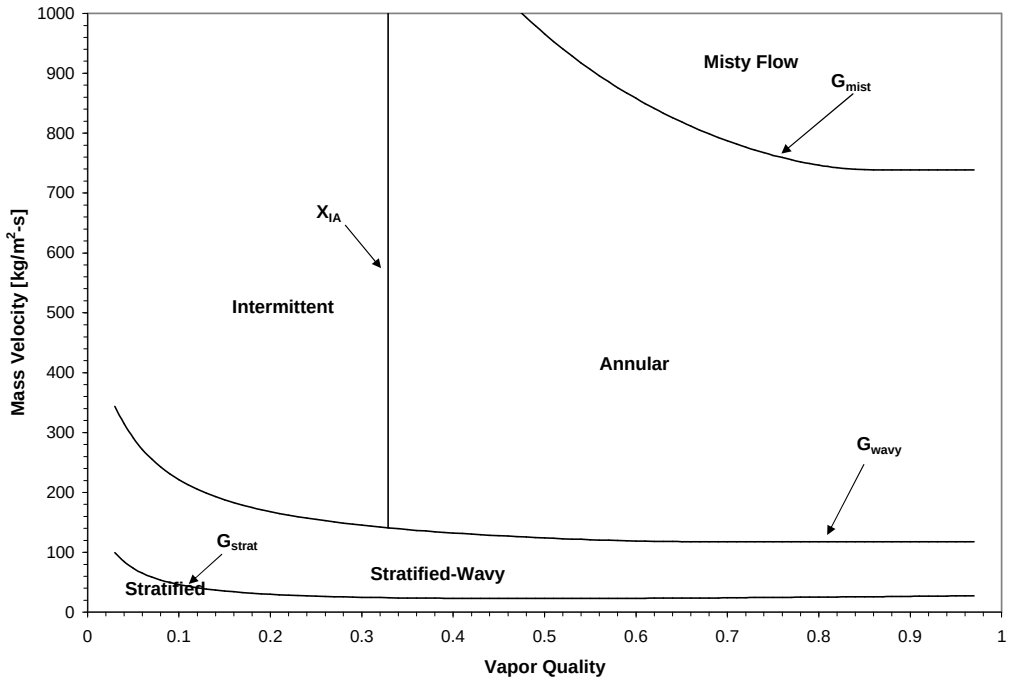

Figure 2.8 Thome flow map for ammonia at G=270 kg/m^2-s

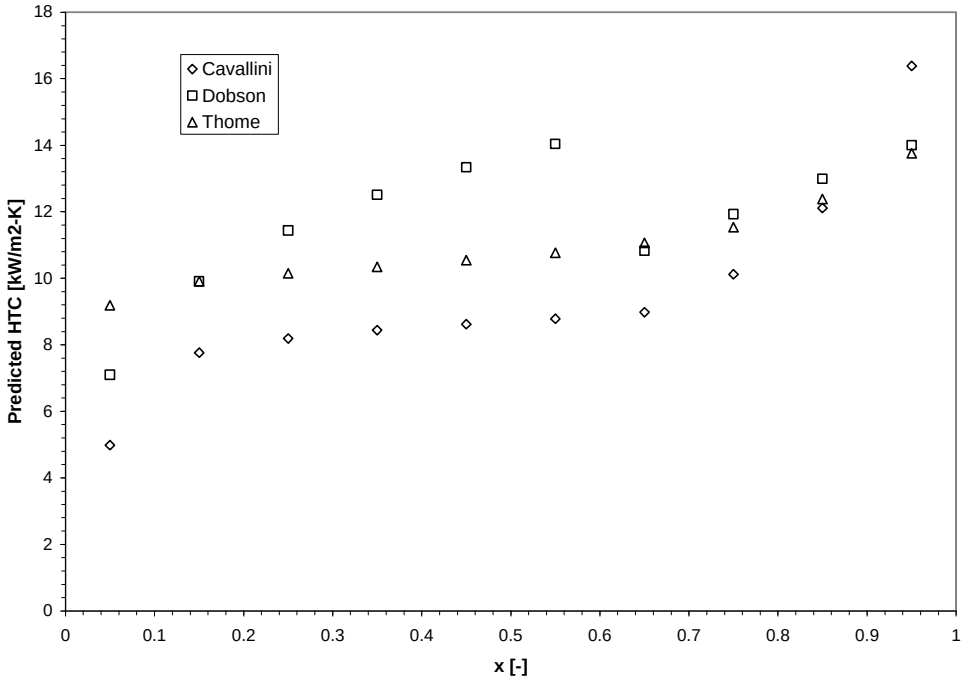

Figure 2.9 Heat transfer coefficient for multiple flow regime correlation comparison for ammonia at G=80 kg/m^2-s

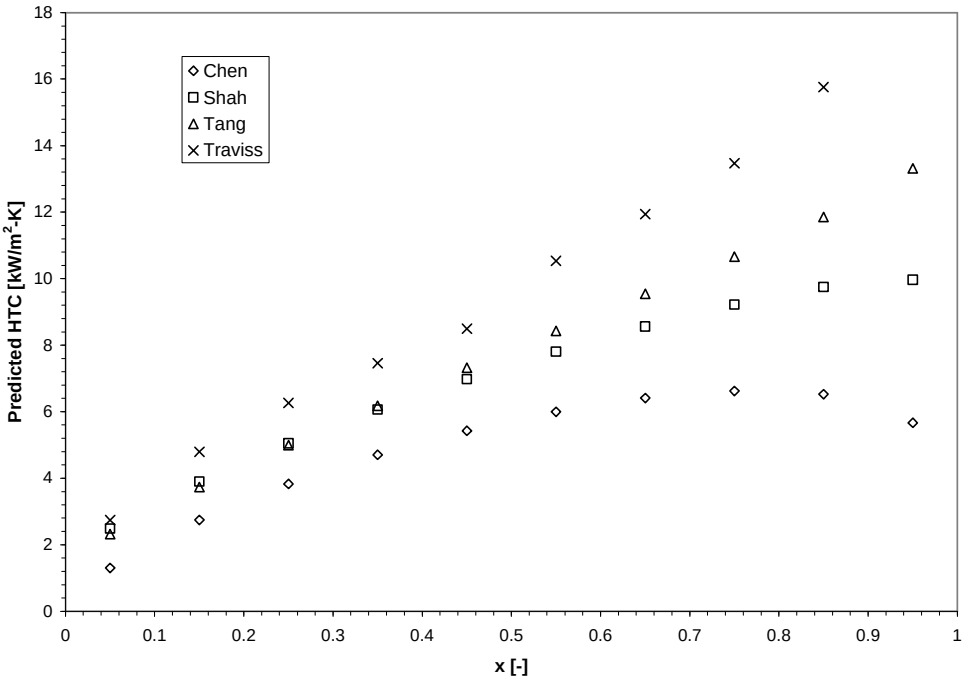

Figure 2.10 Heat transfer coefficient for single flow regime correlation comparison for ammonia at G=80 kg/m^2-s

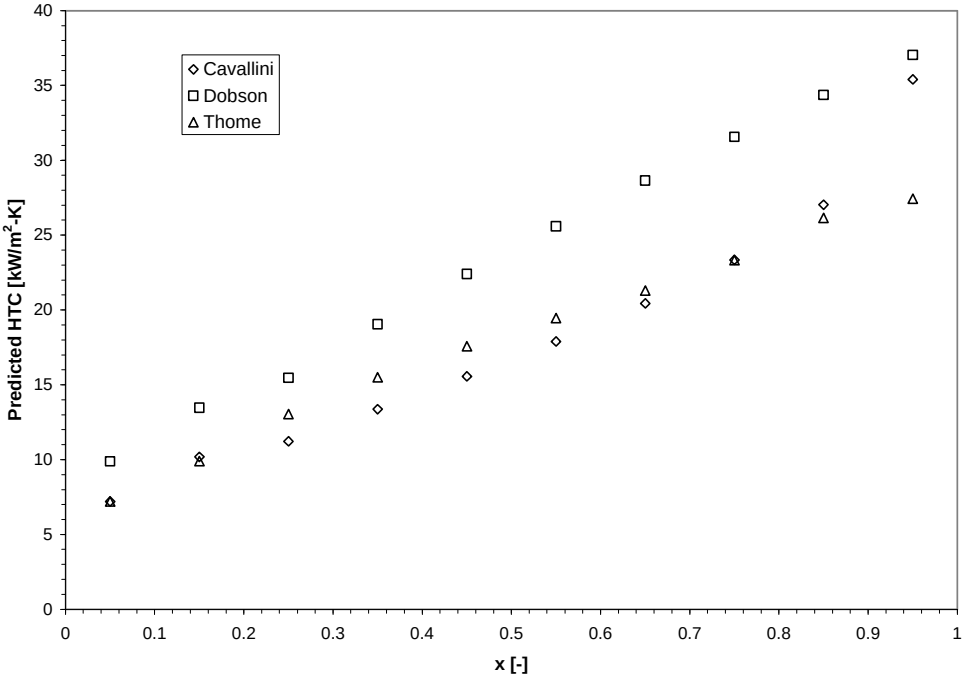

Figure 2.11 Heat transfer coefficient for multiple flow regime correlation comparison for ammonia at G=160 kg/m^2-s

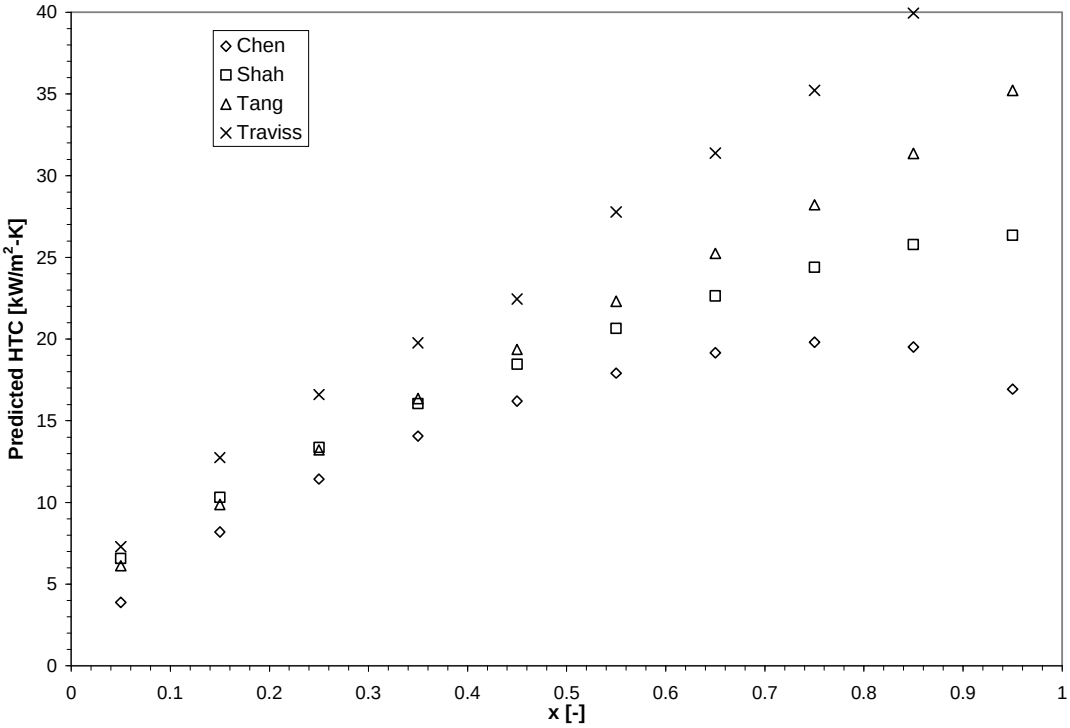

Figure 2.12 Heat transfer coefficient for single flow regime correlation comparison for ammonia at G=160 kg/m^2-s

Table 2.1 Frequently used non-dimensional groups

Group	Interpretation	Definition
Reynolds Number, Re	Ratio of inertial to viscous forces	$\mathrm{Re} = \frac{GD_h}{m}$
Superficial Reynolds Number, Re_l, Re_v	Assumes actual phase flow occupies entire tube	$\mathrm{Re}_l = \frac{GD_h(1-x)}{m_l}$ liquid $\mathrm{Re}_l = \frac{GD_h x}{m_v}$ vapor
Phase Only Reynolds Number, Re_{lo}, Re_{vo}	Assumes flow consists of liquid or vapor only	$\mathrm{Re}_{lo} = \frac{GD_h}{m_l}$ liquid only $\mathrm{Re}_{vo} = \frac{GD_h}{m_v}$ vapor only
Liquid Froude Number, Fr_l	Ratio of inertial to gravitational forces	$Fr_l = \frac{G^2}{r_l^2 g D_h}$
Liquid Weber Number, We_l	Ratio of inertial to surface tension forces	$We_l = \frac{G^2 D_h}{r_l s}$
Nusselt Number, Nu	Dimensionless heat transfer coefficient	$Nu = \frac{hD_h}{k_l}$
Liquid Prandtl Number, Pr_l	Ratio of momentum diffusivity to heat diffusivity	$\mathrm{Pr}_l = \frac{m_l c_{p,l}}{k_l}$
Turbulent Lockhart-Martinelli Parameter, X_{tt}	Ratio of vapor to liquid pressure drop	$X_{tt} = \left(\frac{1-x}{x}\right)^{0.9}\left(\frac{r_v}{r_l}\right)^{0.5}\left(\frac{m_l}{m_v}\right)^{0.1}$

Chapter 3. Experimental Apparatus and Procedure

3.1 Experimental Apparatus

The experimental apparatus was designed to properly circulate and condition the refrigerant to the test sections. Similar versions of this flow loop are discussed by Dobson (1994) and Wilson (2001). Included in this chapter are discussions about the refrigerant loop, steam loop, the test sections, water loop, and instrumentation.

3.1.1 Refrigerant Loop

Figure 3.1 shows a schematic of the refrigerant loop. A variable speed gear pump circulates the refrigerant throughout the loop. A pump was chosen instead of a compressor in order to avoid contaminating refrigerants with compressor lubricant. A compressor unlike a pump requires the circulation of a lubricating oil throughout the test facility leaving the refrigerant dirty or contaminated. Upon exiting the pump the mass flow rate of the refrigerant is measured with a Coriolis-type mass flow meter (Micromotion F025S319S). From here the refrigerant goes to the conditioning portion of the facility. A flat plate heat exchanger (Alfa Laval NB26-10H) is used to condition the flow from sub-cooled liquid to the desired two-phase quality. A bypass line was designed to divert some of the fluid around this heat exchanger. Although bypassing the fluid was seldomly used to achieve the proper thermodynamic state, it proved to be quite useful in system start up. The evaporator was designed to provide up to 15 kW of heating which is required to achieve high qualities at high flow rates. Due to this design requirement, the evaporator provided too much power for lower flow rates or two-phase qualities. To account for exceeding the necessary energy rates at these low mass flux/low quality conditions, the heat exchanger was flooded with the condensate forming on the steam side. This effectively lowered the overall two-phase heat transfer surface area on the steam side, thereby lowering the overall rate of heat transferred.

After leaving the conditioned portion of the loop, the fluid enters the test section(s). The loop was designed to have two test sections in parallel to each other. The flow can be directed into either test section. Upon leaving the test sections, the refrigerant enters the subcooler. Another flat plate heat exchanger (Alfa Lavel NB26-14L) is used to subcool the refrigerant prior to entering the pump. A small receiver tank (500mL) manufactured by Swagelok sits at the bottom of the subcooler. All wetted materials are either nickel, stainless steel, Teflon, or aluminum.

3.1.2 Steam Loop

Figure 3.2 shows the evaporator/conditioning portion of the test loop. Again a flat plate heat exchanger from Alfa Laval (NB26-10H) was used to transfer heat from the steam to the refrigerant. The heat exchanger was mounted in the vertical position. The refrigerant and steam were designed to flow in parallel through the heat exchanger, both entering at the top and exiting at the bottom. This was done for the steam side to allow gravity to properly drain the condensate from the heat exchanger. From the refrigerant's perspective, this design was used so that oil can be added to the refrigerant and not get trapped at the bottom of the heat exchanger. The heat exchanger was designed to meet the highest of energy transfer rates experienced in this experiment (15kW). Because this level of heat rate is only required at the high mass fluxes and high qualities, flooding the heat exchanger with steam condensate was required to achieve lower heat rates. By flooding the steam side of the heat exchanger with condensate, the effective steam two-phase heat transfer area is reduced. Due to the dominance of steam's two-phase

heat transfer rate over its single-phase rate, this in turned decreases the overall heat transfer rate of the steam. The level of condensate is controlled downstream by a needle valve. A site glass was also installed in parallel to the steam side of the heat exchanger. This was done to allow for visual observation of the amount of condensate flooding occurring in the heat exchanger. Once the condensate exits the heat exchanger and site glass it passes through a Coriolis mass flow meter (Micromotion S012S100). Two type T thermocouples measure the temperatures of the steam/condensate. One is placed at the entrance to the heat exchanger, while the other is located at the exit. The steam, prior to entering the heat exchanger, is passed through a condensate separator. The separator effectively eliminates any condensate formed in the steam line, and thereby insuring that the steam enters the exchanger as a saturated vapor (x=1).

3.1.3 Test Sections

The test sections used in this condensation study were modeled after the design Wilson (2001) used. The test sections are comprised of two copper bars along with two cooling (water) jackets. The test section is sandwiched in between the two copper bars, while the cooling jackets are soldered to the sides opposite the test section. This technique of using the copper bars acts as an isothermal material between the cooling jacket and refrigerant. This layout is detailed in Figure 3.3. This design allows for the water to remove up to 400W from the refrigerant. Figure 3.4 is an end view depicting the location of the water cooling jackets with respect to the test section.

A side view of the test section with the locations of temperature measurements appears in Figure 3.5. The test section is 0.9144 m (36") long with thermocouples mounted every 0.1016 m (4"). The thermocouples are mechanically attached to the wall in a very unique way. Using a knife, an angled slit was cut into the wall at each location. 30 gauge Type T thermocouple wire is than inserted into this slit while the cut out edge is then folded back over the wire to securely fasten it. In addition to these wall temperature locations, the inlet and outlet refrigerant temperatures were measured using type T thermocouple probes. The cold water circulating through the water jackets are measured at the inlet and outlet. Both of these measurements are done with type T thermocouples.

Pressure taps are soldered outside the ball shutoff valves at both the inlet and outlet position. The inlet pressure tap is connected to an absolute pressure transducer (Setra model 225), and both inlet and outlet are connected to a differential pressure sensor (Sensotec Z/1309-12-01). A schematic of this is shown in Figure 3.6. A test series was set up to measure the amount of pressure drop caused by the two ball valves located between the pressure taps. This test rig is shown as a schematic in Figure 3.7. Three corrective equations were found, one for each mass flow tested (G=80, 160, 270 kg/m^2-s). These equations are listed in Chapter 4, Equations 4.1-4.3.

Two different types of internal geometries were used in this experiment: smooth, and an axially enhanced microfin tube. Drawings of these two appear in Figure 3.8. Both of these tubes are aluminum and have a nominal outside diameter of 9.5 mm (0.375"). The internal diameters have nominal lengths of 0.72 mm (0.3"). The enhanced tube has 60 microfins placed circumferentially around the tube. The area enhancement created by these fins is approximately 2.2 over the smooth tube.

3.1.4 Test Section Water Loop

The water loop, which is depicted in Figure 3.9, is used to circulate the cooling water through the water jackets on the test sections. A constant temperature bath with digital controller (Thermo Neslab model RTE-220) is used to both pump the water but also to maintain a constant inlet water temperature. Distilled water is pumped through a filter and then through a turbine-type volumetric flow meter (Cole Parmer #EW-32709-60). Upon exiting the flow meter, the water enters the 'selection board' where by various valves it is directed into the desired test section. The water flows in a direction counter to that of the refrigerant in the test section. Two direct flow variable area flow meters (rotameters) and a set of needle valves are used to visually insure that there are equal flows to the top and bottom portions of the test sections. After exiting the test section, the water continues by flowing back to the constant temperature bath. The selection board is also used to switch between the pressure taps on the two different test sections.

3.1.5 Test Conditions

Experiments were performed using both R22 and ammonia primarily at a saturation temperature of 35 ºC. Table 3.1 lists the pertinent properties of the two fluids at this saturation temperature. A few of the data points were taken at other temperatures either 25 or 45 ºC. The mass flux varied from 20 kg/m^2-s to 270 kg/m^2-s with a few tests exceeding 270 kg/m^2-s. The inlet quality was varied from 0 percent up to 95 percent, with a few tests in the subcooled liquid and superheated vapor state.

3.1.6 Instrumentation and Uncertainty Analysis

The uncertainty of any experiment determines the reliability of the experimental data. This uncertainty can be treated in various different ways. For instance, in many experiments one may repeat an experiment at the same condition several times. This allows the results to be treated statistically in order to determine the mean and standard deviation of the data. Unlike these repetitive experiments, two phase refrigerant experiments often require a substantial amount of time to reach steady state. Therefore, most of the literature on two-phase flow heat transfer uses a method called single sample uncertainty analysis.

The uncertainty analysis method used to treat the experimental data here is the method described by Moffat (1988). This method estimates the uncertainty in a variable "y" that depends on "N" independent variables (x_i's) that can not be determined exactly. The equation for the uncertainty in "y" is "δy":

$$\delta y = \sqrt{\sum_{i=1}^{N} \left(\frac{\partial y}{\partial x_i} \delta x_i \right)^2} \qquad (3.1)$$

The uncertainty of each measured quantity consists of the uncertainty in the measurement devices, the uncertainty of the data-acquisition equipment, the uncertainty in the sensor to data acquisition system, and conceptual errors. Three different experimental variables are the focus of this uncertainty analysis. These variables include the heat transfer coefficient, the inlet quality of the refrigerant (entering the test section) and the pressure drop of the refrigerant (dP) across the test section. The following is a list of experimental components that contribute to these uncertainties.

1. Wall temperature measurement
2. Inlet and outlet water temperatures

3. Surface area measurements
4. Water flow measurements
5. Steam flow measurements
6. Refrigerant flow measurements
7. Differential pressure measurements
8. Inlet and outlet refrigerant temperatures
9. Pre heat refrigerant temperature
10. Inlet and outlet steam/condensate temperatures
11. Heat loss prediction
12. Prediction of the thermal resistance of the aluminum tube wall

In a complete analysis of uncertainty, all of the uncertainties of the aforementioned components would be used. But the method used in this study (root sum square) minimizes the effect of small uncertainties relative to larger uncertainties so greatly that the small uncertainties can be neglected with negligible loss of accuracy. From this basis, for example, the aluminum wall thermal resistance due to its high conductivity was neglected.

Equation 3.2 is the expanded version of equation 3.1. It is expanded to include all of the components contributing to the uncertainty calculation of the heat transfer coefficients.

$$\frac{\delta h}{h} = \left[\frac{\left(\dot{m}_w c_{p,w}\right)^2 \left(\delta T_{w,i}^2 + \delta T_{w,o}^2\right) + \left(c_{p,w}\left(T_{w,i} - T_{w,o}\right)\right)^2 \delta \dot{m}_w^2 + \dot{Q}_l^2}{\left(\dot{m}_w c_{p,w}\left(T_{w,i} - T_{w,o}\right) + \dot{Q}_l\right)^2} + \frac{\delta T_{sat}^2 + \delta T_w^2}{\left(\delta T_{sat} - \delta T_w\right)^2} \right]^{0.5} \tag{3.2}$$

Equation 3.2 provides considerable insight on how each individual component affects the total uncertainty of the heat transfer coefficient. For instance, the uncertainty in the saturation and wall temperatures are divided by the temperature difference between them, each yielding a component uncertainty equal to the percentage uncertainty in the temperature difference. The uncertainties on the water side heat transfer rate and heat loss are both divided by their sums. This indicates that the heat loss makes up a small fraction of the overall heat transfer. This is true even when a large uncertainty percentage exists for the spurious heat loss.

Furthermore, equation 3.2 shows that the water, saturation and wall temperature measurements contribute the most to the overall uncertainty. The inlet and outlet water and saturation temperatures were measured using type T copper-constantan thermocouple probes. These probes were calibrated against a NIST-traceable platinum RTD thermometer (Omega DP-241, ±0.035ºC accuracy) using a constant temperature water bath. Separate calibration curves were fit to the data for each thermocouple. The thermocouples were 'spot-checked' periodically throughout the course of the project and they were found to be within ±0.1C of their original calibration. Therefore, the associated absolute uncertainty that accompanies these temperature measurements was set at ±0.1C.

Unlike the calibration methods used for the water and saturation temperatures, the tube wall temperatures were calibrated against the saturation temperatures in situ. Saturated refrigerant was run through the test section at a constant saturation temperature until the change in wall temperature was less than 0.05 ºC per minute thereby insuring an isothermal test section. This was done at five different saturation temperatures. The calibration curves

were then generated by plotting each different wall location versus the saturation temperature using the set of five different temperatures. This calibration data was inputted into the data acquisition system. The nine different wall temperatures agreed to within ±0.04C. Again, the wall temperatures have been 'spot-checked' periodically throughout the course of the activities and found to be within ±0.1C of their original calibration. Therefore, the absolute uncertainty that was assigned to the wall temperature measurements was ±0.1C per location.

The water flow rate was measured by a turbine type volumetric flow meter (Cole Parmer #EW-32709-60). This meter was calibrated using a bucket-stop watch method. Over 20 calibration points were taken by measuring the amount of water flowing into a bucket. The time per each calibration point was measured using a handheld electronic stop watch. This method proved to be very accurate, as the uncertainty between the calibration points and the resulting calibration curve was less than ±1%.

A second source of uncertainty in this project is the uncertainty associated with the differential pressure and absolute pressure measurements. A Sensotec differential pressure transducer (Z/1309-12-01) with an operating range of 0-5 psid (0-35 kPa) was used to monitor the pressure drop across the test section. It has an accuracy of ±0.25% full scale. The absolute pressure transducers used to measure the test section inlet and preheat inlet pressures are Setra model GTC225. These also have an uncertainty of ±0.25 full scale and have an operation range of 0-250 psig (0-1724 kPa).

The absolute pressure transducers were both calibrated against the same pressure calibrator. An SI Pressure Instruments #DTG-2K-30 (±1.5 kPa calibrated accuracy at range of interest) was used to do this calibration. The differential pressure transducer was calibrated against a water manometer. First order calibration curve fits were applied to each instrument.

As mentioned earlier, two coriolis-type mass flow meters are used to measure the mass flow rates in the refrigerant and steam condensate lines. These sensors operate by measuring the vibrational frequency of a U-tube, and a specific 4-20mA current output corresponds to a given flow rate. The refrigerant mass flow meter is a Micromotion model F025S319S with a maximum flow rate of 0.605 kg/s and an accuracy of ±0.2% of the reading. The condensate mass flow meter is a Micromotion model S012S100 with a maximum flow rate of 0.038 kg/s and an accuracy of ±0.15% of the reading.

All temperature, flow rate, and pressure measurements were calibrated while being connected with the data acquisition system. This 'end-to-end' method effectively eliminates any error associated with the electrical connections used or by the differences in measurement techniques when.

3.1.7 Data Acquisition

Process parameters are measured by a computerized data acquisition system comprised of an Agilent 34970A switch unit connected to a personal computer. An internal 6.5 digit (22 bits) multimeter allows measurements to be conducted from the three multiplexer boards to which the instrument outputs are connected. The switch unit can scan up to 250 channels per second with a basic VDC (direct current voltage) accuracy of ±0.004%. Two 20 channel voltage modules (Agilent 34901A) are used for all temperature measurements. The Agilent 34901A also has the capability to measure two current sources. These current channels are used to measure the micromotion coriolis type flow meters. The scan rate of the 34901A multiplexer is 60 channels per second. One

16 channel multiplexer board (Agilent 34902A) is used to measure voltage outputs of the various pressure transducers, water flow meter, and power meters. The scan rate of the 34902A is 250 channels per second. The multiplexer boards are connected to jack panels with grounded and shielded wire to limit electrical interference and drifting in the measured voltages. The jack panels allow for quick connection of instrument outputs and thermocouples to the data acquisition system.

This system, interfacing with HP VEE data acquisition software, allows visual readouts of desired parameters as well as broad data analysis capabilities. Several computations are performed in the data acquisition program, such as calculating mass flux, heat flux, test section inlet quality, and quality change during condensation. HP VEE also interfaces easily with Microsoft Excel, which facilitates data recording and analysis. An interface was made with REFPREX through Microsoft Excel. REFPREX is an offshoot of REFPROP which is a piece of software that calculates the properties of various refrigerants. Through this interface the various enthalpies of the refrigerants were calculated based off of measured pressures and temperatures. This allowed for an easy, accurate method of calculating the inlet quality, and change in quality. This information was then passed back to HP VEE via Microsoft Excel.

3.1.8 Calculated Parameters

As mentioned above, the HP VEE data acquisition program in conjunction with REFPREX performs several computations necessary to carry out experimental procedures. Of importance are the following parameters: refrigerant mass flux, enthalpies at various locations, inlet quality, and heat transfer coefficients.

Mass flux is simply determined by dividing the total mass flow rate by the test section cross sectional area.

The refrigerant's enthalpies are calculated at two locations through the use of energy balances. The first location is the enthalpy calculation of the subcooled liquid prior to entering the evaporator/condition heat exchanger. This is done by simply measuring the pressure and temperature at this location and using the following equation:

$$h_{sub} = h_l + v_l\left(P_{sub} - P_l\right) \tag{3.3}$$

Internal energy for the subcooled and saturated liquid states is assumed to be equal; however, a small modification is used for the Pv term in the enthalpy relation. As can be seen from equation 3.3, the $P_l v_l$ term is subtracted while the $P_{sub} v_l$ term is added. Since in subcooled conditions, v_l very nearly equals v_{sub}, the $P_{sub} v_l$ term is nearly exact.

Knowing the enthalpy of the subcooled liquid is the first step in determining the refrigerant's quality at the test section inlet. The second step is calculating the energy or heat that goes into the refrigerant by the steam in the evaporator/conditioner. This is calculated by doing an energy balance using the measured parameters on the steam side. $\dot{Q}_{PH}$ is the derived in the following equation:

$$\dot{Q}_{PH} = \dot{m}_{cond}\left(h_{fg,steam} + c_{p,condensate} \cdot \left(T_{steam,in} - T_{condensate,out}\right)\right) \tag{3.4}$$

Equation 3.5 is used to determine the refrigerant's enthalpy at the test section inlet

$$h_{TS\_in} = \frac{\dot{Q}_{PH}}{\dot{m}_{refr}} + h_{sub} \tag{3.5}$$

In the above equation, the heat rate divided by the refrigerant's mass flow rate is added to the subcooled enthalpy level. The result is the enthalpy level of the refrigerant exiting the evaporator. Because the test loop is insulated it is assumed that heat losses/gains from the ambient air is negligible and that the enthalpy levels at the test section inlet and evaporator outlet are equal. Knowing the test section inlet enthalpy, the inlet vapor quality can be calculated.

$$x = \frac{h_{TS\_in} - h_l}{h_v - h_l} \tag{3.6}$$

In the above equation (3.6), the saturated liquid and vapor enthalpies are calculated using the REFPREX software. During the heat transfer experiments, similar energy balances are used to calculate the change in quality throughout the length of the test section.

3.2 Experimental Procedure

This section details the operation of the loop during experimental testing.

3.2.1 Heat Exchange Experiments

The main goal of this project was to characterize the heat transfer coefficients and pressured drop of two-phase ammonia under condensation conditions. The majority of the two-phase condensation experiments were conducted at a saturation temperature of 35 ºC (95 ºF) with a few selected points taken at 25 ºC and 45 ºC (77 ºF and 113 ºF). A combination of the steam and chilled water loops were utilized to achieve these set temperatures. For flows that require a low heat input from the steam side (i.e. low G, low x), the steam heat exchanger would be flooded with condensate, causing less heat input. In addition to this, the amount of chilled water circulation throughout the subcooled heat exchanger was reduced. By combining these two techniques, the desired saturation temperature was attained. For flows that require a relatively high heat input from the steam side (i.e. high G, high x), the level of condensate flooding is reduced (hence more heat input). Also, the amount of chilled water in circulation was increased, taking more heat out of the refrigerant and thereby lowering the saturation temperature.

These two-phase experiments were conducted at inlet qualities of 0, 10, 20 ,40, 60, 80, 90, and 95%. The mass fluxes used were 20, 40, 80, 160, and 270 kg/m^2-s. Due to limitations in the sizing of the steam side flat plate heat exchanger, flows over a quality of 60% and a mass flux of 270 kg/m^2-s were very difficult to achieve. The cooling water was circulated in a direction counter to that of the refrigerant. The temperature and flow rate of the cooling water was controlled to attain the desired 4-6ºC (7-11ºF) temperature difference ($T_{cw,out}$-$T_{cw,in}$). In addition to this, a test section heat flux of 4-10 kW/m^2 (1270-3170 Btu/h-ft^2) was set as the standard.

3.2.2 Methodology

This subsection covers the necessary equations that are solved to determine both the pressure drop and the heat transfer coefficients. The pressured drop across the test sections is measured by a differential pressure transducer. Although this pressure drop is important, it is necessary to normalize it with respect to length to compare with existing literature. This is done by the data acquisition system. The nominal pressure drop is divided by the length of the tube in between the pressure taps. This length is approximately 114.3 cm (45").

Determining the heat transfer coefficient proves to be more of a challenge. Several parameters are needed to solve for it. One parameter, the test section heat input is calculated by using the known parameters on the water side of the test section. Equation 3.7 lends insight into this calculation.

$$\dot{Q}_{ts} = \left(\rho \dot{V}\right) c_p \left(T_{cw,in} - T_{cw,out}\right) \tag{3.7}$$

The test section heat flux can then be calculated from this by simply dividing the heat transfer above by the total surface area of the test sections. Due to the length of the copper bar (91.5 cm, or 36”), only that length is used in the calculation of the effective test section surface area. The heat transfer coefficient can then be calculated using the following:

$$h = \frac{\dot{Q}_{ts}}{A_{surf}\left(T_w - T_{refr}\right)} \tag{3.8}$$

Since there are nine different wall temperature measurements along the length of each test section, the refrigerant temperatures must be calculated at each of those locations. This is accomplished by interpolating between the inlet and outlet temperature readings. The wall temperatures are compensated for conduction to find the wall surface temperature at each of their locations. The nine temperature differences T_w-T_{refr} are then averaged. Because each cover equal amounts of the test section in terms of area, a straight average was used.

3.3 Figures and Tables

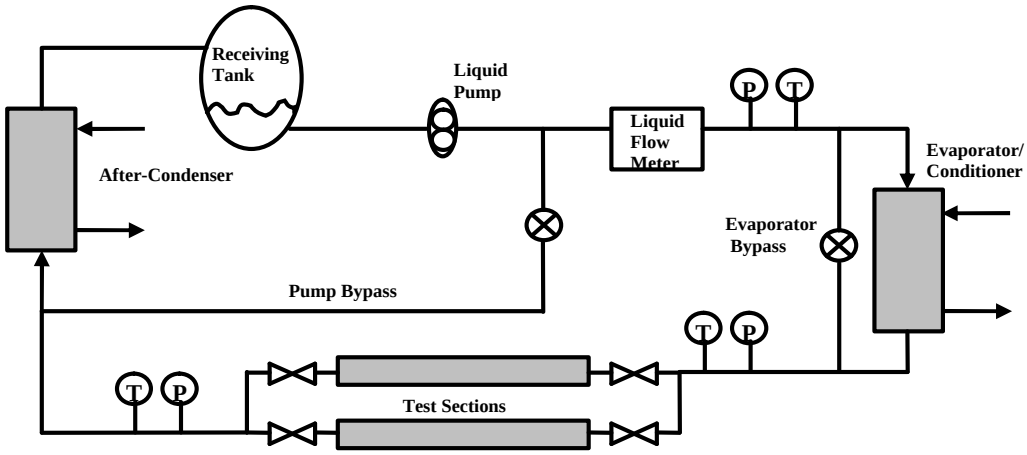

Figure 3.1 Schematic of refrigerant loop

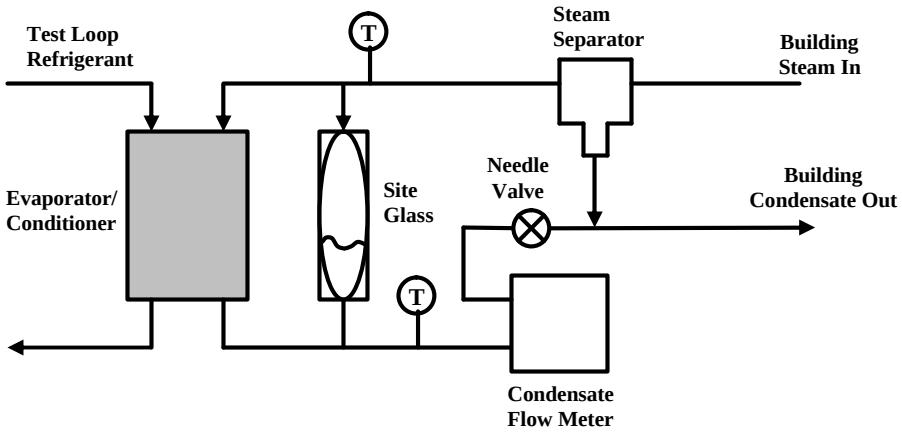

Figure 3.2 Schematic of steam loop

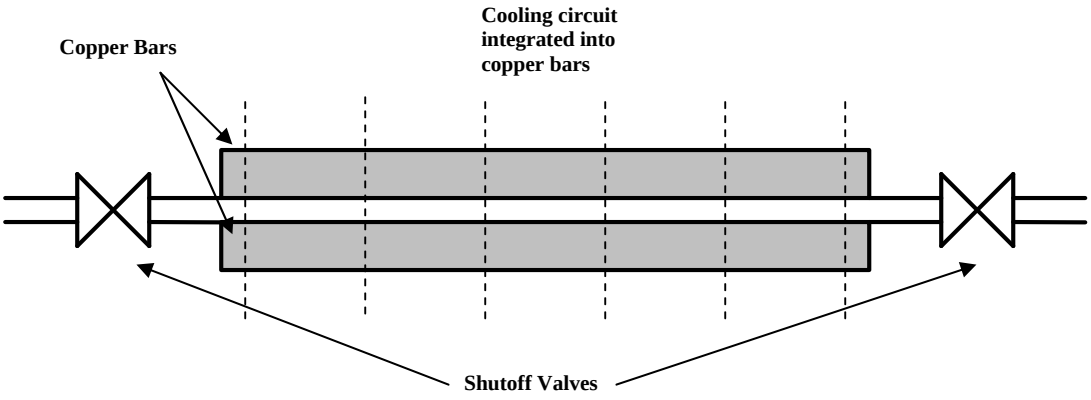

Figure 3.3 Side view of test section with shutoff valve locations

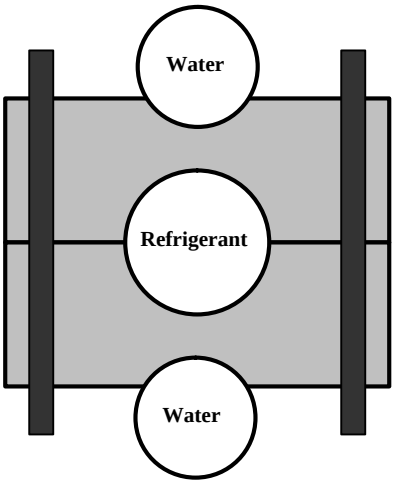

Figure 3.4 End view of test section with copper bar

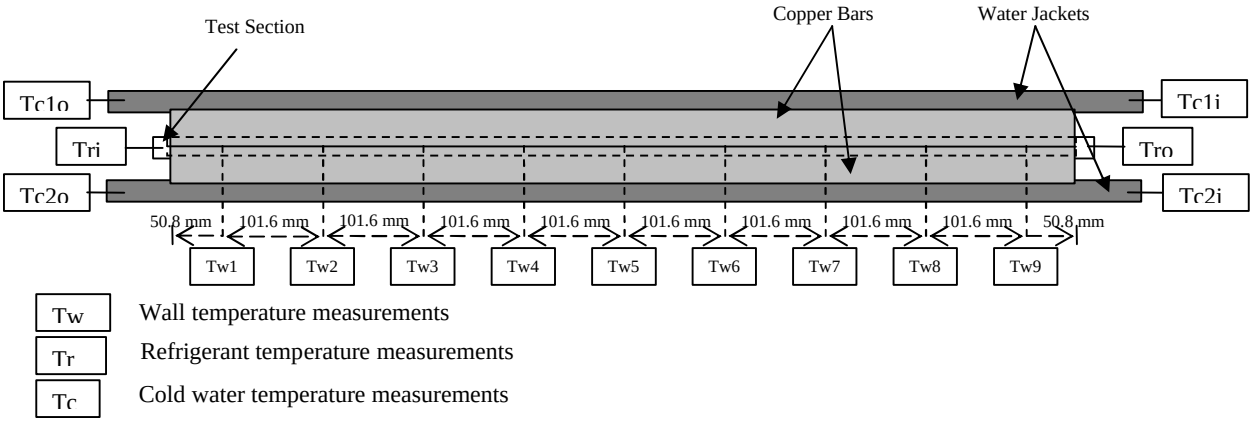

Figure 3.5 Side view of test section with thermocouple locations

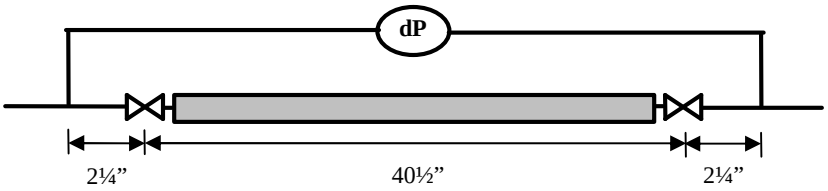

Figure 3.6 Side view of test section with pressure tap locations

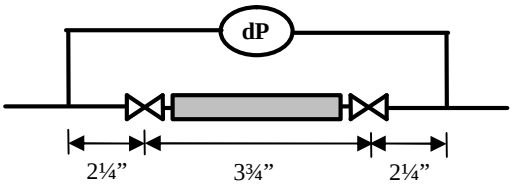

Figure 3.7 Side view of test section used to measure pressure drop across ball valves

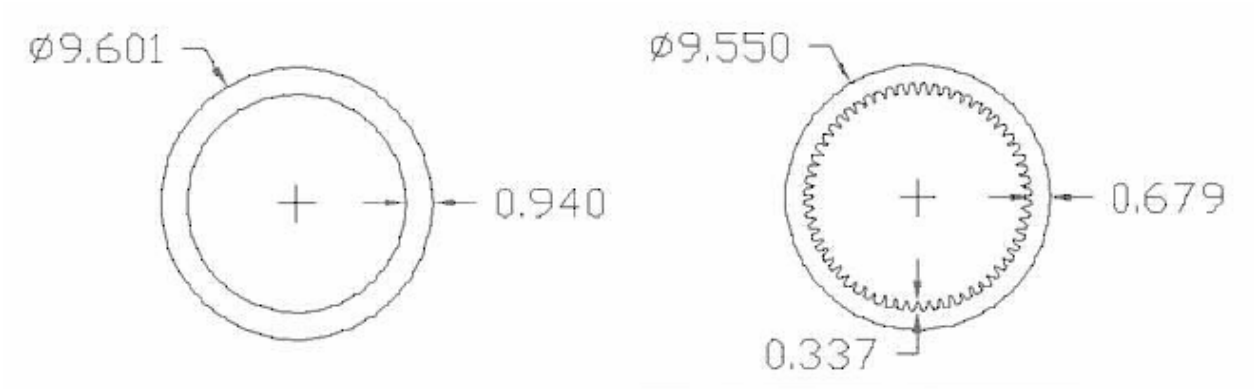

Figure 3.8 Schematic of tube geometry (dimensions in inches)

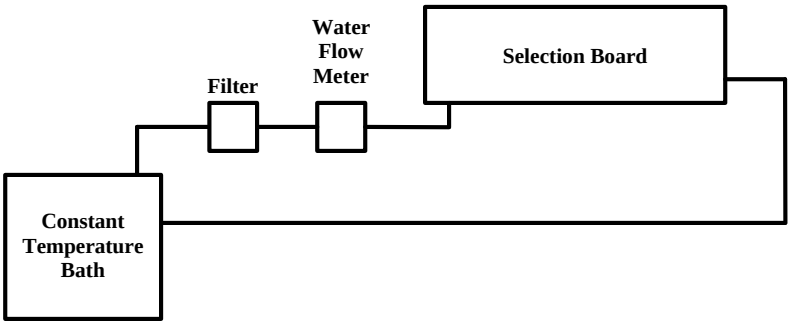

Figure 3.9 Schematic of test section water circulation loop

Table 3.1 Refrigerant properties at 35 ºC saturation temperature (from EES)

Refrigerant	R22	Ammonia
Pressure [kPa]	1354	1354
Liquid Density [kg/m^3]	1153	587.3
Vapor Density [kg/m^3]	57.9	10.47
Liquid Viscosity [kg/m-s]	1.67E-04	1.29E-04
Vapor Viscosity [kg/m-s]	1.40E-05	1.08E-05
Liquid Specific Heat [J/kg-K]	1272	4925
Vapor Specific Heat [J/kg-K]	915	3212
Liquid Thermal Conductivity [W/m-K]	0.0828	0.4579
Vapor Thermal Conductivity [W/m-K]	0.0129	0.029
Enthalpy of Vaporization [kJ/kg]	172.5	1121
Surface Tension [N/m]	0.0067	0.0192

Chapter 4. R22 Condensation Heat Transfer Results

Heat transfer results of R22 for both single and two-phase flows are discussed in this chapter. Comparisons of the R22 experimental results are made to existing heat transfer correlations for single-phase and two-phase flow conditions.

4.1 Single Phase Heat Transfer Results

The single phase tests were conducted primarily in the subcooled liquid regime, with a few data points collected with superheated vapor. Figure 4.1 illustrates the dependence of the heat transfer coefficient on mass flux (G), while Figure 4.2 shows the single phase heat transfer data in comparison to the Dittus-Boelter and Gnielinski correlations. This plot indicates that results from the smooth tube test section compare favorably to the classical single phase heat transfer correlations of Dittus-Boelter and Gnielinski. Conversely, the experimental data taken from the enhanced tube tends to be lower than the predicted values of these two correlations. Figures 4.3 and 4.4 show the experimental data in terms of the Nusselt number plotted against the Reynolds number. Within this set of figures, experimental error bars determined from an uncertainty propagation analysis using the procedure previously described (Section 3.1.6). For clarity, error bars are only placed on the experimental data points falling at the extremes (i.e. low quality and high quality) and uncertainty should be interpolated for the intermediate.

Figures 4.5 through 4.8 illustrate how the single phase heat transfer results compare versus four single phase heat transfer coefficient models for the smooth and enhanced tubes. The models are the classical correlations of Churchill, Colburn, Dittus-Boelter and the Gnielinski correlations. Figure 4.5 demonstrates the predictability of the smooth tube results. From this plot, it is observed that all four of the correlations predict the data within ±15% with the Dittus-Boelter correlation being able to predict the best.

From Figures 4.1 and 4.2, it is observed that the experimental data taken from the enhanced tube tends to be lower than both the predicted values and the smooth tube data. This discrepancy between data sets leads to the poor enhancement factors of the data.

Enhancement factors quantify how the enhanced tube experimental results compare to those of the smooth tube.

$$EF = \frac{hA}{hA_{rsG}} \tag{4.1}$$

In the above equation h_{rsG} is the heat transfer coefficient calculated using an adjustment of the Cavallini correlation for two phase flow and the Dittus-Boelter correlation for single phase flow. These correlations were adjusted by a constant so that the enhancement factor of the smooth tube is approximately one. Traditionally the surface area increase is a primary factor causing heat transfer enhancement. For the tubes studied in this project, the enhanced tube's surface area is 0.05146 m^2 per meter of length, which is more than twice the surface area of the smooth tube at 0.0235 m^2 per meter. Therefore, the expected overall enhancement factor should be on the order of two if the tubes had similar heat transfer coefficients.

The single phase R22 enhancement factors are plotted in Figure 4.9. A correction of 0.057 kW/m^2-K was added to adjust the predicted values of Dittus-Boelter to more closely match the smooth tube experimental results.

4.2 Two Phase Condensation Heat Transfer Results

R22 has been studied as a means of checking the experimental facility, test procedures and data reduction methods. Condensation heat transfer data for R22 appears in Figure 4.10, while Figure 4.11 shows a comparison between the smooth tube data and predictions from Cavallini's (2002) model. Notice that the heat transfer coefficients for the enhanced test section do not appear to be a function of the fluid mass flux (G). These data points all seem to fall on the same line throughout the range of quality. These heat transfer coefficients are also considerably less than those observed in the smooth tube which is very similar to the characteristics described in the single phase testing. This trend along with the one perceived in the single phase tests suggests that something in the enhanced geometry is hindering the fluid's heat transfer. One possibility is that the enhanced tube's geometry is stagnating the fluid in between the microfins. If the fluid is indeed stagnate and not moving in this area surrounding the fins, the effective surface area for two phase convection is considerably less. This would result in lower heat transfer coefficients because the entire surface area is taken into consideration in the calculation of these values. A more detailed explanation for this is offered in Chapter 5 in regards to ammonia test results.

The smooth tube experimental data display general trends that are consistent with results reported in the literature. The experimental heat transfer coefficients increase both as the mass flux (G) and the quality are increased. One key observance is that the experimental data at low qualities are approximately the same regardless of mass flux. As the quality was increased to around 30%, the heat transfer coefficient began to display a much more pronounced quality effect. This can be explained by thinking about the liquid film thickness and its affect on heat transfer coefficients. Liquid film thickness is one of the governing physical features of two phase heat transfer in that the liquid resistance is far greater than the vapor resistance. A saturated fluid exhibits more thermal resistance at low qualities where the amount of liquid is far greater than vapor. The increasing heat transfer coefficient trend with respect to increasing quality demonstrates this physical feature of two phase flow.

Heat transfer coefficients for the smooth tube tend to increase with increasing mass flux (G). This can be explained by the amount of turbulence in the fluid. Turbulent motion of the liquid layer enhances heat transfer. The amount of turbulence in a fluid is directly proportional to the speed of the fluid . Therefore, the heat transfer coefficient is a function of both mass flux and quality.

Figures 4.12 and 4.13 illustrate how well the existing two-phase condensation correlations are able to predict the experimental data. In Figure 4.12, the three flow regime-based correlations are presented. These include the Cavallini (2002), Dobson (1994), and the Thome (2003) correlations. These correlations appear to perform fairly well, with the Thome and Cavallini emerging as the best. All three correlations tend to consistently overpredict the data. Figure 4.13 shows the predictions of the annular based correlations. These correlations include the Chen (1966), Shah (1979), Tang (1997), and Traviss (1973) models. All four models seem to be inconsistent in predicting the experimental data. This is probably due to the models being based only on annular flow regime characteristics.

An enhancement factor (EF) is used to compare the enhanced and smooth tubes as shown in Figure 4.14. This plot demonstrates that despite having a significant surface area enhancement (more then twice the internal surface area of the smooth tube) that the enhanced tube overall performs worse than the smooth tube in terms of heat transfer. Generally, an enhancement factor is greater than unity; in fact it is often just the ratio of enhanced surface

area to the surface area of the smooth tube. However, in this case the enhancement factor has been found to fall below unity except for a few select points showing an enhancement greater than one. A correction of 0.437 kW/m^2-K was added to the Cavallini (2002) correlation to adjust the correlation to the smooth tube experimental results. For a more detailed definition of an enhancement factor, please refer back to section 4.1.

4.3 R22 Summary

R22 was used to establish baseline test results with the new ammonia heat transfer test facility and to practice experimental methods employed in the operation of the test facility. Included in this baseline testing were both single phase and two phase condensation heat transfer experiments. This experimental data (both single and two-phase) collected on the smooth tube correlates reasonably well with existing correlations thereby suggesting that the test apparatus and methods are sound. Experimental data gathered on the enhanced tube suggest that the fin structures are not improving the heat transfer, and in some manner are affecting the flow field in an undesirable manner.

4.4 Figures

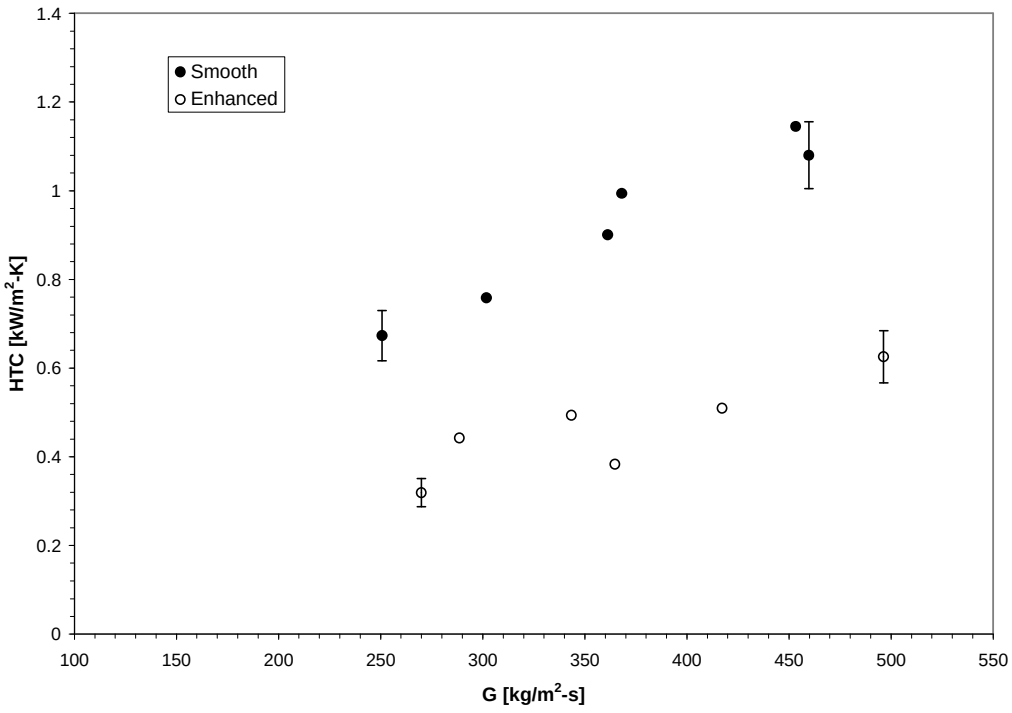

Figure 4.1 Single phase R22 heat transfer coefficients for smooth and enhanced tubes.

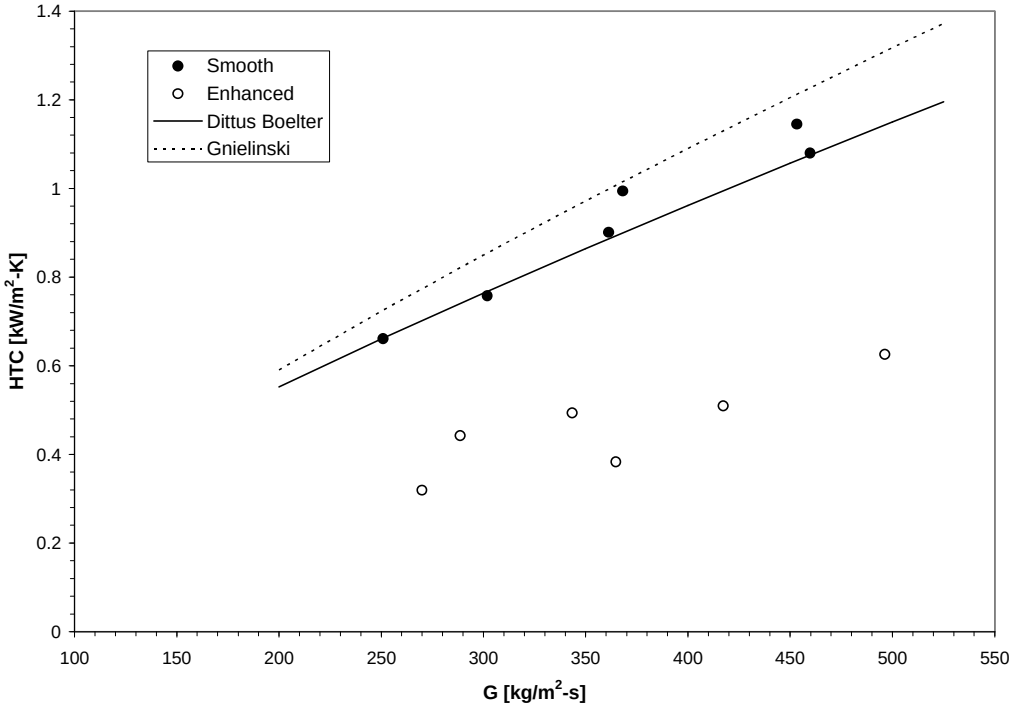

Figure 4.2 Single phase R22 heat transfer with correlations

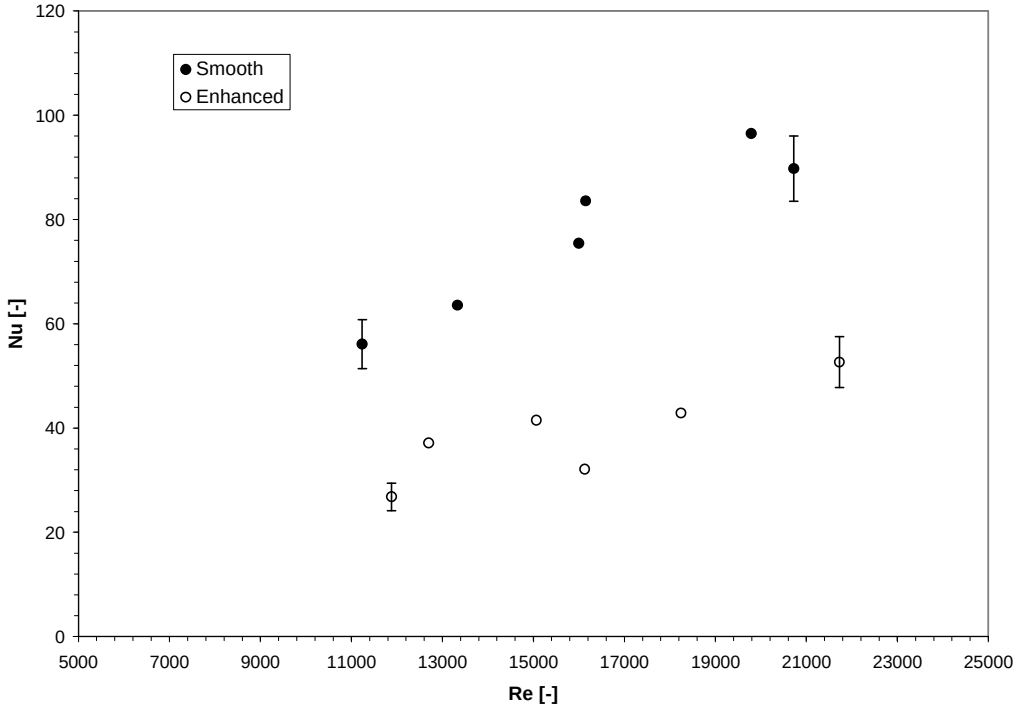

Figure 4.3 Dimensionless heat transfer single phase R22 without correlations

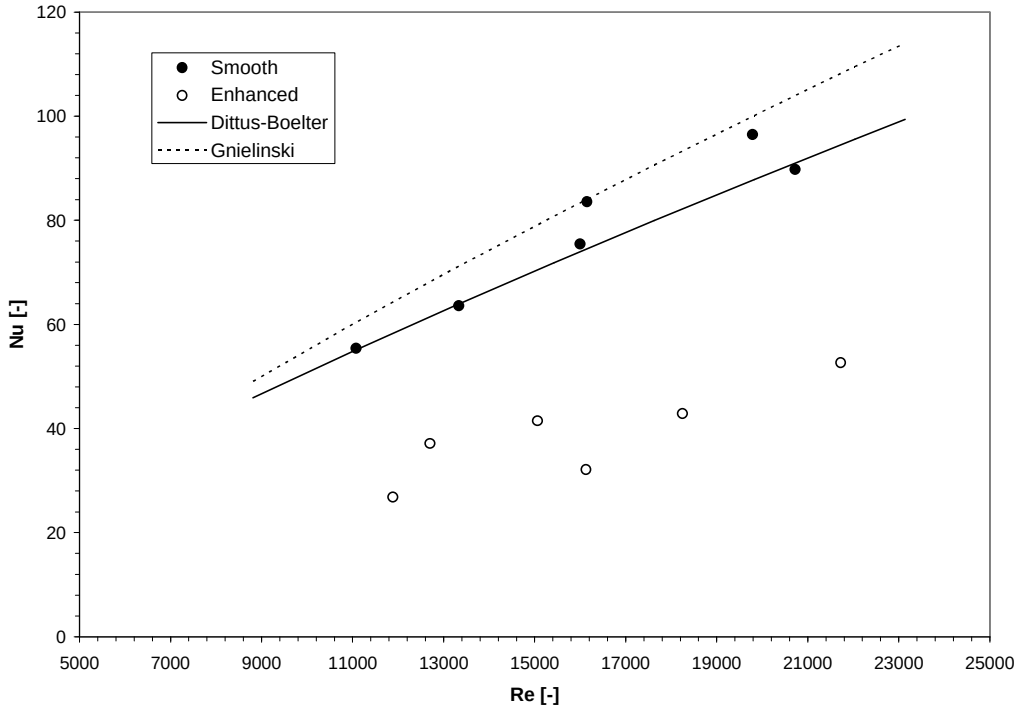

Figure 4.4 Dimensionless heat transfer single phase R22 with correlations

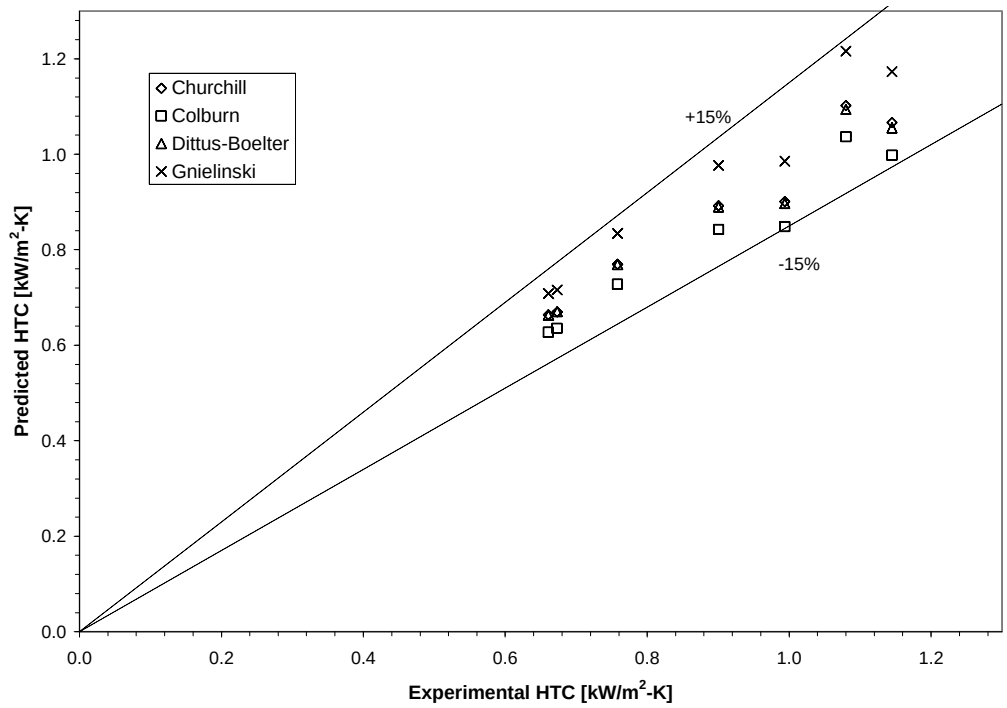

Figure 4.5 Single phase R22 heat transfer correlation smooth tube comparison

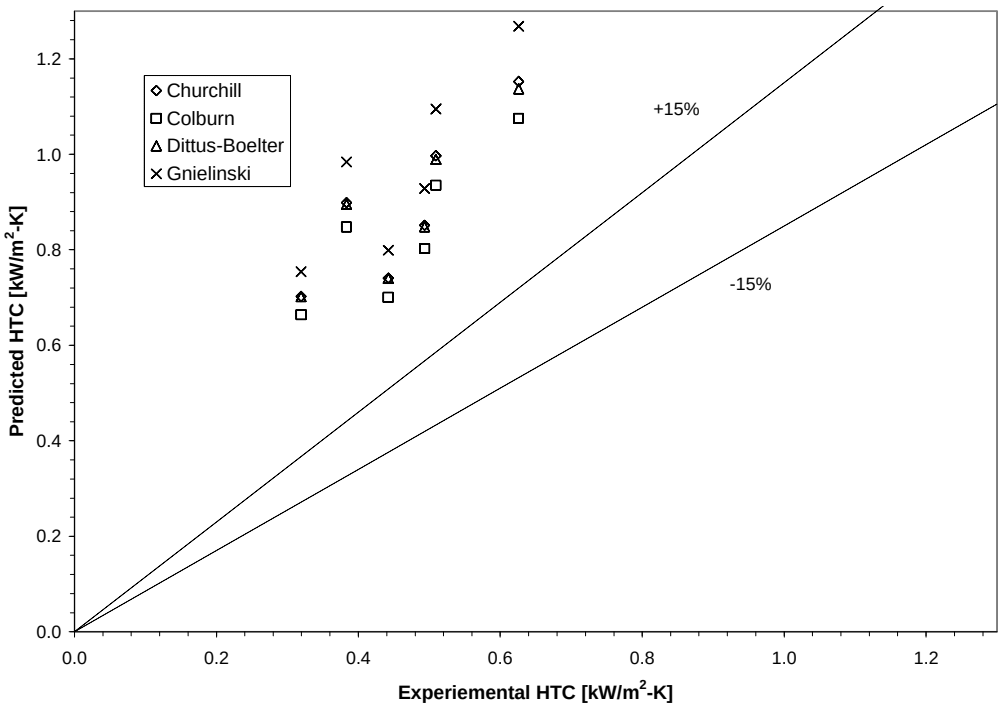

Figure 4.6 Single phase R22 heat transfer correlation enhanced tube comparison

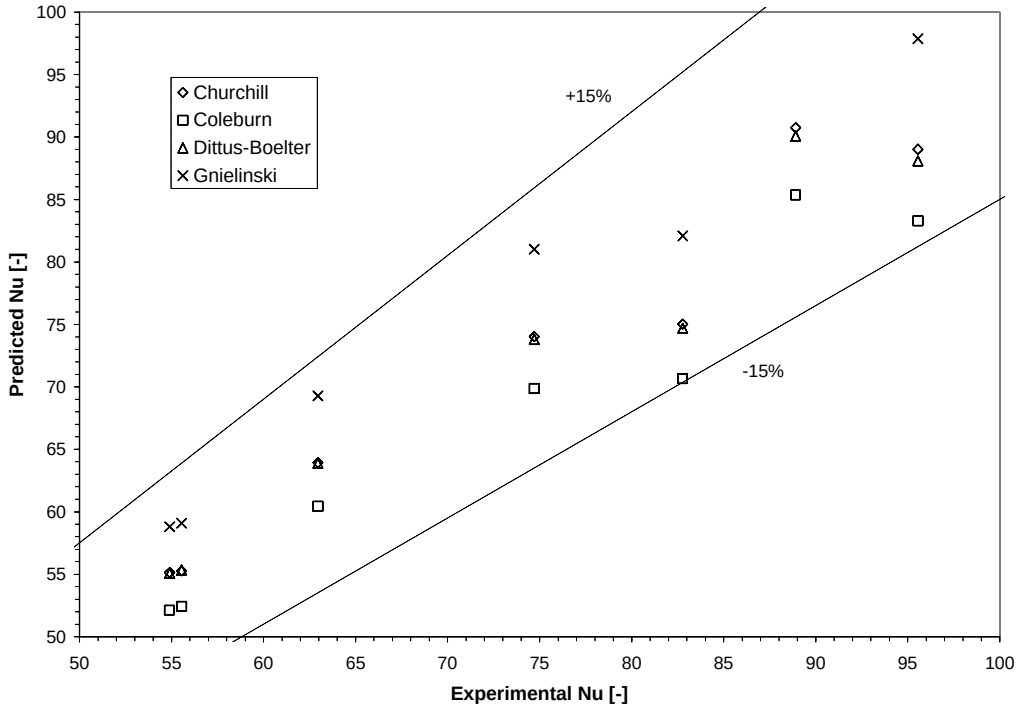

Figure 4.7 Dimensionless single phase R22 heat transfer correlation smooth tube comparison

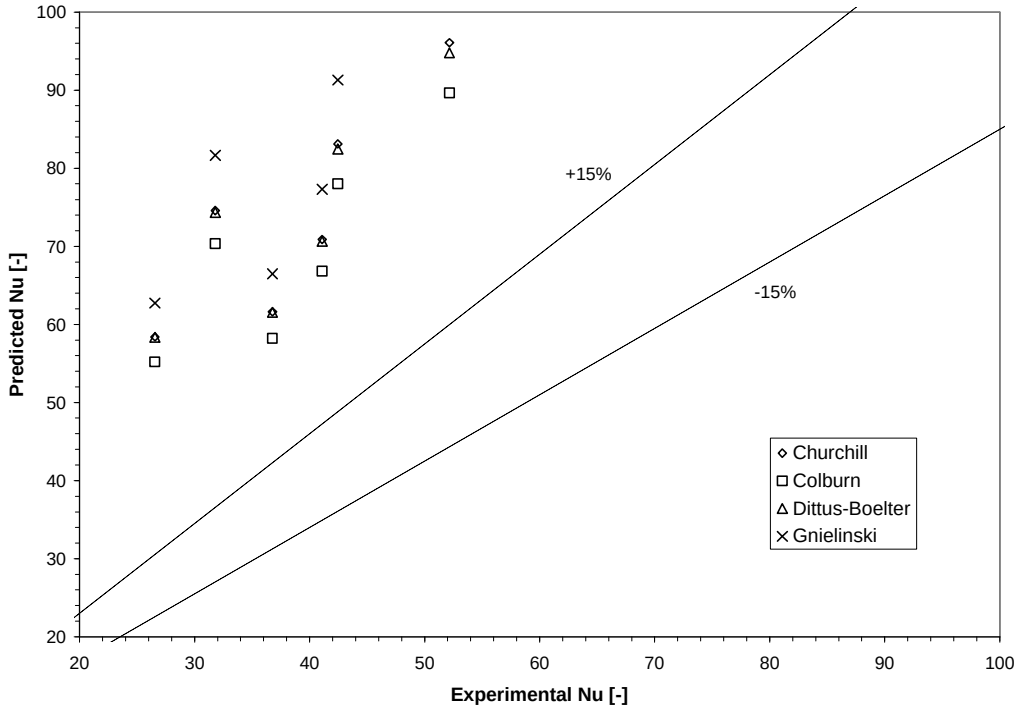

Figure 4.8 Dimensionless single phase R22 heat transfer correlation enhanced tube comparison

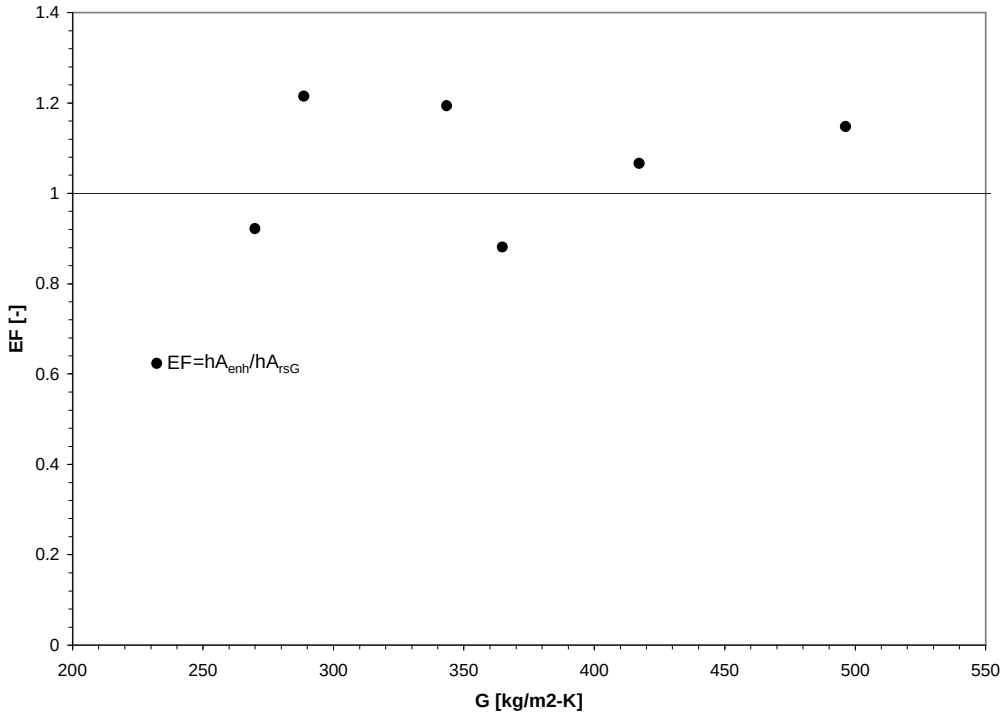

Figure 4.9 Enhancement factor for single phase R22 heat transfer

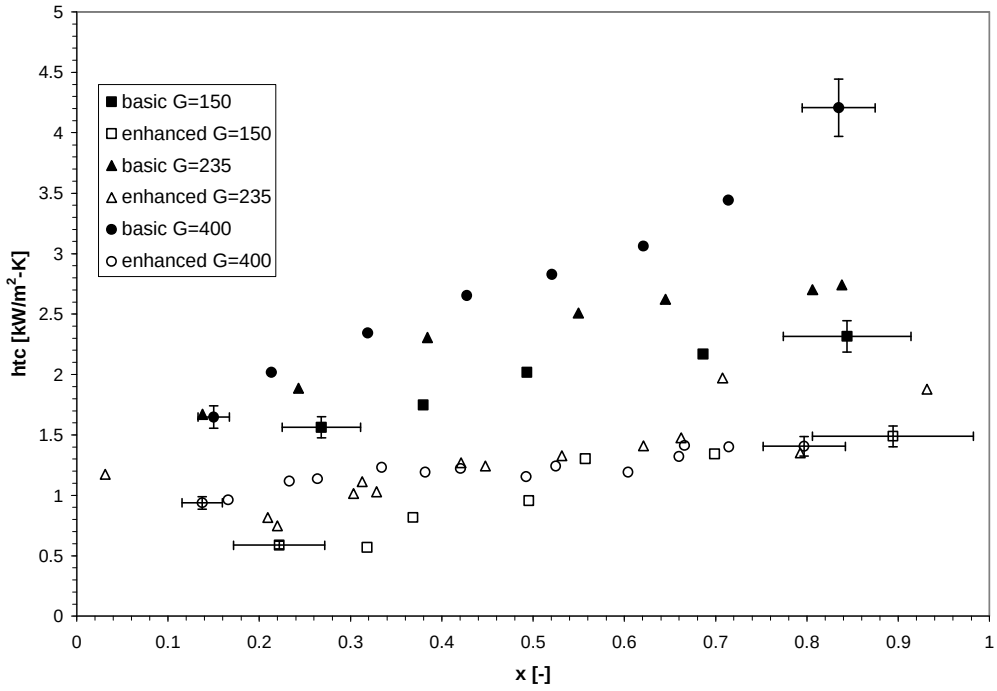

Figure 4.10 Two phase R22 heat transfer results (Mass Flux, G, in kg/m^2-s)

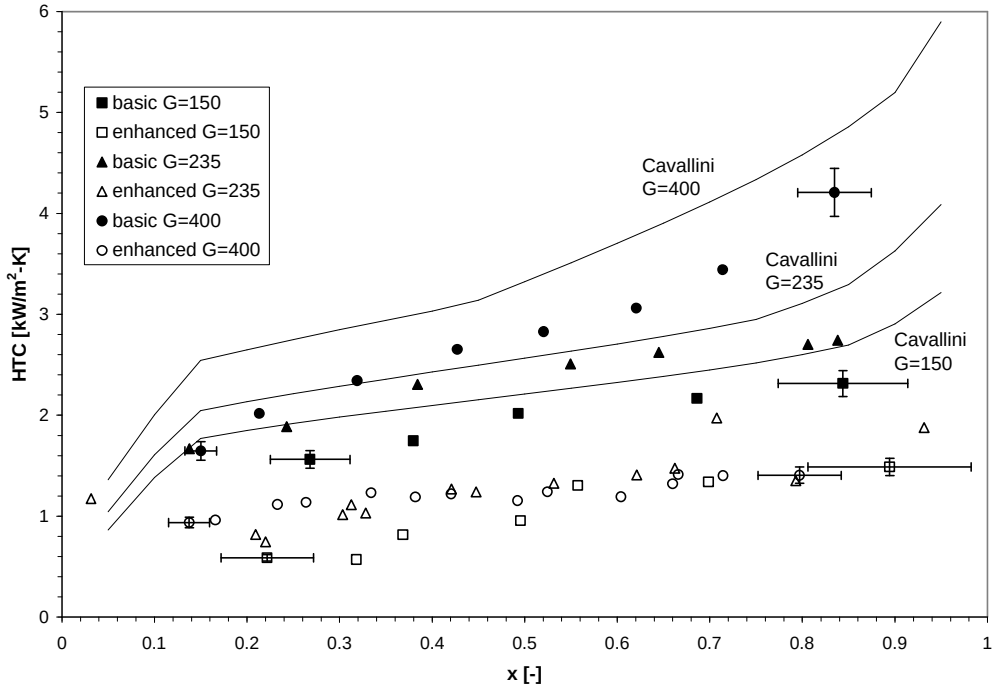

Figure 4.11 Two phase R22 heat transfer with Cavallini correlation (Mass Flux, G, in kg/m^2-s)

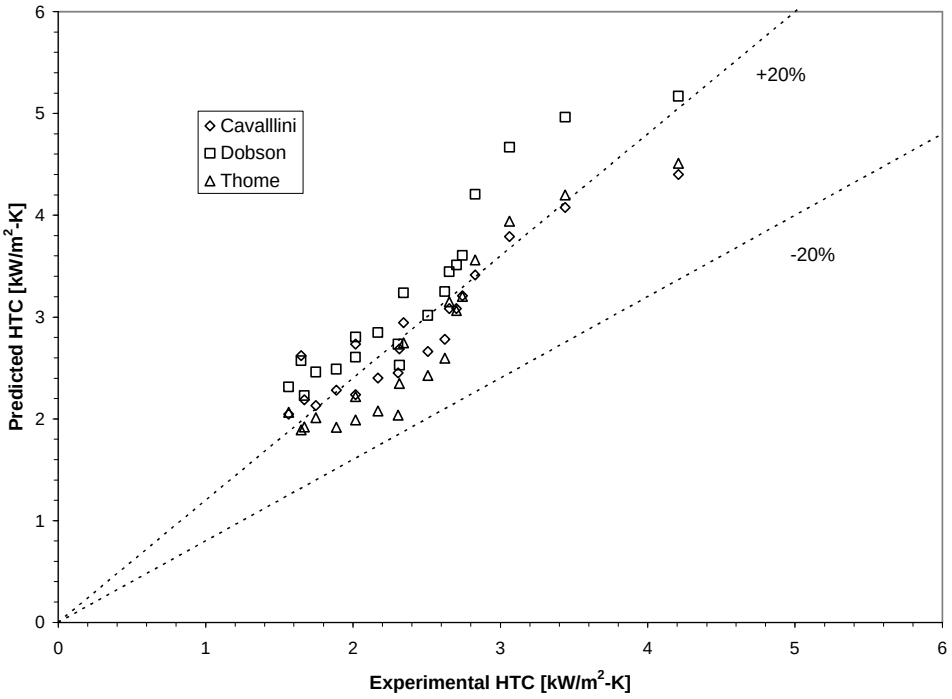

Figure 4.12 Two phase R22 heat transfer correlation smooth tube comparison set I

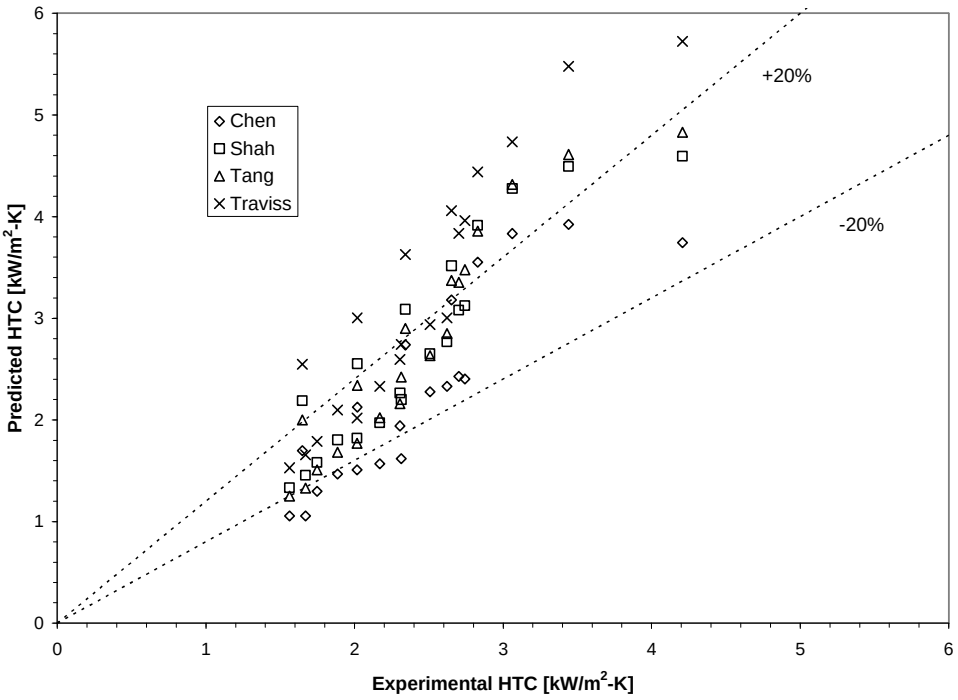

Figure 4.13 Two phase R22 heat transfer correlation smooth tube comparison set II

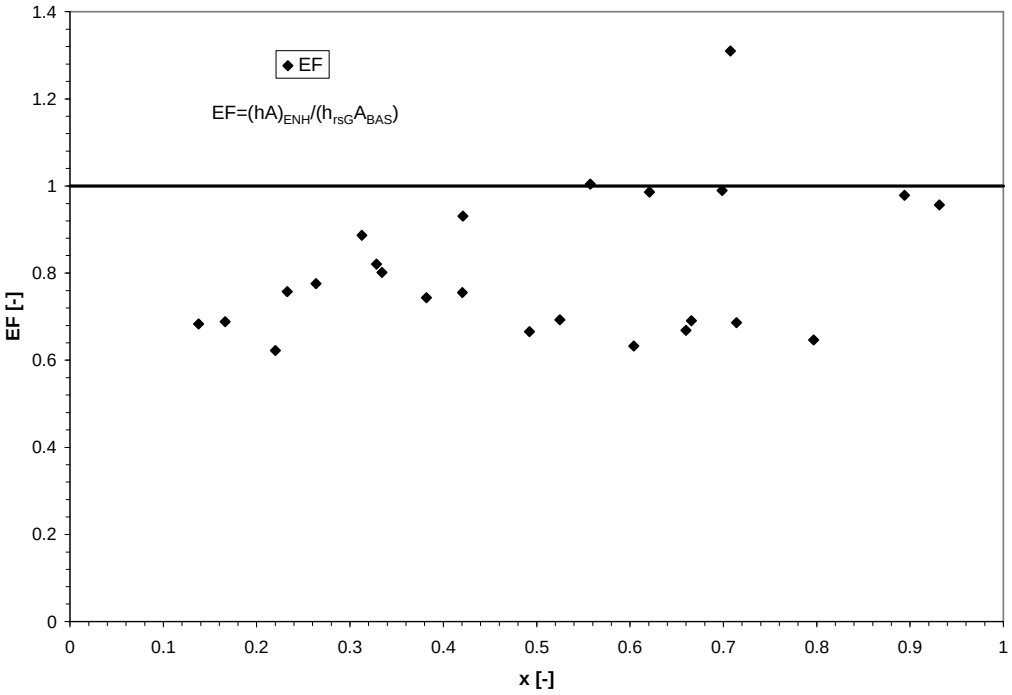

Figure 4.14 Enhancement factor for two phase R22 heat transfer

Chapter 5. Ammonia Condensation Heat Transfer Results

This chapter discusses ammonia condensation heat transfer results in a smooth tube and an enhanced tube. The ammonia results represent a large number of mass flux and quality conditions that have been investigated. Throughout the chapter, several comparisons are made with existing correlations, particularly those presented in the literature review section. Overall, ammonia is found to have high levels of heat transfer coefficient compared to other refrigerants.

5.1 Ammonia Data

Three sets of pure ammonia data have been collected and are discussed in this chapter. The multiple sets of data were collected in order to show repeatability of the tests. The repeated tests were also performed in order to examine the enhanced tube performance more closely. Similar to the R22 condensation heat transfer data, lower heat transfer coefficients were observed on the enhanced tube compared to the smooth tube. Figure 3.1 illustrates that the test sections were placed in parallel positions in the test loop to allow for easier replication of test conditions and shorter time periods between tests. In order to ensure that the different test section locations acted in a similar manner, the test sections were swapped after the completion of the first set of data.

The first set of pure ammonia condensation data was collected with the smooth test section located in the top position, and the enhanced tube test section in the bottom position. The second set of data is the reverse: the enhanced test section in the top position and the smooth tube in bottom position. Although some differences between the two sets of data appear, they do not suggest that the heat transfer coefficients are a function of the location of the tubes. The third data set was collected with new tube test sections. This data set was conducted in order to examine potential differences in the construction of a test section. The smooth test section was in the top test section position, while the enhanced tube test section was in the bottom position. Again, while some differences appear between this set of data and the previous two, the overall trends and characteristics remain very similar. To alleviate confusion when presenting these different data sets, the ammonia data will be presented in four subsections. The first three subsections pertain to each individual set of data, while the fourth compares the three different sets together.

5.1.1 First Set of Ammonia Data

The first set of tubes used to collect this set of ammonia data were also the same set of tubes in which the R22 heat transfer and pressured drop data were collected. The experimentally determined heat transfer coefficients for both the smooth and enhanced tubes from this first set of data appears in Figures 5.1 and 5.2 It is within this set of figures that experimental error bars determined from an uncertainty propagation analysis (Section 3.1.6) are presented. The error bars are only placed on the experimental data points falling at the extremes (i.e. low x, high x) and should be interpolated for the points falling in between. At the low mass fluxes (G=20-80 kg/m^2-s), the condensation heat transfer coefficient is nearly constant throughout the whole range of quality. This is a characteristic of stratified-wavy flows. In fact, looking at the flow maps developed by Cavallini and Thome, (Figures 5.28 – 5.31) both predict that the flow regime would be stratified at these low mass fluxes. At higher mass fluxes, the heat transfer coefficient appears to be a function of both quality and mass flux. This is a characteristic of annular flow.

Figure 5.1 shows that higher mass fluxes (G=160, 270 kg/m^2-K), the condensation heat transfer coefficient appears to decrease at the very high quality range quality range (x>0.8-0.9). This decrease in heat transfer coefficient may be due to the saturation temperature at which these points were taken. All the data collected except for these few high mass flux, high quality conditions were taken at a saturation temperature of 35 ºC. Due to limitations in the flat plate heat exchangers used to preheat and subcool the refrigerant, the data points taken at high mass flux/high quality levels were at elevated saturation temperatures (T_{sat}=40-53 ºC). These elevated temperatures affect both the liquid thermal conductivity and the vapor density of the refrigerant. The liquid thermal conductivity decreases while the vapor density increases as the saturation temperature increases. The combination of these two factors lowers the heat transfer coefficient relative to values expected at 35 ºC saturation temperature. As the vapor density increases, the vapor velocity decreases thus limiting the kinetic energy of the flow. The kinetic energy of the vapor flow is important to two-phase heat transfer, because it is the transfer of this kinetic energy from the vapor to the liquid flow that causes turbulence in the liquid flow. The turbulent motion of the liquid layer is one of the important factors in the heat transfer associated with the flow.

Another important factor affecting heat transfer is within the liquid film. The liquid film can be separated into three regimes: the log region, buffer region, and viscous sublayer. Hurlburt (1999) states that within the viscous sublayer conduction is important. The buffer layer is a region in which conduction across the film layer transitions to heat transfer dominated by turbulent convection. The conduction across the viscous sublayer and into the buffer layer represent the primary thermal resistances of the liquid film layer and control the heat transfer between the tube wall and refrigerant vapor. The liquid thermal conductivity of a fluid is important in that it directly affects the resistance of the liquid conduction. As the liquid thermal conductivity of a refrigerant decreases, the resistance of the viscous sublayer increases, thereby reducing the overall heat transfer coefficient.

Figure 5.2 shows the heat transfer coefficients collected inside the enhanced tube. Unlike the smooth tube results, low mass flux (G=20-80 kg/m^2-s) heat transfer coefficients tend to be a function of both mass flux and quality. At the higher mass fluxes (G=160, 270 kg/m^2-s), the heat transfer coefficients appear to be a function of just quality and not mass flux. These peculiar trends counter those observed in the smooth tube, suggesting that flow regimes for the enhanced tube are quite different from those assumed for a smooth tube.

As observed from Figure 5.2, the heat transfer coefficients are much lower relative to those found for the smooth tube (Figure 5.1). This is much different than expected. The open literature is filled with papers and articles that suggest the heat transfer coefficient of an enhanced tube should closely resemble heat transfer coefficients of smooth tubes with similar dimensions. Wilson (2001) is just one example of this trend. Several thoughts and models were developed to explain this phenomenon.

One explanation that may cause this decrease in heat transfer coefficient is that the liquid may become stagnant in between the fins. The height of the microfins in the enhanced tube is 0.33 mm (0.013”), while the gap between the bases of two adjoining fins is approximately 0.20 mm (0.008”). This is quite an increase in both fin height and gap width to what was found in the open literature. Typical microfin heights are on the order of 0.1-0.2 mm (0.004-0.008”), while the distance between two fin bases is often negligible (based off a triangular type geometry). The relatively large fin height and gap spacing may cause the liquid to stagnate between each fin. This

stagnant liquid is detrimental to heat transfer in two ways. First, the liquid layer acts as an additional conduction resistance. Because a refrigerant's conductive resistance is greater than its convective resistance, this causes the overall resistance to increase thereby decreasing the overall heat transfer coefficient. In addition to an increased thermal resistance layer, a stagnated liquid layer could cover a certain amount of tube wall surface area. The effective tube wall surface area is reduced, consequently reducing the overall heat transfer coefficient. By stagnating fluid in this gap, a third phenomenon may also occur. If the majority of the liquid phase is buried in the gap between the relatively high microfins, the fin tips can protrude into the vapor core of the two-phase flow. Contact between the fin tips and the vapor core may result in a single-phase vapor heat transfer coefficient for that portion of the surface area. Because single-phase heat transfer coefficients are less than two phase coefficients, this would also lead to a decrease in the overall heat transfer coefficient.

Figures 5.3 and 5.4 show how well the existing correlations predict the experimental data gathered on the smooth tube. Figure 5.3 contains three correlations that are dependent on flow regime. These correlations are from Cavallini (2002), Dobson (1994), and Thome (2003). All three correlations tend to consistently overpredict the experimental data. It appears that the Cavallini correlation predicts the best overall. In particular is its ability to accurately predict the lower heat transfer coefficients (0-5 kW/m^2-K). It is also the most consistent correlation in terms of the higher coefficients (h>5 kW/m^2-K). The Dobson correlation appears to perform the worst.

Plotted in Figure 5.4 are the heat transfer correlations that were developed on models based on annular flow characteristics. Included in these correlations are the Chen (1966), Shah (1979), Tang (1997), and Traviss (1973). The general trend observed from this plot is that all four correlations underpredict the low experimental heat transfer coefficients (0-6 kW/m^2-K) and then increase discontinuously to overpredict the data at higher heat transfer coefficients. This is probably caused by the limitation of only being able to predict annular flow characteristics. As the experimental data approaches high heat transfer coefficients (h>14 kW/m^2-K), the correlations developed by Tang and Traviss tend to drastically overpredict the data. Overall, the Chen and Shah correlations perform the best, yet they exhibit an inconsistent trend in that at low experimental coefficients, they underpredict, while at higher coefficients, they overpredict. A comparison of Figures 5.3 and 5.4 shows that the flow regime based correlations perform better in that they consistently overpredict the data.

Figure 5.5 shows the enhancement factor for the first set of experimental data.

$$EF = \frac{hA}{hA_{rsG}} \tag{5.1}$$

An enhancement factor is a commonly used method of comparing the effect of internal surface area enhancements on the heat transfer results from two different tubes. In this case the smooth round tube is used as the common reference. In the above equation h_{rsG} is the heat transfer coefficient calculated using an adjustment of a condensation heat transfer correlation for the two phase data points. The most accurate of the three flow regime based correlations (Cavallini, Dobson, or Thome) in terms of predicting the smooth tube heat transfer coefficient is used. The correlation is then adjusted by multiplying by a constant so that the enhancement factor of the smooth tube is approximately one.

Figure 5.5 shows that overall; the enhanced tube performs worse than the basic tube in terms of heat transfer. An enhancement factor of unity would show that both tubes perform equally well. Wilson (2002) reports that enhancement factors of round tubes should closely resemble the ratio of the enhanced surface area over the smooth surface area when the heat transfer coefficients are similar between the two tube types. From this manner of thinking, the enhancement factors in Figure 5.5 should be 2.0-2.2. Low enhancement factors are caused by the low enhanced heat transfer coefficients relative to those on the smooth or basic test section. A multiplication factor of 0.76 was applied to the Cavallini correlation to relate the enhanced tube to the smooth tube results.

5.1.2 Second Set of Ammonia Data

The smooth tube heat transfer results for the second set of data appears in Figure 5.6. Figure 5.6 shows the same general trends observed in Figure 5.1 for the first set of data. In particular, the heat transfer coefficients taken at the low mass fluxes (G=20-80 kg/m^2-s) appear to be more of a function of mass flux, not quality. This again suggests that the flow is in a stratified flow regime. At the higher mass fluxes (G=160, 270 kg/m^2-s), the upward trend of the heat transfer coefficients throughout the range of quality suggests that the flow was in an annular flow regime. This coincides with Cavallini's and Thome's flow maps (Figures 5.28-5.31). The experimental points taken at the higher mass fluxes (G=160, 270 kg/m^2-s) and higher qualities (x>0.7) were taken at saturation temperatures that were higher (40-53 ºC) than the usual saturation temperature of 35 ºC.

The corresponding heat transfer data captured for the enhanced tube is located in Figure 5.7. Comparing Figures 5.7 and 5.2, it is observed that the second set of heat transfer coefficients data (Figure 5.7) corresponds greatly with those gathered in the first set of data (Figure 5.2). This consistency between sets suggests that the location of the test section (either on top or bottom) does not have an effect on the overall heat transfer coefficients measured. The second set of enhanced tube heat transfer data also backs up the initial set of enhanced data, reinforcing the idea that fin geometry is playing a role in limiting the overall heat transfer coefficients.

Figures 5.8 and 5.9 illustrate how well the existing condensation correlations compare to the experimental data. Figure 5.8 includes the three correlations based on flow regimes, while Figure 5.9 depicts correlations based on the annular flow regime characteristics. The predictability of this set of data is consistent with that of the first set of data, indicating consistency between the data sets with different locations in the test loop facility. In Figure 5.8, all three correlations (Thome, Cavallini, and Dobson) appear to perform in a similar manner. All three correlations tend to consistently overpredict the experimental data. In Figure 5.9, the four correlations (Chen, Shah, Tang, Traviss) display systematic deviations from the experimental results due to the correlations' inability to characterize the flow field. Figure 5.10 shows the enhancement factor for the second set of experimental data. Figure 5.10 reveals that the enhanced tube performs much worse than the smooth tube. All of the experimental data points fall below unity or one, similar to what was observed in the first data set (Figure 5.5). Overall, the enhancement factors from the second set of data appear similar to those attained from the first set of data. The first and second data sets reinforces the premise that test section location does not play a role on the evaluation of heat transfer coefficients. A correction factor of 0.75 was applied to the Cavallini correlation to nominalize the smooth tube heat transfer coefficient.

5.1.3 Exploration of Tube Consistency

After completion of the first two sets of ammonia data, the test sections were removed from the experimental facility. The enhanced test section was then analyzed qualitatively for any blemishes within the internal geometry that may have caused the lower then expected heat transfer coefficients. This analysis revealed that a thin coating had formed along the wall surface. To further analyze this film, a more detailed chemical spectrography test was done on the test sections. A clean tube section was also analyzed in addition to the used test section. Results for the tests are plotted in Figures 5.11 and 5.12. Figure 5.11 depicts the clean tube, while results from the dirty or used tube are shown in Figure 5.12. The main discrepancy between the two tests is the high amount of chlorine observed in the dirty tube (Figure 5.12), while little or no chlorine was seen in the clean tube (Figure 5.11). One possible explanation for this is that the used test sections were also used in the R22 condensation tests just prior to the ammonia condensation tests. Perhaps some of the chlorine from the R22 ($CHClF_2$) was absorbed into some of the flow loop materials. This buildup of chlorine, forming some aluminum chloride compounds, appears to be the main component of the film. One concern was that the existence of this film may or may not alter the condensation heat transfer characteristics of ammonia. New clean test sections were constructed and a third round of pure ammonia tests was collected. Also, a short section of aluminum tube was placed in the test loop such that it could periodically be removed for inspection. No additional buildup of a film layer ahs been observed since the original test sections were removed.

5.1.4 Third Set of Ammonia Data

The third set of ammonia data was taken on different set of tube test sections. Heat transfer data taken on the smooth tube appears in Figure 5.13. Figure 5.13 is in reasonable agreement with results from the first and second data sets (Figures 5.1 and 5.6). All the data points have similar trends. This consistency shows that the heat transfer coefficients are independent of individual test sections.

Figure 5.14 shows the third set of data taken on the enhanced tube. This set of data shows that heat transfer coefficients tend to be a little higher than those observed in the first two sets of data (Figure 5.2 and 5.7). Despite the elevated coefficients, the difference between Figure 5.14 and the first two sets is quite small (approximately 0.4 kW/m^2-K). The difference between the third data set and the first two data sets could be caused by an error in the wall temperature calibration measurements. Despite this variation between the data sets, the heat transfer coefficients follow the same general trend discussed in section 5.1.1.

Figures 5.15 and 5.16 compare the experimental data with the data generated from several correlations. Figure 5.15 shows the agreement between the data and flow regime correlations. These correlations are the Cavallini, Dobson, and Thome. All three correlations tend to consistently overpredict the experimental data throughout the entire range of heat transfer coefficients. This is very similar to what was observed in the first set of data. Overall, it appears that the Cavallini or the Thome correlation tends to do the best job, while the Dobson performs the worst among the three. Figure 5.16 shows how well the annular flow regime correlations perform. Included in these correlations are the relations from Chen, Shah, Tang, and Traviss. Again, similar to the first and second set of data, these correlations are systematically scattered when compared to the experimental data.

5.1.5 Direct Mass Flux (G) Comparison

This subsection serves as a direct comparison of the three sets of data at the different mass fluxes. The first set of figures (Figures 5.17-5.21) compares the data sets taken on the smooth tube. All five plots show that the three sets of data are very consistent with each other. The second set of figures (Figures 5.22-5.26) examines the data sets taken on the enhanced tube. In all five plots, the third set of data was observed to be consistently greater than the previous two sets. Referring to section 5.1.3, this could have been caused by an error in calibration of the tube wall temperature thermocouples or possibly the chloride film/corrosion.

5.2 Figures

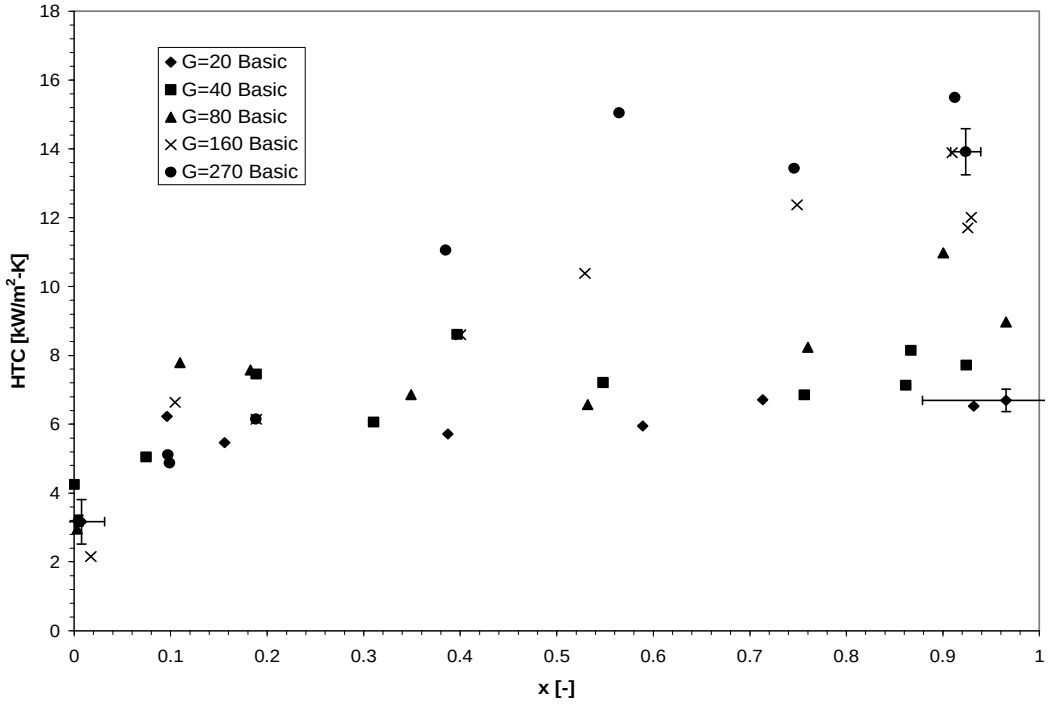

Figure 5.1 Heat transfer coefficients for first set of ammonia data for the smooth tube (Mass Flux, G, in kg/m^2-s)

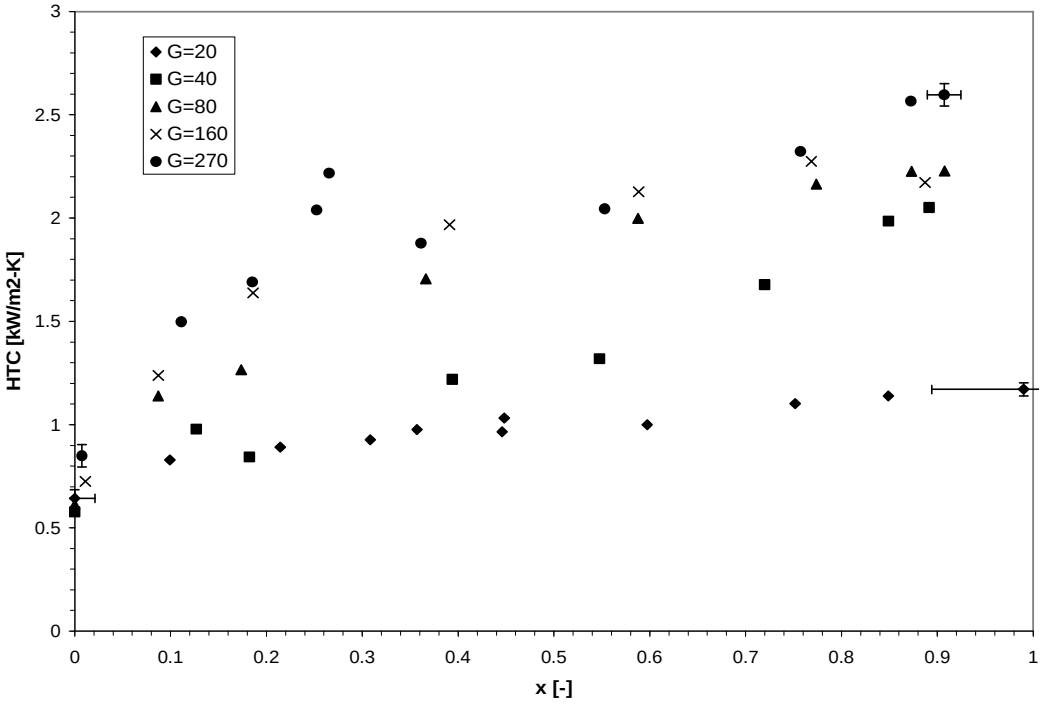

Figure 5.2 Heat transfer coefficients for first set of ammonia data for the enhanced tube (Mass Flux, G, in kg/m^2-s)

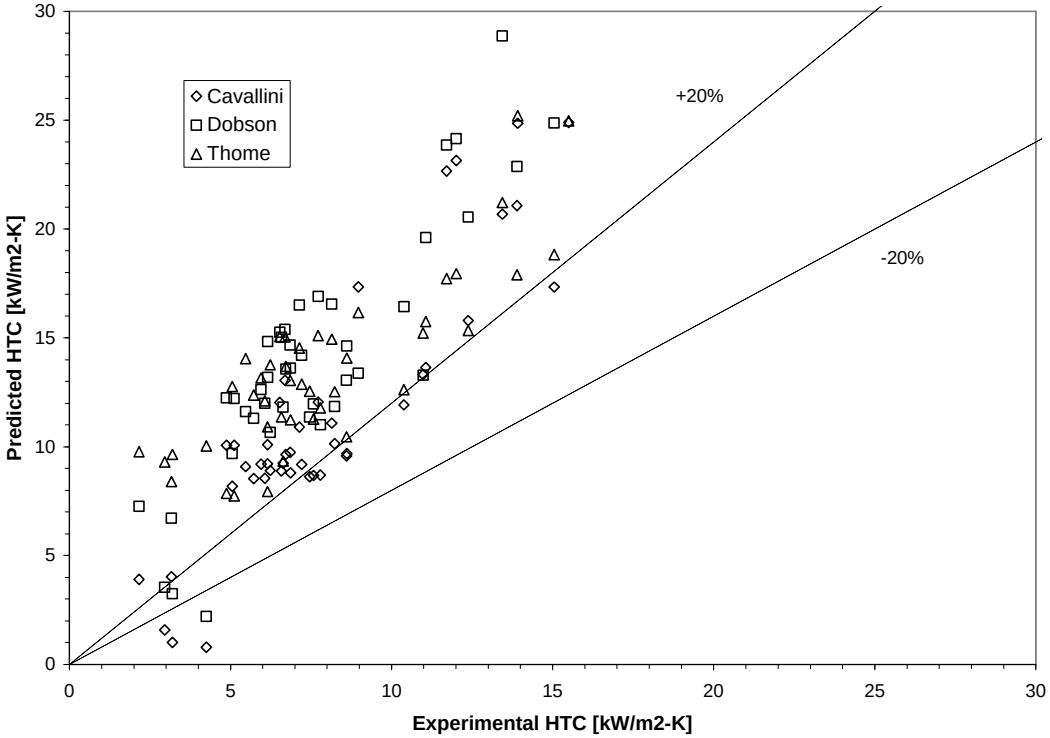

Figure 5.3 First set of ammonia data, smooth tube, correlation set I

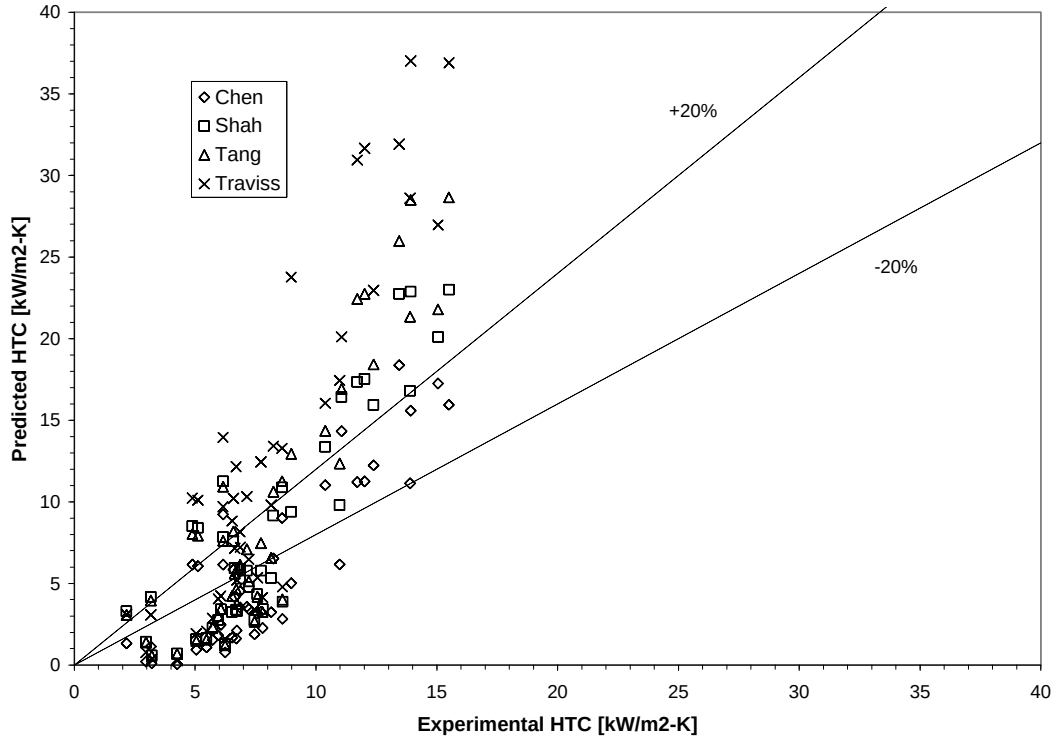

Figure 5.4 First set of ammonia data, smooth tube, correlation set II

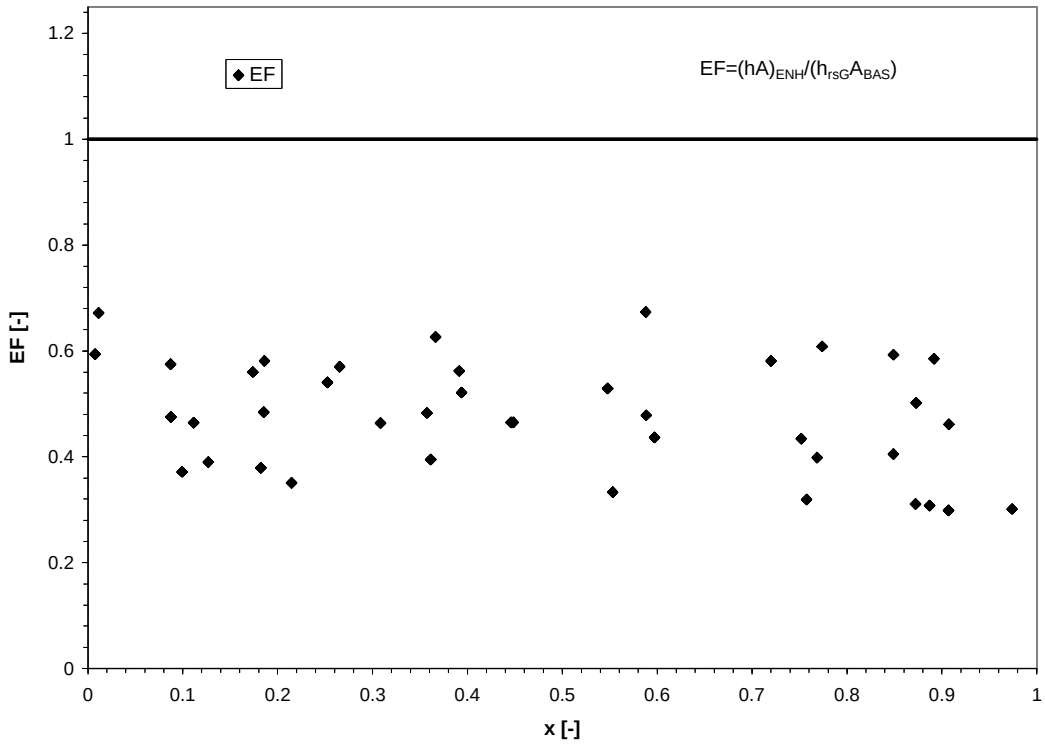

Figure 5.5 Enhancement factor for first set of ammonia data

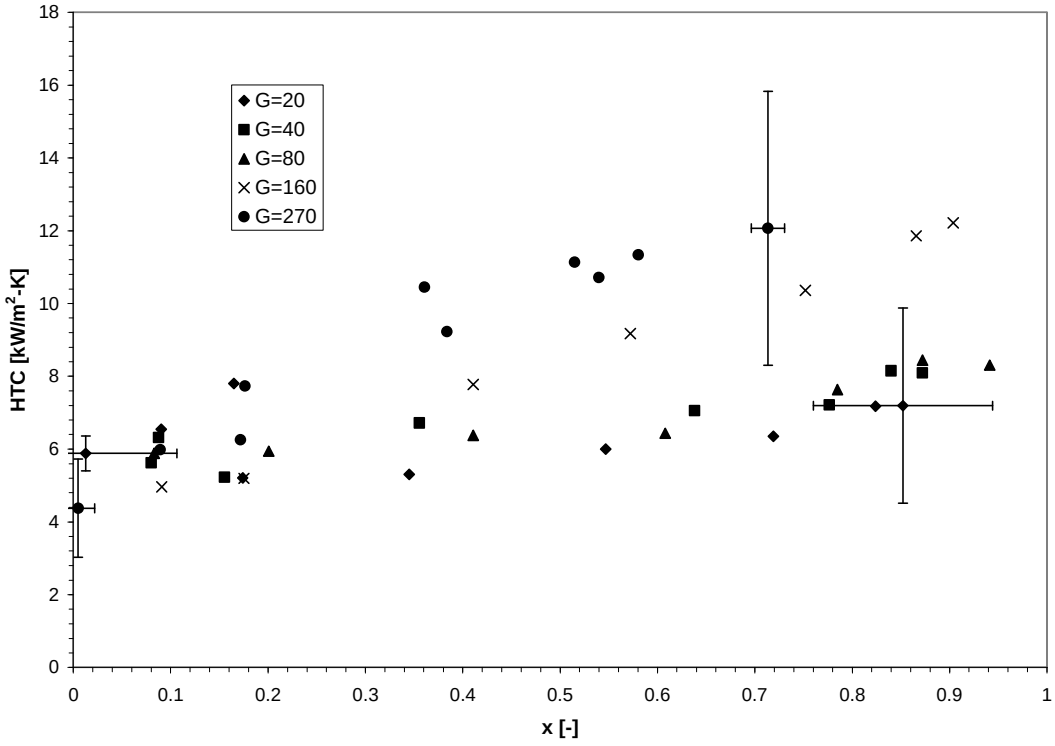

Figure 5.6 Heat transfer coefficients for second set of ammonia data for the smooth tube (Mass Flux, G, in kg/m^2-s)

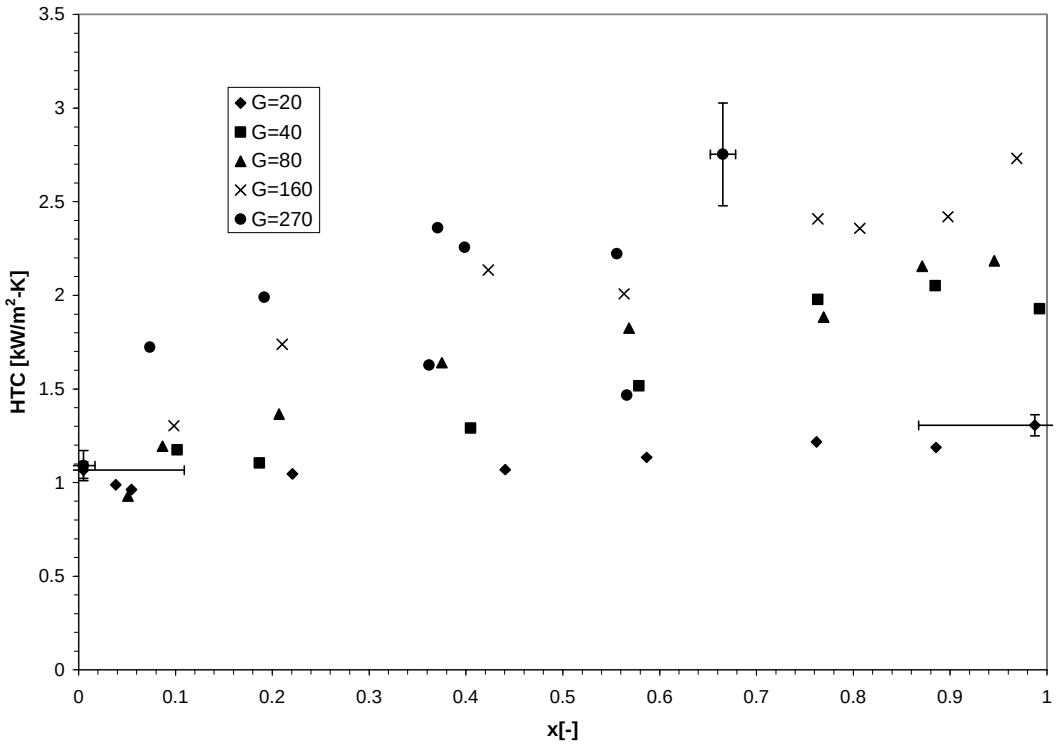

Figure 5.7 Heat transfer coefficients for second set of ammonia data for the enhanced tube (Mass Flux, G, in kg/m^2-s)

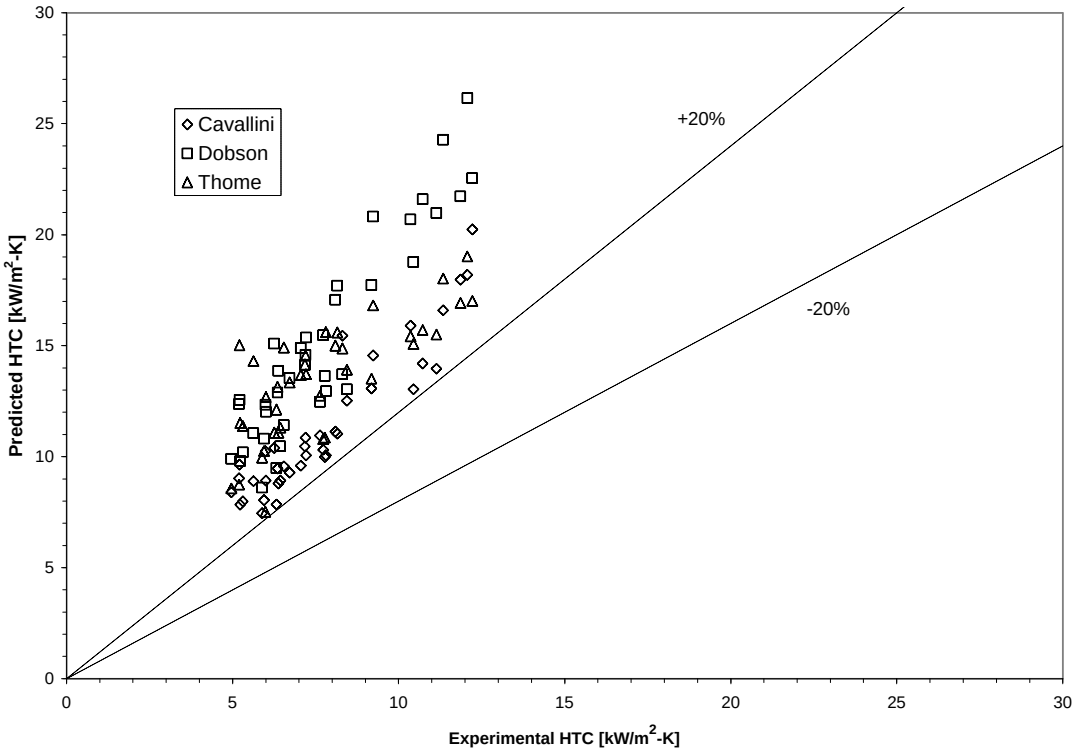

Figure 5.8 Second set of ammonia data, smooth tube, correlation set I

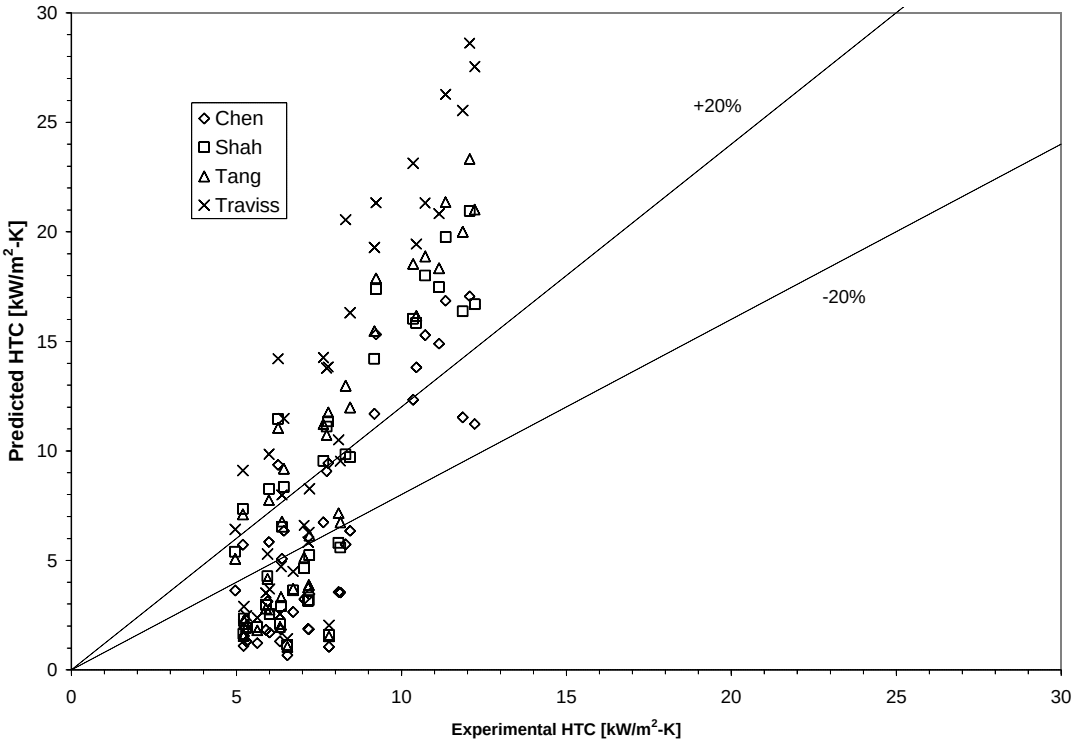

Figure 5.9 Second set of ammonia data, smooth tube, correlation set II

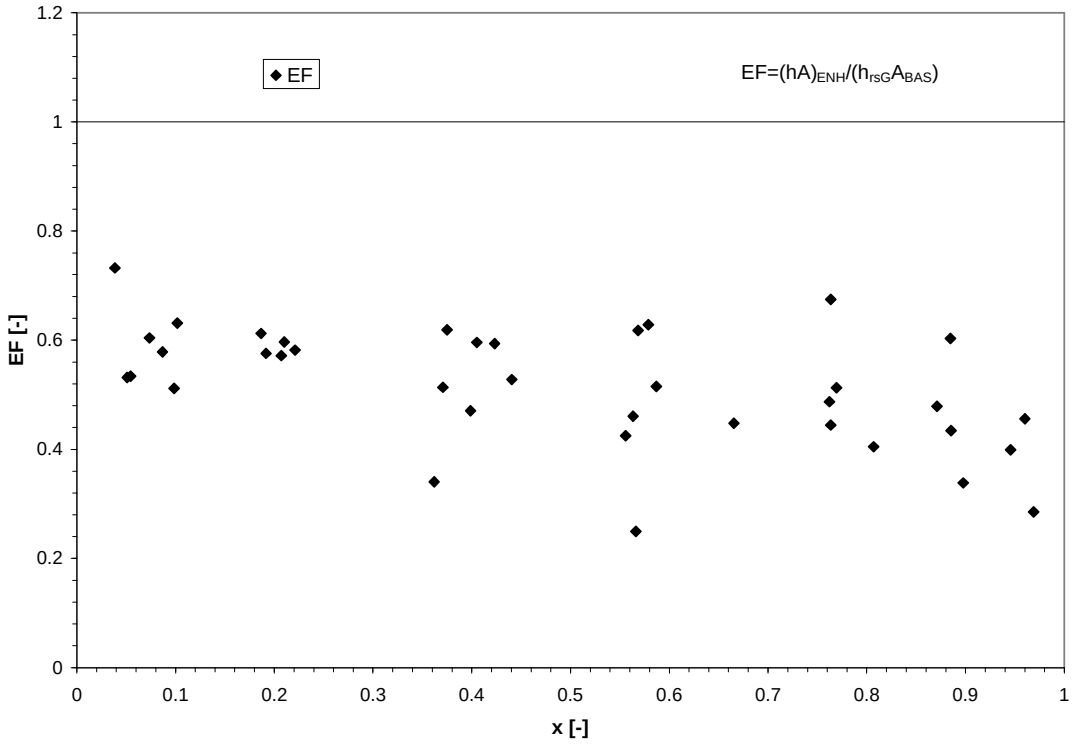

Figure 5.10 Enhancement factor for second set of ammonia data

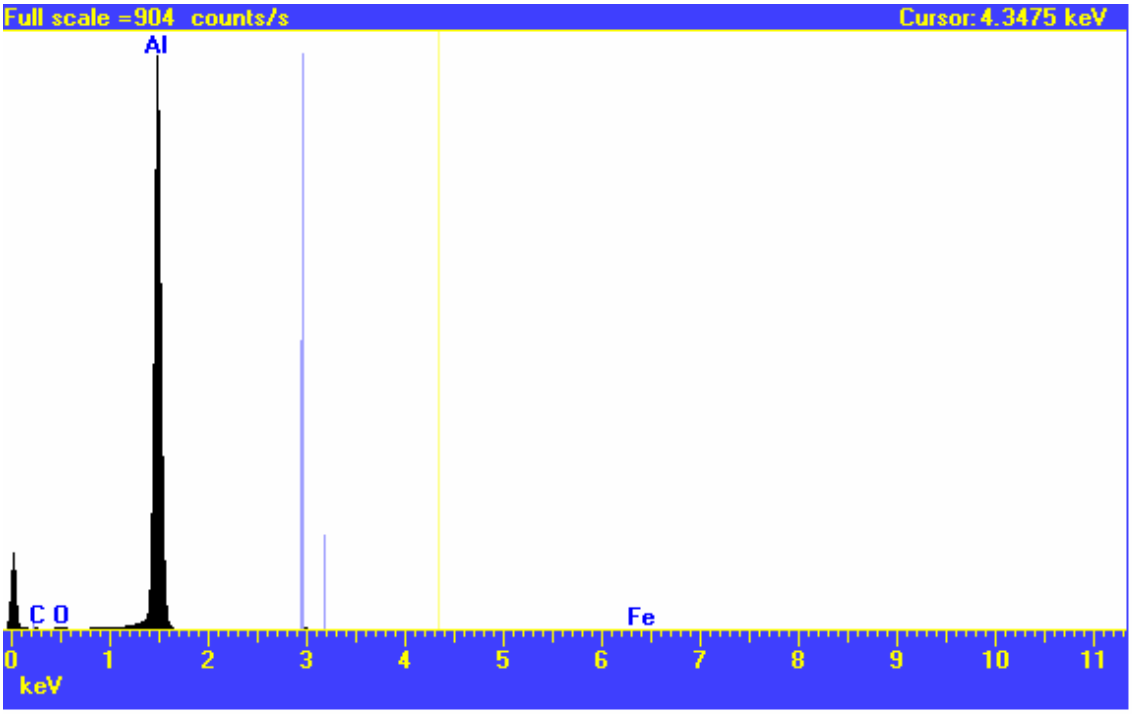

Figure 5.11 Spectrographic analysis of clean aluminum test section

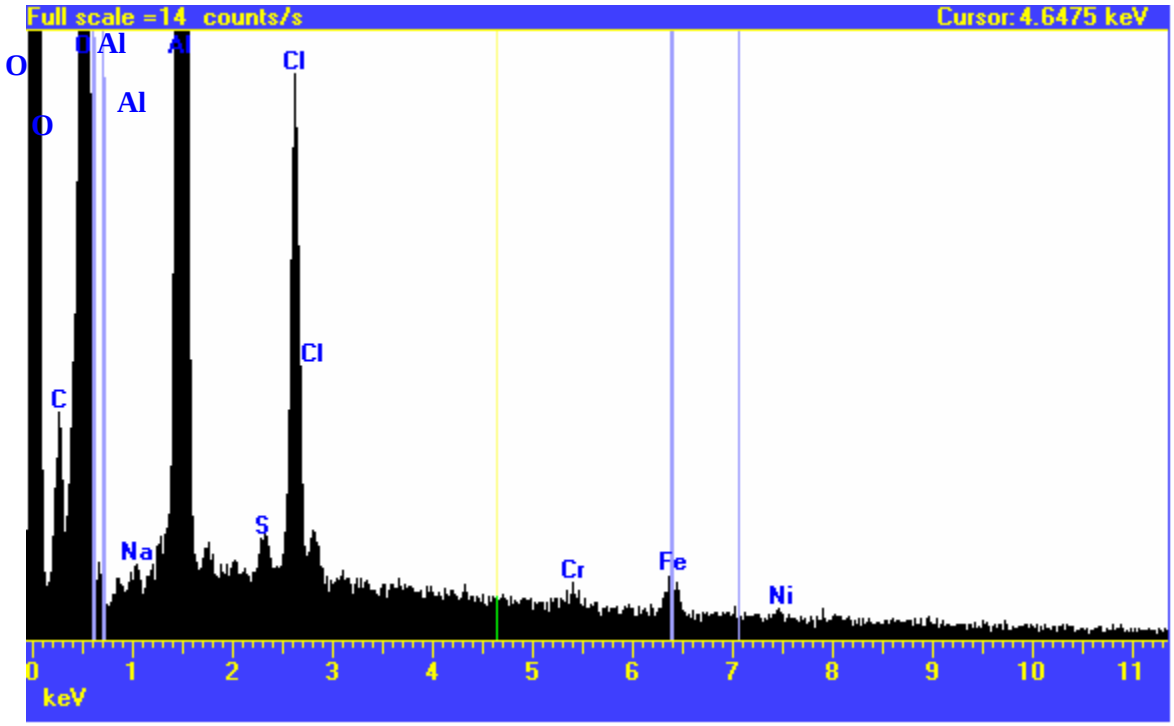

Figure 5.12 Spectrographic analysis of used (dirty) aluminum test section

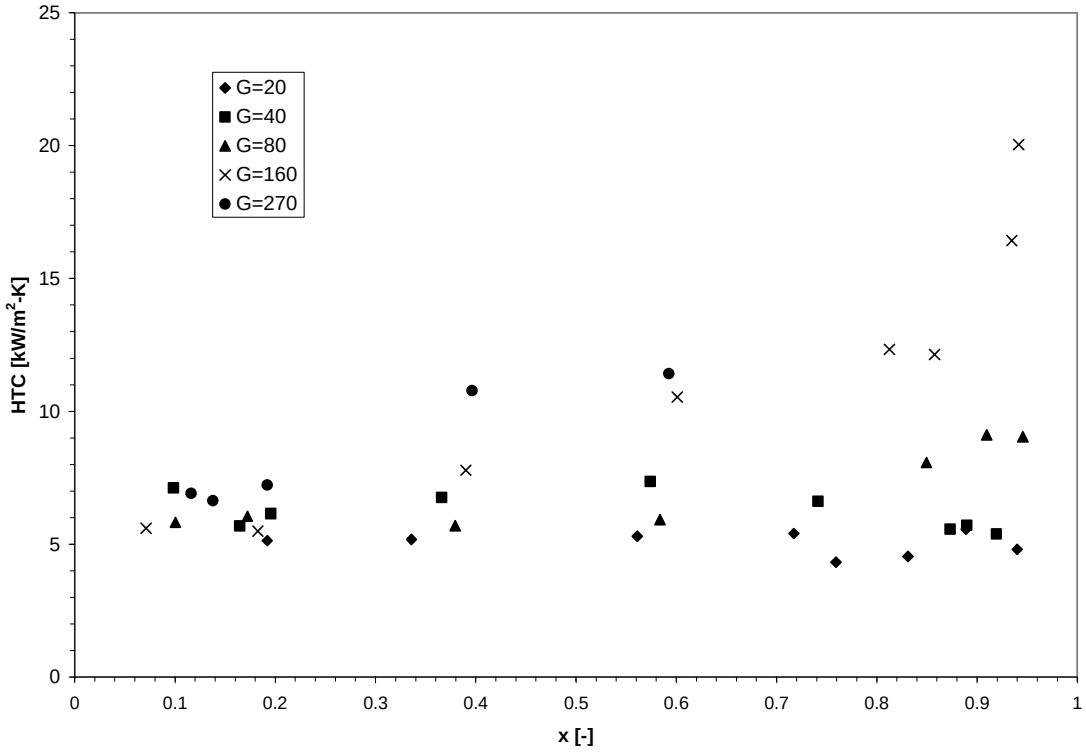

Figure 5.13 Heat transfer coefficients for third set of ammonia data for the smooth tube (Mass Flux, G, in kg/m^2-s)

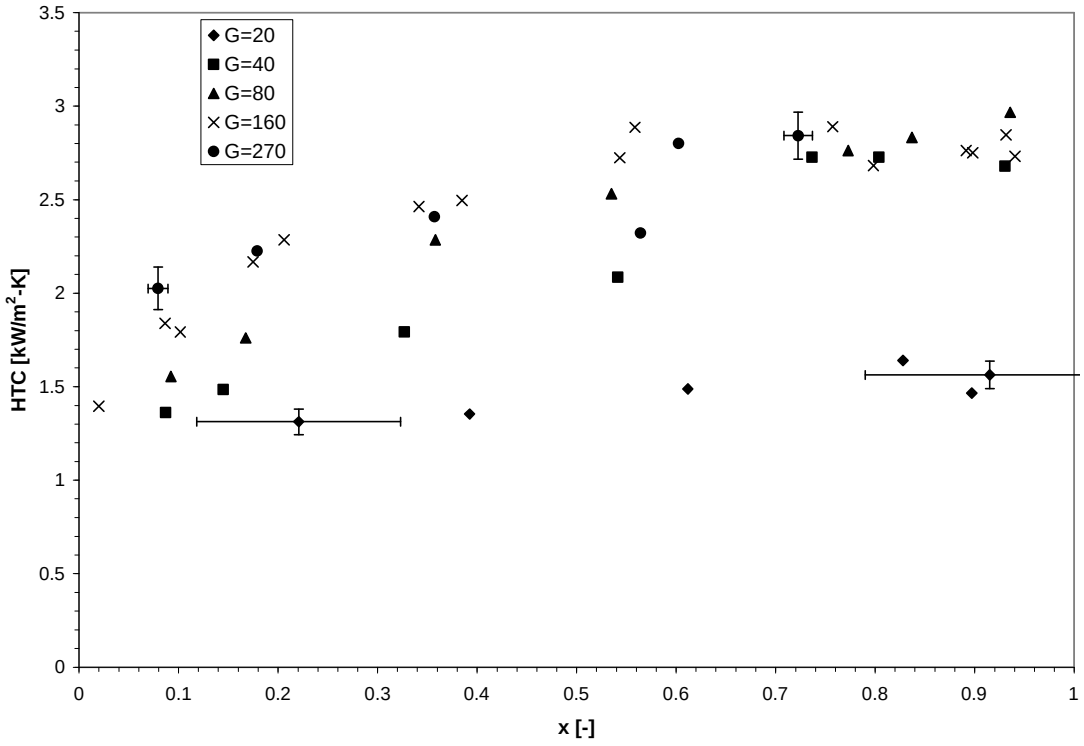

Figure 5.14 Heat transfer coefficients for third set of ammonia data for the enhanced tube (Mass Flux, G, in kg/m^2-s)

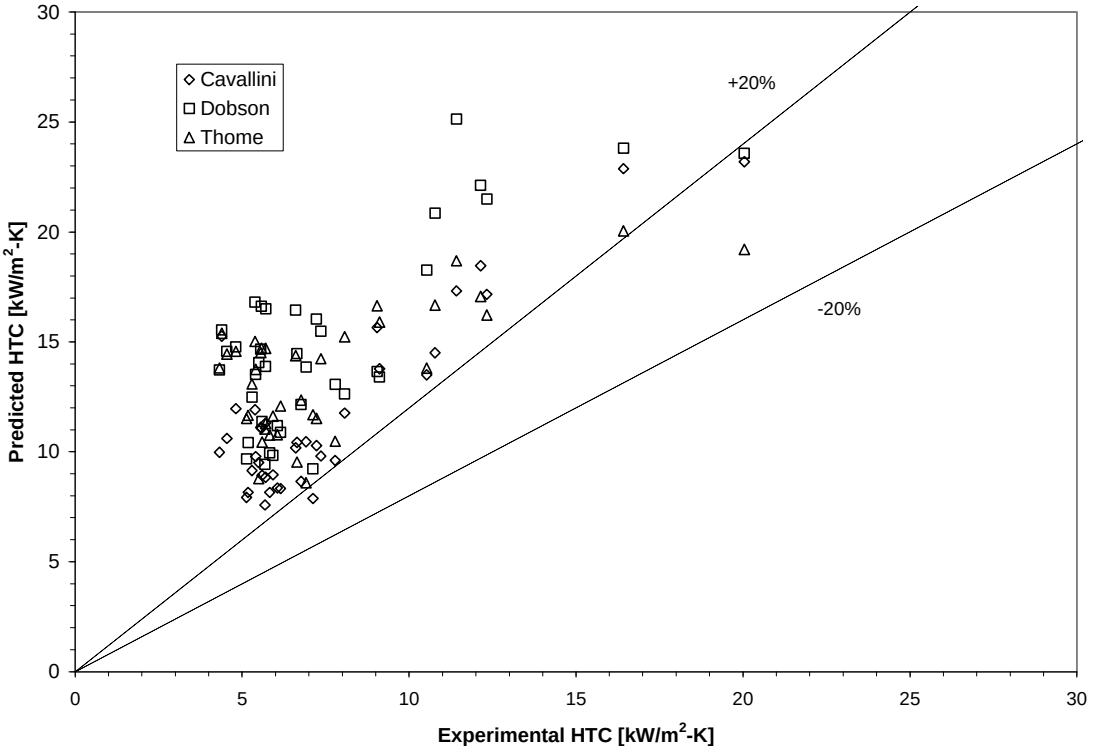

Figure 5.15 Third set of ammonia data, smooth tube, correlation set I

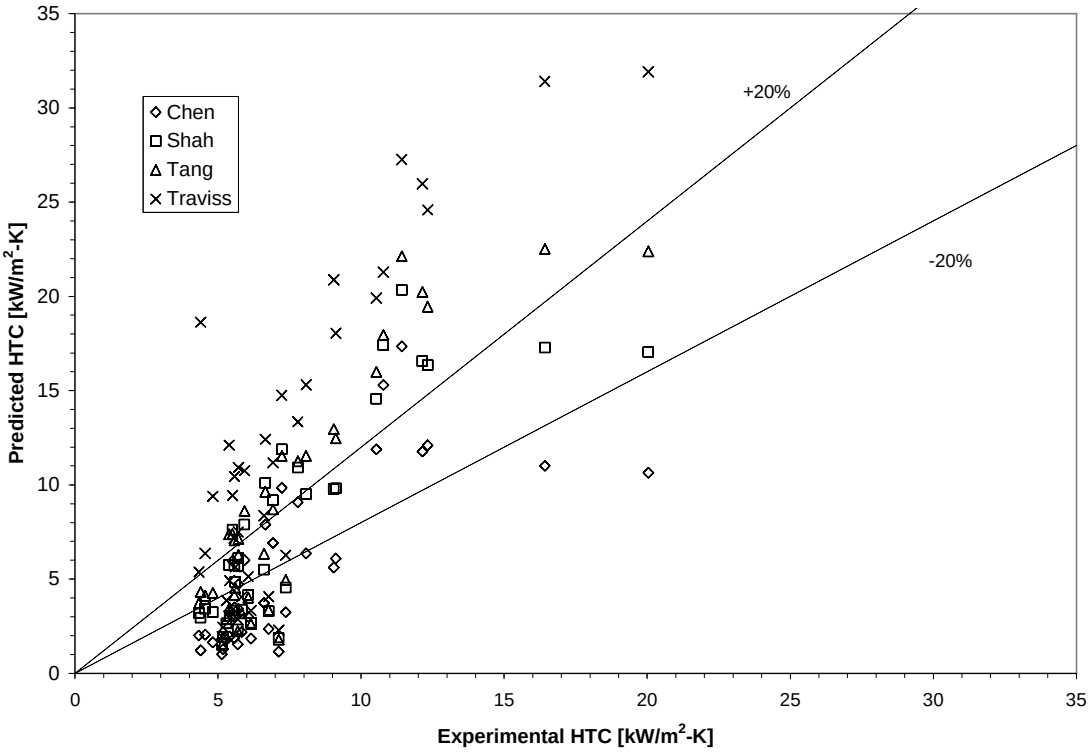

Figure 5.16 Third set of ammonia data, smooth tube, correlation set II

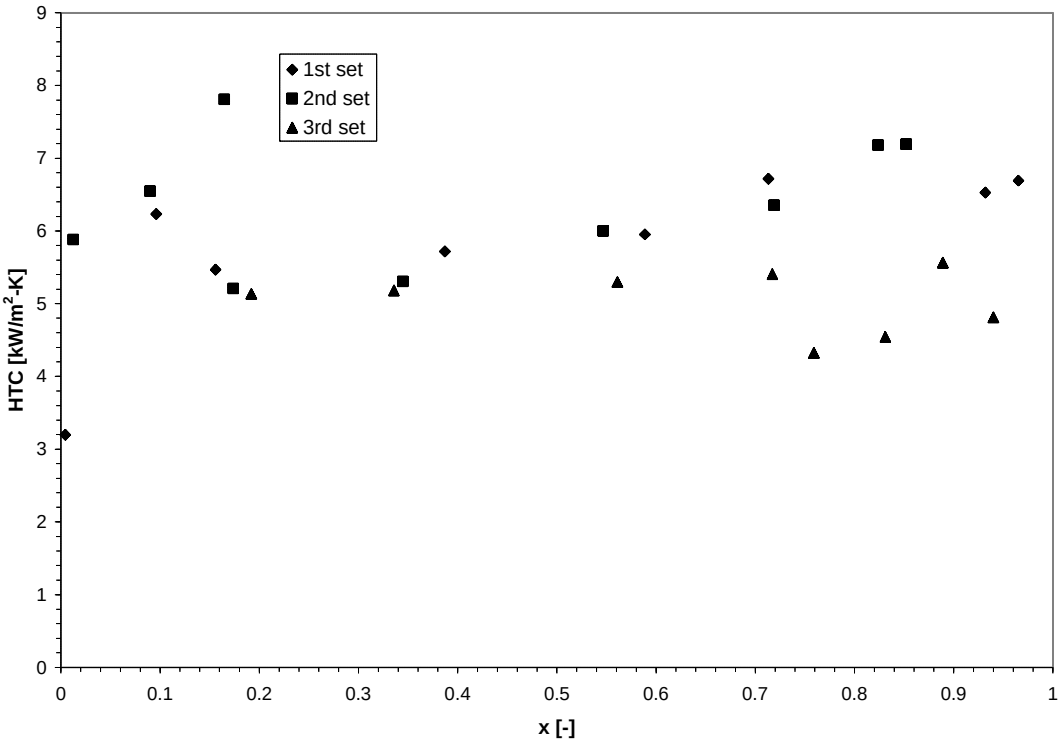

Figure 5.17 Smooth tube, comparison of heat transfer coefficient sets, G=20 kg/m^2-s

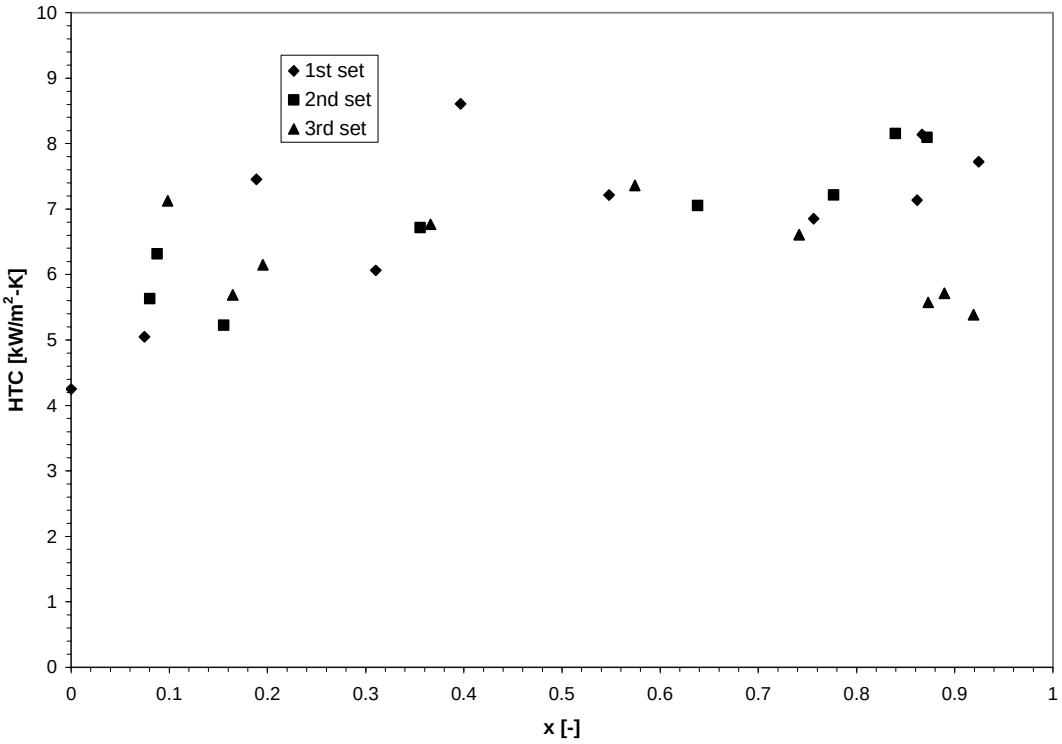

Figure 5.18 Smooth tube, comparison of heat transfer coefficient sets, G=40 kg/m^2-s

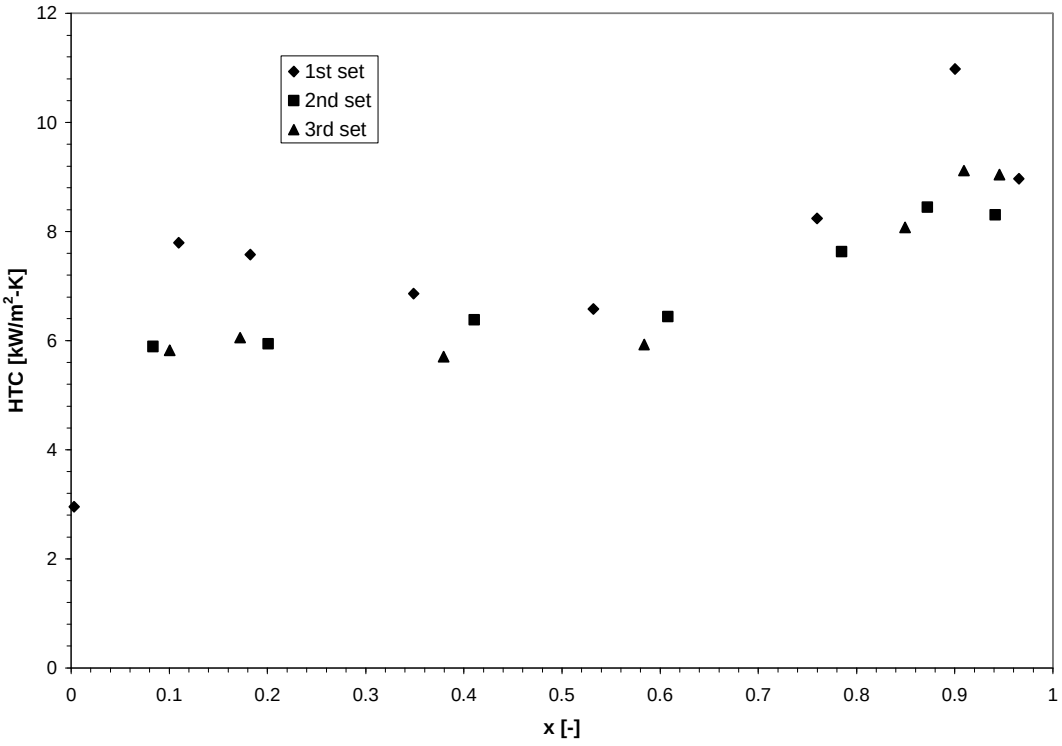

Figure 5.19 Smooth tube, comparison of heat transfer coefficient sets, G=80 kg/m^2-s

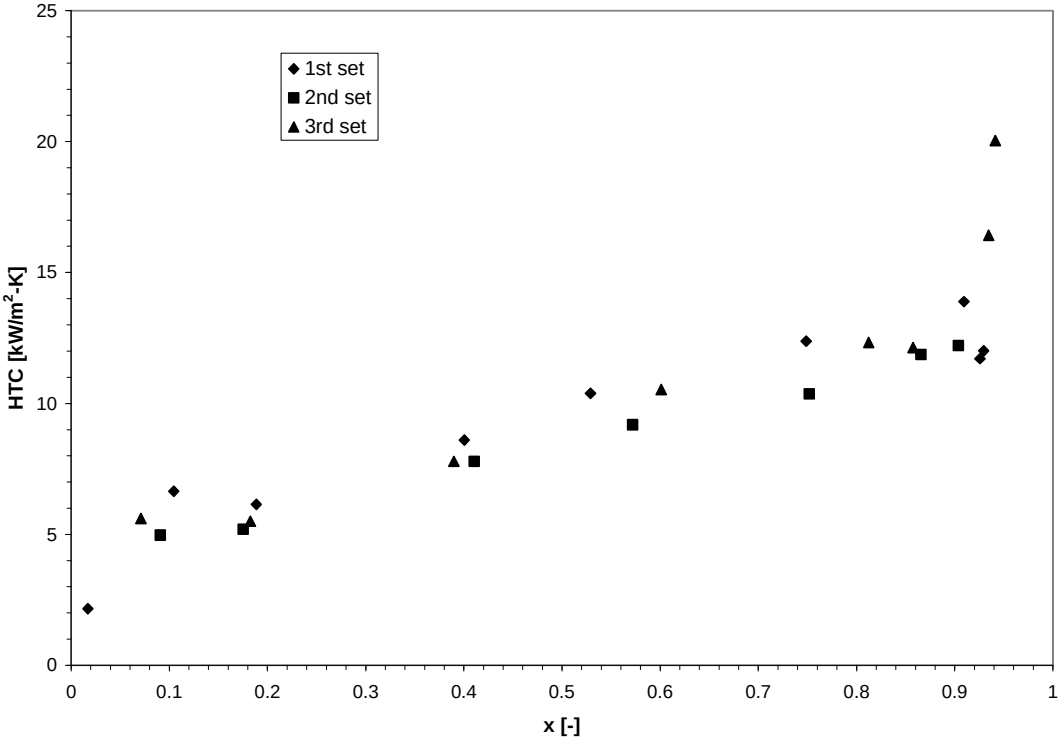

Figure 5.20 Smooth tube, comparison of heat transfer coefficient sets, G=160 kg/m^2-s

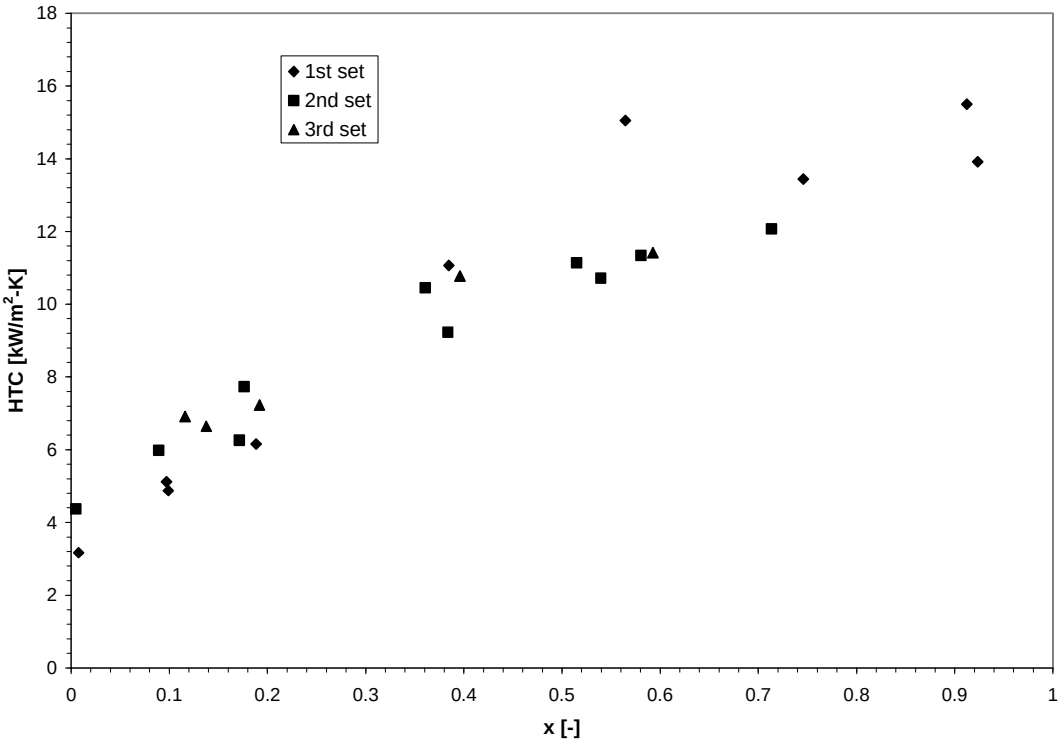

Figure 5.21 Smooth tube, comparison of heat transfer coefficient sets, G=270 kg/m^2-s

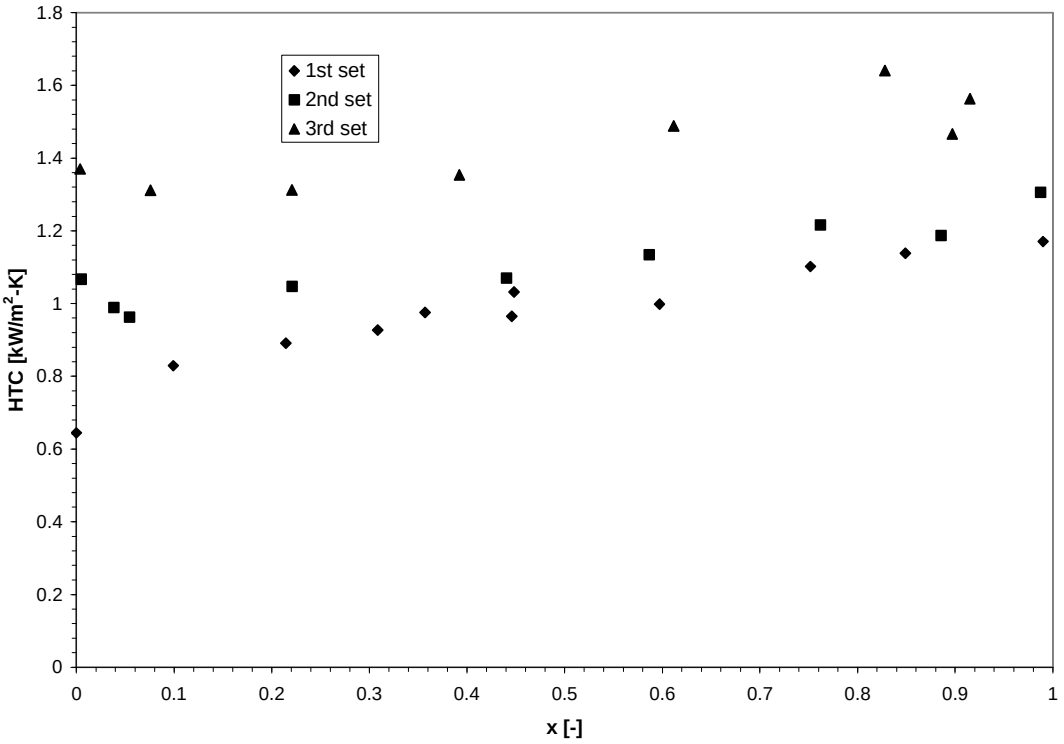

Figure 5.22 Enhanced tube comparison of heat transfer coefficient sets, G=20 kg/m^2-s

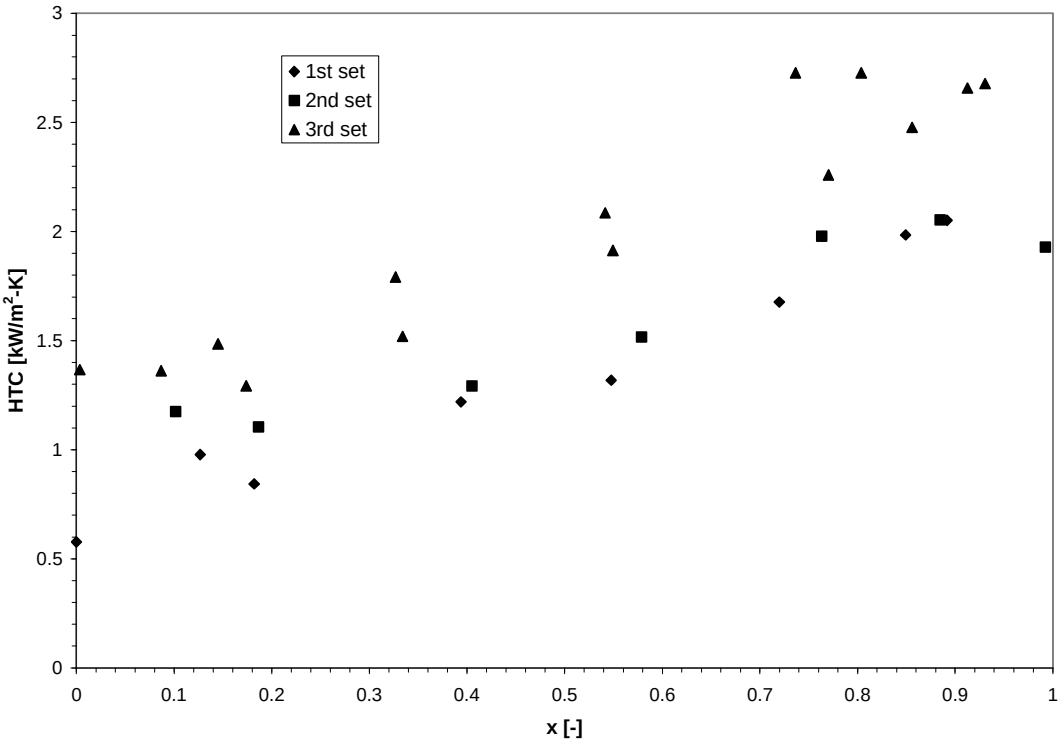

Figure 5.23 Enhanced tube, comparison of heat transfer coefficient sets, G=40 kg/m^2-s

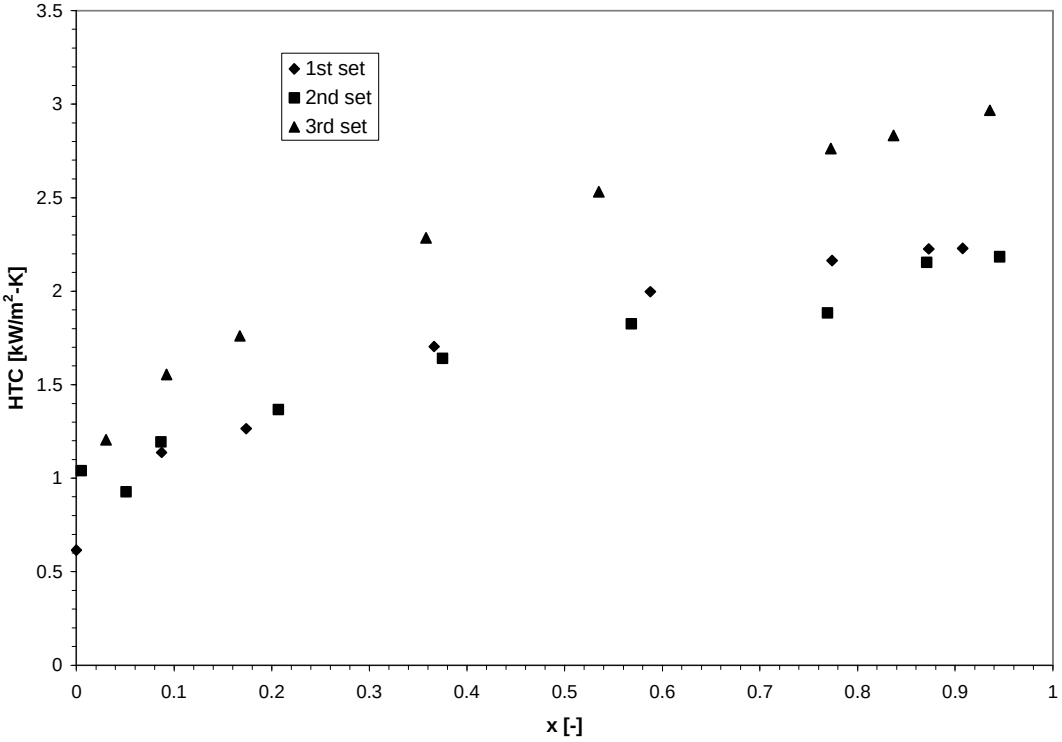

Figure 5.24 Enhanced tube, comparison of heat transfer coefficient sets, G=80 kg/m^2-s

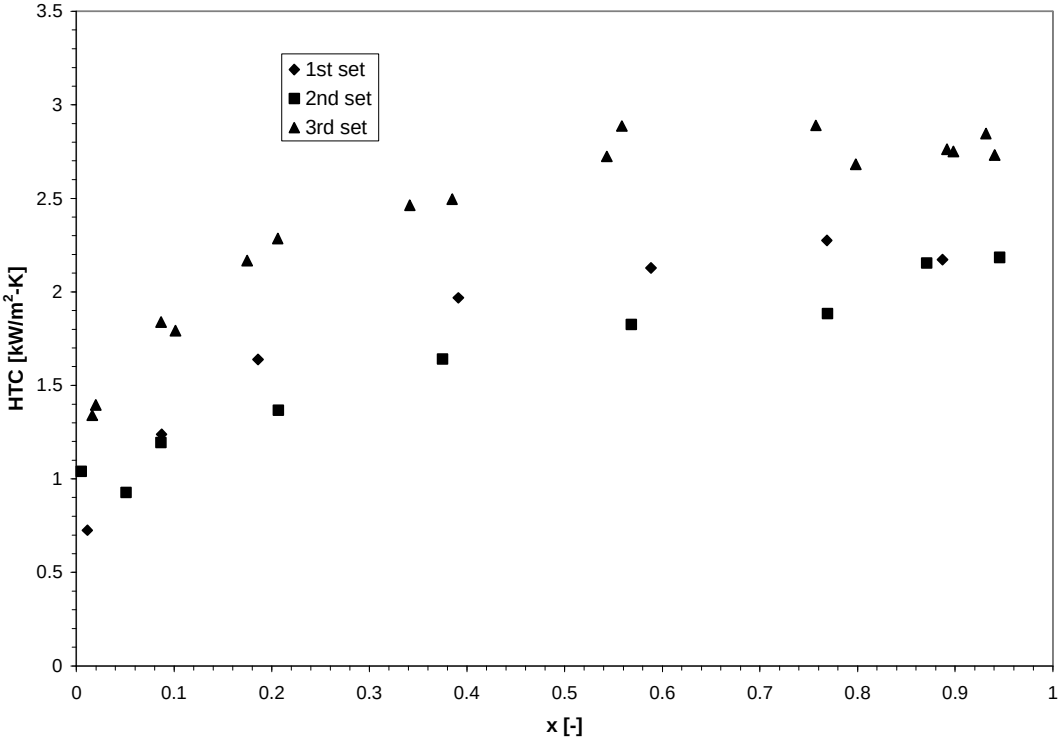

Figure 5.25 Enhanced tube, comparison of heat transfer coefficient sets, G=160 kg/m^2-s

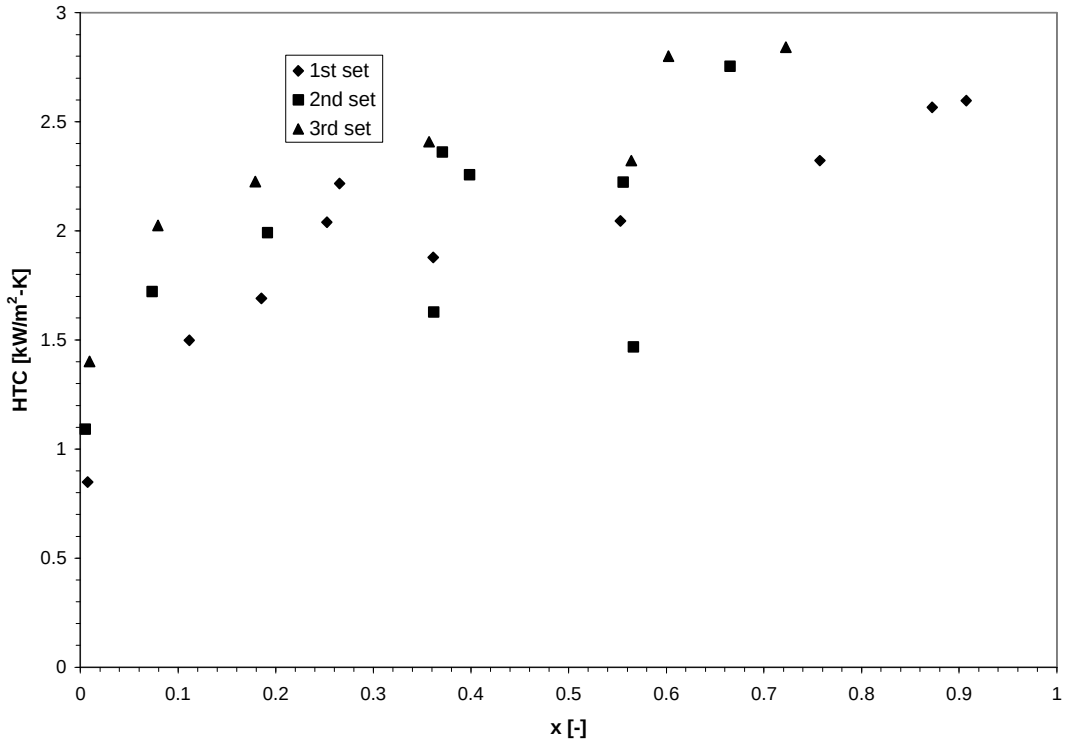

Figure 5.26 Enhanced tube, comparison of heat transfer coefficient sets, G=270 kg/m^2-s

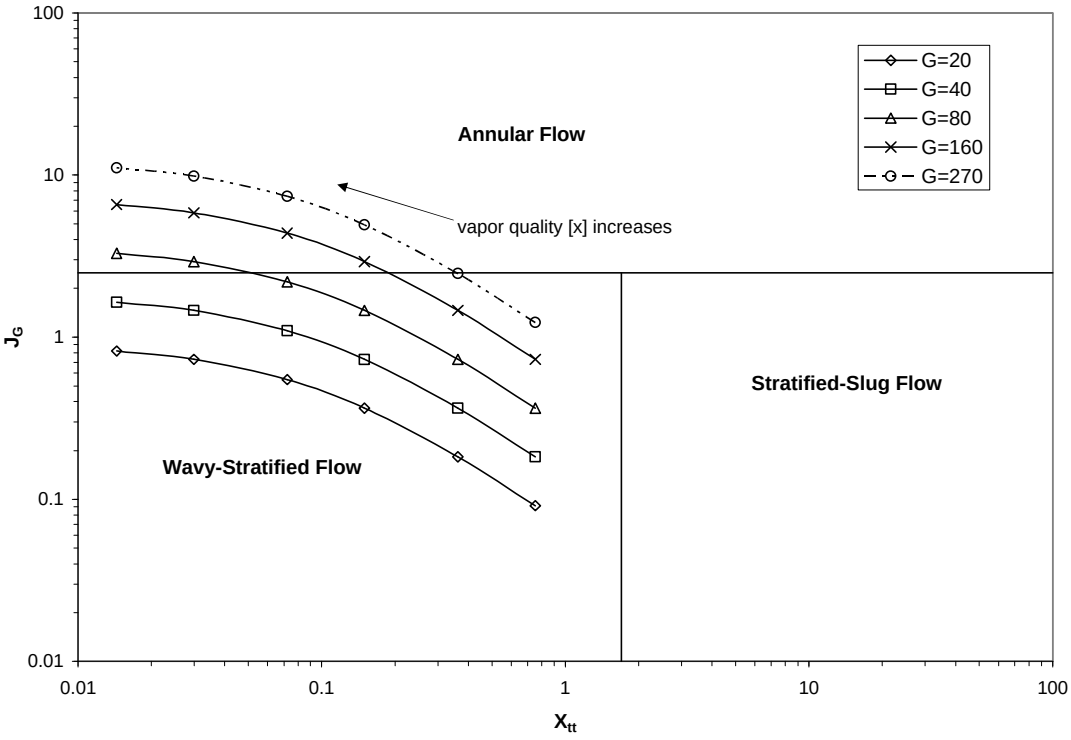

Figure 5.27 Cavallini flow map with lines of constant mass flux for ammonia (Mass Flux, G, in kg/m^2-s)

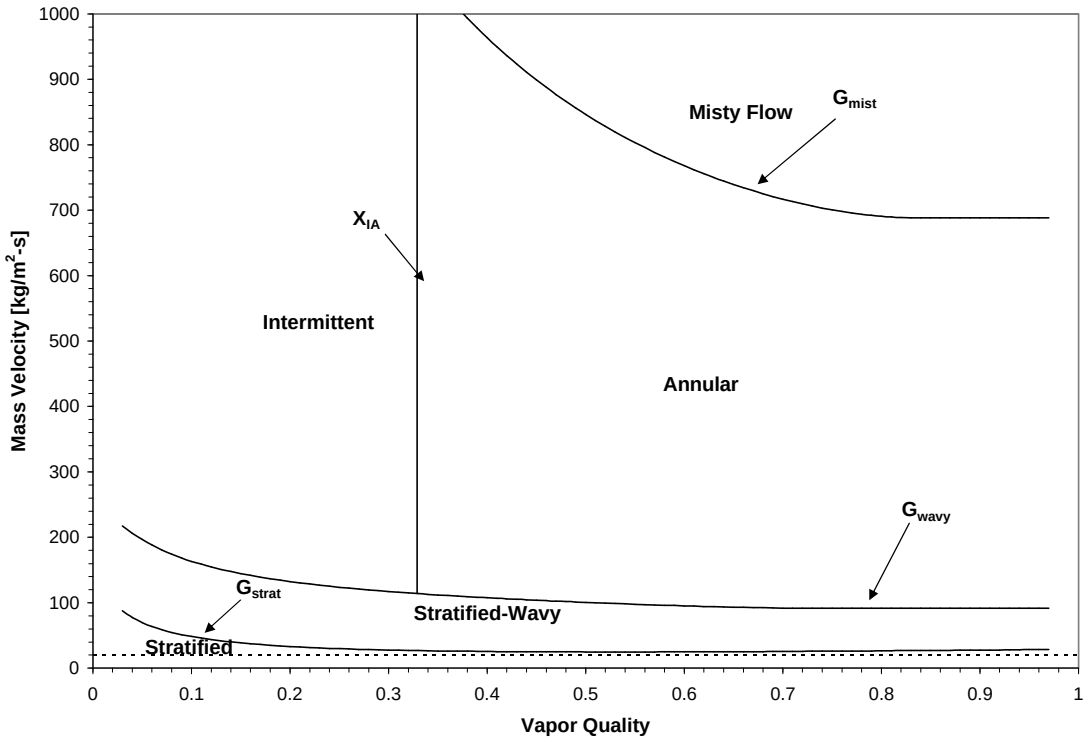

Figure 5.28 Thome flow map for ammonia at a mass flow rate (G) of 20 kg/m^2-s

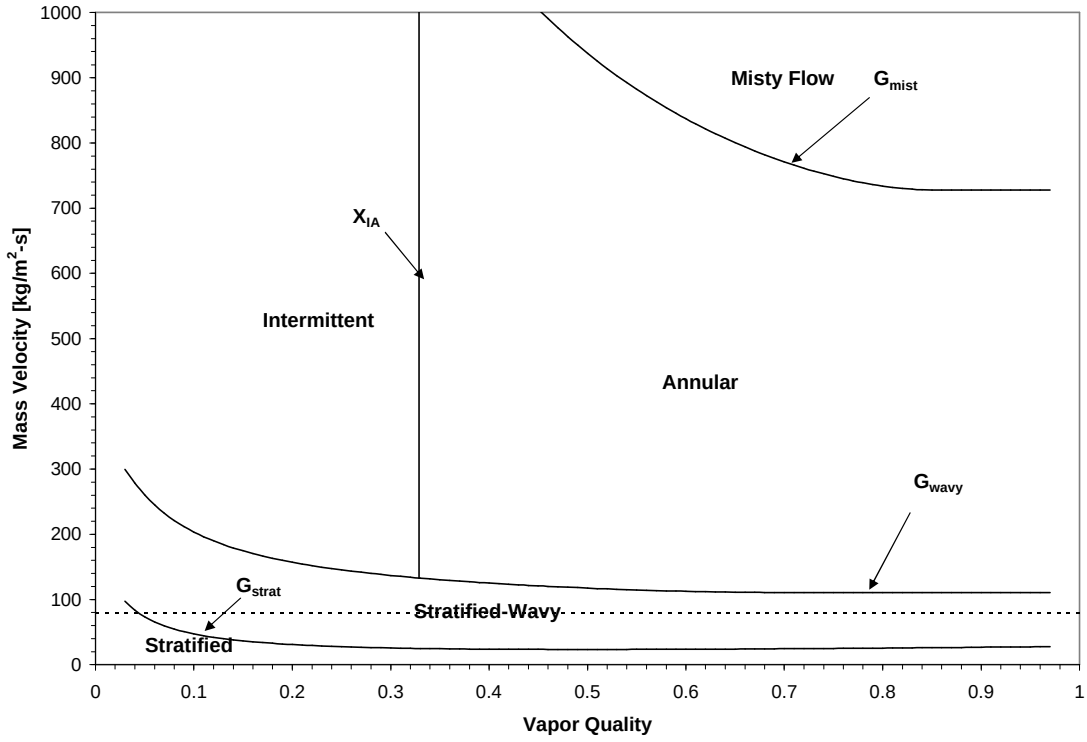

Figure 5.29 Thome flow map for ammonia at a mass flow rate (G) of 80 kg/m^2-s

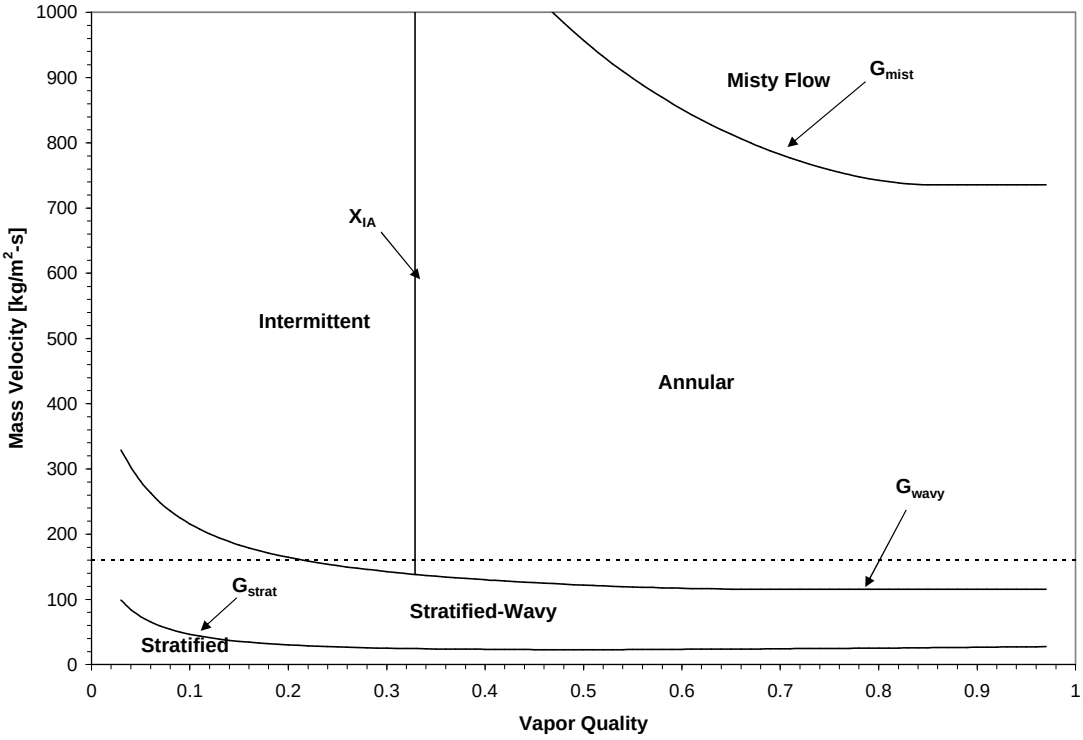

Figure 5.30 Thome flow map for ammonia at a mass flow rate (G) of 16 kg/m^2-s

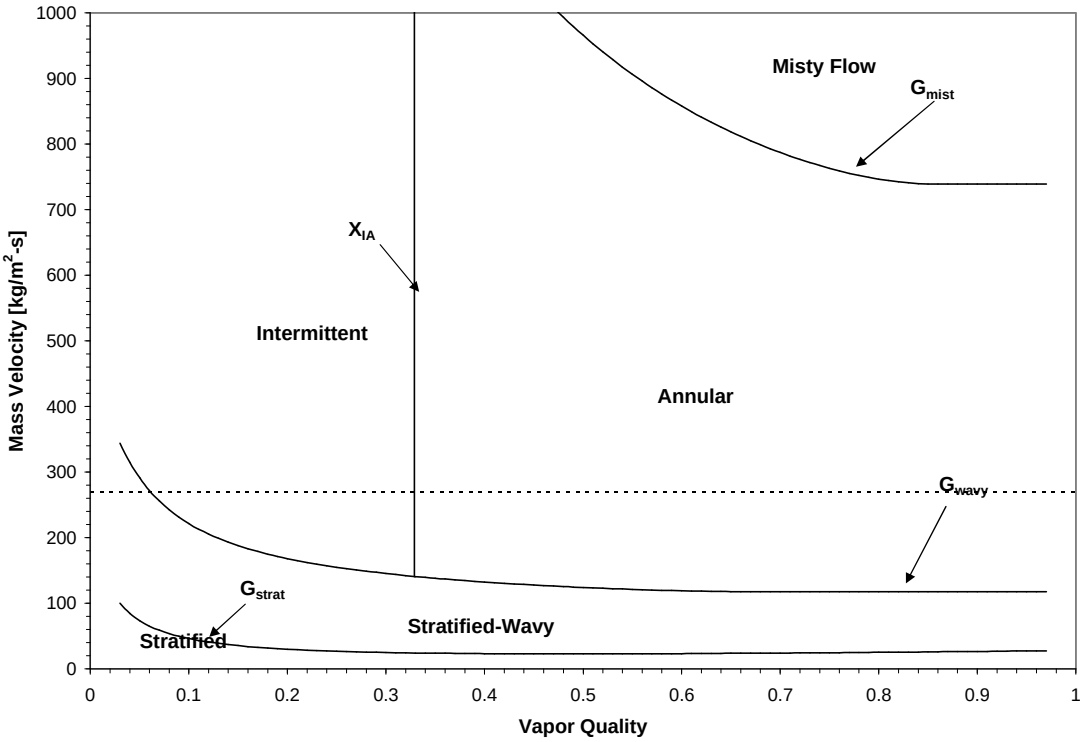

Figure 5.31 Thome flow map for ammonia at a mass flow rate (G) of 270 kg/m^2-s

Chapter 6. Ammonia Pressure Drop during Condensation

This chapter discusses the pressure drop results in the smooth tube and the enhanced tube for pure ammonia in condensation. Throughout the chapter, several comparisons are made with existing two-phase pressure drop correlations, particularly those presented in the literature review section.

6.1 Ammonia Data

Pressure drop data was collected three times on the pure ammonia. However, each set of data has different implications on the pressure drop associated with it. Figure 3.1 shows that the test sections were placed in parallel for easier replication of data points. Because one test section is placed beneath the other, a concern grew that the length of the capillary lines connecting the tube test sections to the pressure transducers may alter the pressure drop measurements. In particular, due to running at saturation temperatures (Tsat=35 ºC) greater than room temperatures (Troom~20 ºC), refrigerant condensate may form in these capillary lines. These 'liquid legs' may have different heights if vapor bubbles form within the connecting lines (i.e. top vs. bottom test section, inlet vs. outlet). To account for the first configuration, the test sections were swapped and rotated after completion of the first set of data points. That is, the smooth test section that was originally located on top was switched with the enhanced tube, originally located on the bottom. This comprises the first two sets of data. The smooth and enhanced test sections were replaced with new test sections for the third data set with the smooth test section on top and the enhanced test on the bottom.

A pressure drop correction factor was needed due to the location of the pressure taps. The pressure taps were located outside of the ball valves controlling the flow into and out of the test sections. The placement of the pressure taps with respect to the ball valves is shown in Figure 3.6. Another important consideration was the pressure drop of the fluid caused by the compressing of the stainless steel ferrules at the ends of the aluminum test section. Due to the relative softness of the aluminum, it was observed visually, that the compression ferrules used to attach the test sections to the facility significantly altered the inner circumference of the tube. Because the pressure drop caused by both of these factors contribute to the overall measured pressure drop, a correction factor was deemed necessary. To determine the correction factor, a dummy test section was developed as shown in Figure 3.7. This 'dummy' test section was modeled after the test sections used so that it would account for both the ball valves and the tube compression effect of the ferrules. The length of this section was determined by looking at where the pressure taps were located in relation to the original test sections. A correction factor was than determined to be applied to the differential pressure data for the smooth tube. Because the 'dummy' test section was comprised of only a smooth tube, the correction factor cannot be applied to the enhanced tube data. A correction factor for each mass flux was obtained. The pressure drop correction factors obtained appear in Equations 6.1-6.3.

$$dP_{corr} = dP_{meas} - \left[-0.15x^2 + 0.707x - 0.033\right] \quad (G=80\ kg/m^2\text{-}s) \qquad (6.1)$$

$$dP_{corr} = dP_{meas} - \left[-3.12x^2 + 5.197x - .385\right] \quad (G=160\ kg/m^2\text{-}s) \qquad (6.2)$$

$$dP_{corr} = dP_{meas} - \left[-8.77x^2 + 12.995x - .717\right] \quad (G=270\ kg/m^2\text{-}s) \qquad (6.3)$$

The pressure drop data appears in two main formats for the four sets of data presented. The first form of data includes the experimental raw data without a correction factor applied to it. Also included in this format is the experimental data with the correction having been applied. The second format of plots includes comparisons made with existing predicting correlations. Three correlation were used, the Friedel (1979), Jung and Radermacher (1989), and Souza (1993). These three correlations are then applied to both the raw experimental data, along with the corrected data. Only data gathered with mass fluxes of 80 kg/m^2-s and greater are presented. The pressure drop for mass fluxes less than 80 kg/m^2-s were negligible and difficult to measure accurately.

6.1.1 First Set of Ammonia Data

The first set of ammonia data was collected with the smooth tube located in the top location and the enhanced tube located on the bottom of the configuration. Figure 6.1 compares the pressure gradient across the smooth and enhanced tube test sections without using the pressure drop correction factor. The trends in this plot are consistent with those seen in the open literature. The pressure gradient increases with quality until a quality of about 70 – 75%. After this point the pressure gradient tends to decrease. The explanation for this can be found in the liquid sublayer. At low qualities the liquid film is thick enough to allow for turbulent wave motions. Interaction between the vapor and the liquid phases at the interface between the turbulent liquid waves and the vapor is responsible for the majority of the pressure drop. As the flow increases to higher qualities, the liquid film thickness, and therefore the liquid wave height decreases, lowering the "roughness" of the liquid surface. When the flow is at approximately 70 -75% quality, the liquid film is too thin to form significant wave structures. The pressure gradient is also observed to be a function of mass flux. As mass flux increases, so too do the vapor velocities of the flow. An increase in vapor velocity will increase the turbulent nature of the vapor and liquid phases, thus causing higher pressure gradients.

It is also observed in Figure 6.1 that the pressure gradient of the enhanced tube is greater than the smooth tube pressure gradient. This increased pressure gradient of the enhanced tube is also consistent with results found in the open literature. The microfins on the enhanced tube increase the roughness of the tube in addition to the surface roughness of the liquid phase.

Figure 6.2 shows the corrected pressure gradient of the smooth tube test section. Comparing Figure 6.2 with Figure 6.1 illustrates the significance of the correction factor. On average, the correction factor reduces the pressure gradient by approximately 30%. Figures 6.3 and 6.4 compare the uncorrected and corrected pressure gradient with three pressure gradient models. The models used include the Friedel, Jung and Radermacher, and Souza. Figure 6.3 shows the measured, uncorrected data. From this plot, all three correlations perform very well, with the Souza correlation being the most accurate. Figure 6.4 displays the corrected pressure gradient data. Figure 6.4 shows that the Friedel correlation performs the best, while the other two models tend to overpredict the data. This could be caused by an error in developing the correction model, where perhaps the correction model accounts for too much pressure gradient thus excessively lowering the corrected data. Conversely, the open literature generally regards the Friedel correlation to perform the best because it is based on a more extensive set of test data than the other two models.

Figure 6.5 is a graph of the uncorrected pressure gradient data in terms of a penalty factor. A penalty factor is a commonly used method of directly comparing pressure gradients among two or more different flow passageways. In this case, the experimental results from the enhanced tube are compared with those from the smooth tube. The penalty factor used in this paper is defined as the pressure gradient of the enhanced tube divided by the predicted pressure gradient of the smooth tube.

$$PF = \frac{dP/dz_{enh}}{dP/dz_{smooth,G}} \tag{6.4}$$

Where $dP/dz_{smooth,G}$ is the pressure gradient for the smooth tube at the same mass flux (G) and flow properties in the enhanced tube. This predicted pressure gradient, $dP/dz_{smooth,G}$, is calculated using an adjustment of a pressure gradient correlation. The most accurate of the three correlations (Friedel, Jung & Radermacher, or Souza) in terms of predicting the smooth tube pressure gradient is used. The correlation is then adjusted by a constant so that the penalty factor for a smooth tube is approximately unity. The methodology behind this technique is very similar to the one used in determining the enhancement factor for heat transfer comparisons (Section 4.2, 5.1.1)

Figure 6.5 shows that for the uncorrected data, the penalty factor is on average 1.4 for both flow rates shown (G=160, 270 kg/m^2-K). The penalty factors associated with a mass flux (G) of 80 kg/m^2-K are not presented because of a difficulty in attaining one adjustment that would allow a penalty factor of one for all smooth tube pressure gradients. Another interesting trend appearing on this plot is that the penalty factor appears to be independent of mass flux. The penalty factor is also relatively insensitive to quality, although some influence of increasing penalty factor with quality is observed at elevated qualities.

6.1.2 Second Set of Ammonia Data

The second set of ammonia data was collected after switching the test section positions in the flow loop. The enhanced tube is in the top position, while the smooth tube has been placed underneath. This second set of pressure gradient data shows a considerable amount of scatter. This can be observed in Figures 6.6 and 6.7 (without and with pressure drop correction, respectively). The main reason for the apparent scatter is that some of the data points, particularly those at the high mass fluxes, were taken at saturation temperatures between 43-51 ºC. This increase in temperature compared to the majority of the points being taken at a temperature of 35 ºC causes a decrease in pressure gradient. An increase in saturation temperature causes an increase in vapor density. An increased vapor density requires a lower vapor velocity to achieve the same mass flux. A lower vapor velocity will cause lower turbulent interaction between the vapor and liquid phases, thus reducing the dissipation of kinetic energy of the flow.

Figures 6.8 and 6.9 display how well the two different sets of smooth tube pressure gradients compare with the pressure gradient prediction models. Figure 6.8 compares the uncorrected experimental pressure gradient data, while Figure 6.9 compares the corrected pressure gradient data. In Figure 6.8, the model developed by Jung and Radermacher appears to perform the best, while Friedel consistently underpredicts the experimental data. Applying the pressure drop correction factor, Figure 6.9 shows that the Freidel correlation performs the best, while both the

Souza and the Jung and Radermacher correlations tend to overpredict the pressure gradient relative to the experimental data.

The penalty factors for this second set of pressure gradient data emerge in Figure 6.10. For qualities lower than ~30%, the penalty factors are lower than one. This trend disagrees with what is shown in Figure 6.6, where even at these low qualities the enhanced tube has a higher pressure gradient than the smooth tube. The most likely cause to this trend appearing in Figure 6.10 is that the correction applied to the correlations does not accurately fit these lower quality data points. However, the data points taken at qualities greater than 30%, show the penalty factors to be greater than one. Figure 6.10 shows more of a dependence on mass flux (G), than observed from the first set of data (Figure 6.5). The data taken at a mass flux of 270 kg/m^2-s has an overall higher set of penalty factors than the set of data with a mass flux of 160 kg/m^2-s.

6.1.3 Third Set of Ammonia Data

After the second of data, the original two test sections were replaced with two new ones (smooth and enhanced tubes). Like the first set, the smooth tube was placed on top and the enhanced tube was positioned on the bottom. Figure 6.11 exhibits the measured (uncorrected) pressure gradient data for this third set of data. Figure 6.12 displays the corrected experimental data. Figures 6.11 and 6.12 appear very similar to results observed with the first set of ammonia data (Figures 6.1, 6.2).

The experimental versus predicted plots for this set of data appear in Figure 6.13 and 6.14. Figure 6.13 shows that all three correlations (Friedel, Jung and Radermacher, and Souza) predict the uncorrected data fairly accurately, with the Jung and Radermacher model being the most accurate. The corrected experimental data is plotted versus the predicted data in Figure 6.14. Similar to the previous two data sets, the Friedel correlation performs the best, while the Jung and Radermacher and Souza tend to consistently overpredict the data.

The penalty factors for this third set of data appear in Figure 6.15. These factors show a trend somewhere in between the ones observed in the first two sets. It appears that the data points seem to be affected by both mass flux and quality, but not to the extent observed in the second data set (Figure 6.10). In addition to this, the average of the data sets is approximately 1.4. This coincides with the first data set (Figure 6.5). Overall, Figure 6.15 shows that the enhanced tube has a higher pressure gradient than the smooth tube.

6.1.4 Direct Mass Flux (G) Comparison

This subsection serves as a direct comparison of the three sets of data at the different mass fluxes. The pressure gradients that appear are from the uncorrected data. The first set of figures (Figures 6.16-6.18) compares the data sets taken on the smooth tube. All three smooth tube plots show that the three sets of data are very consistent with each other. The second set of figures (Figures 6.19-6.21) examines the data sets taken on the enhanced tube. In all three plots depicting the enhanced tube data, the pressure gradients appear to agree reasonably well with one another. Overall, all three sets of data taken for both tubes demonstrate the repeatability of the pressure gradient data regardless of test section location, or individual test sections.

6.2 Figures

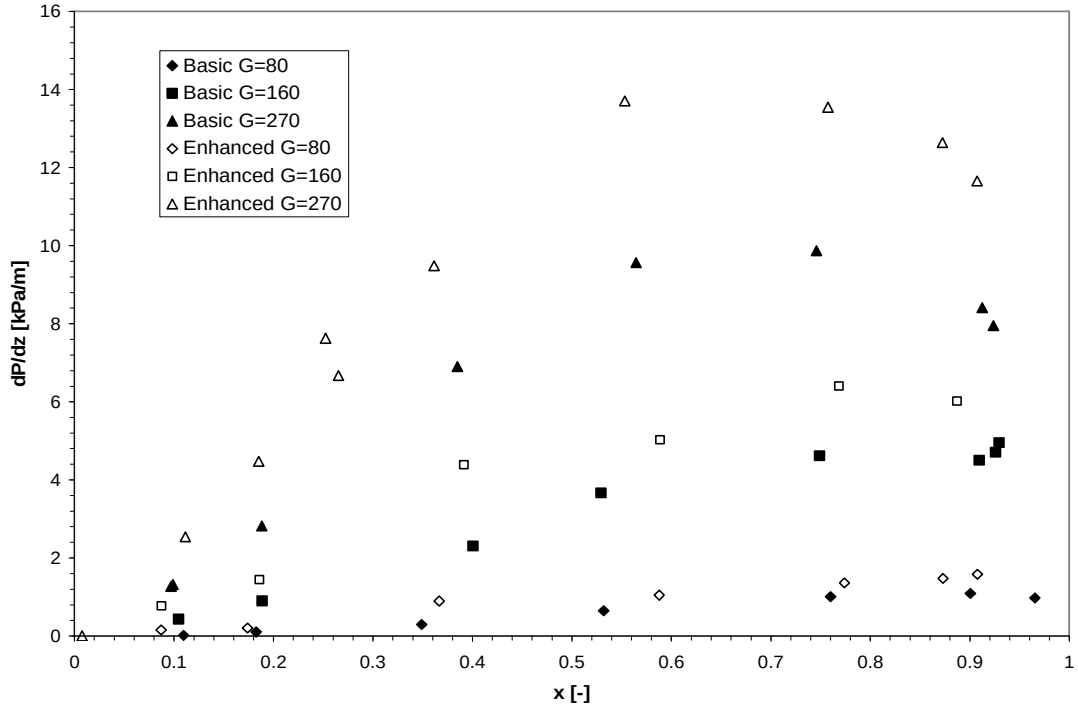

Figure 6.1 First set of uncorrected experimental pressure gradient data for both smooth and enhanced tubes (Mass Flux, G, in kg/m^2-s)

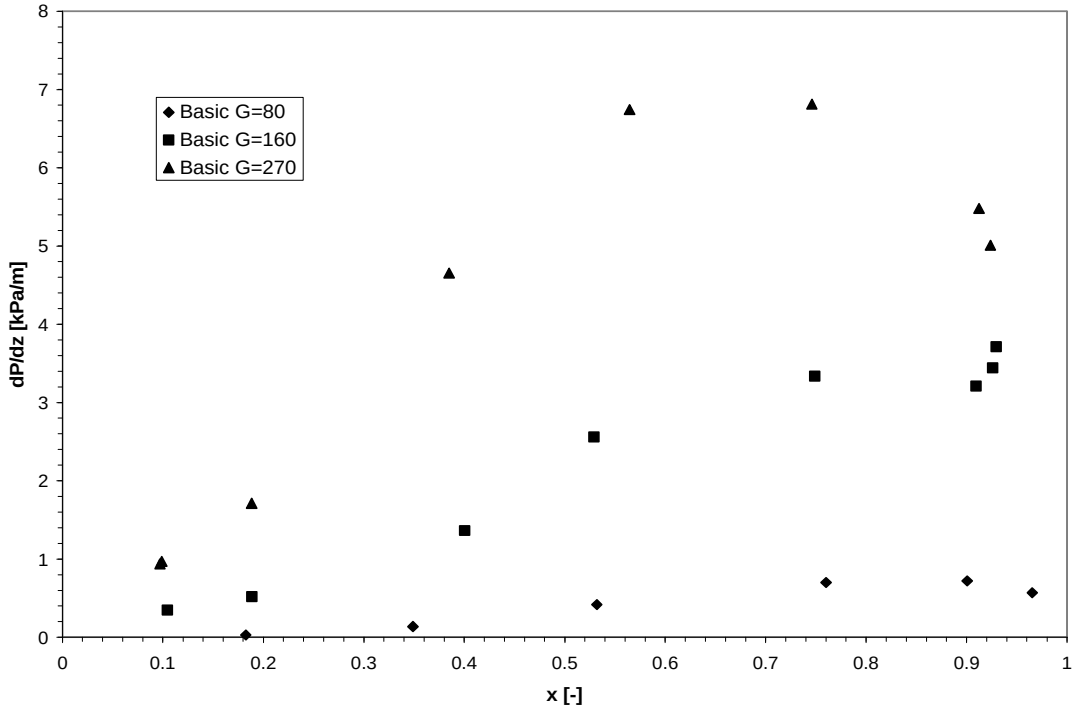

Figure 6.2 First set of corrected experimental pressure gradient data for both smooth and enhanced tubes (Mass Flux, G, in kg/m^2-s)

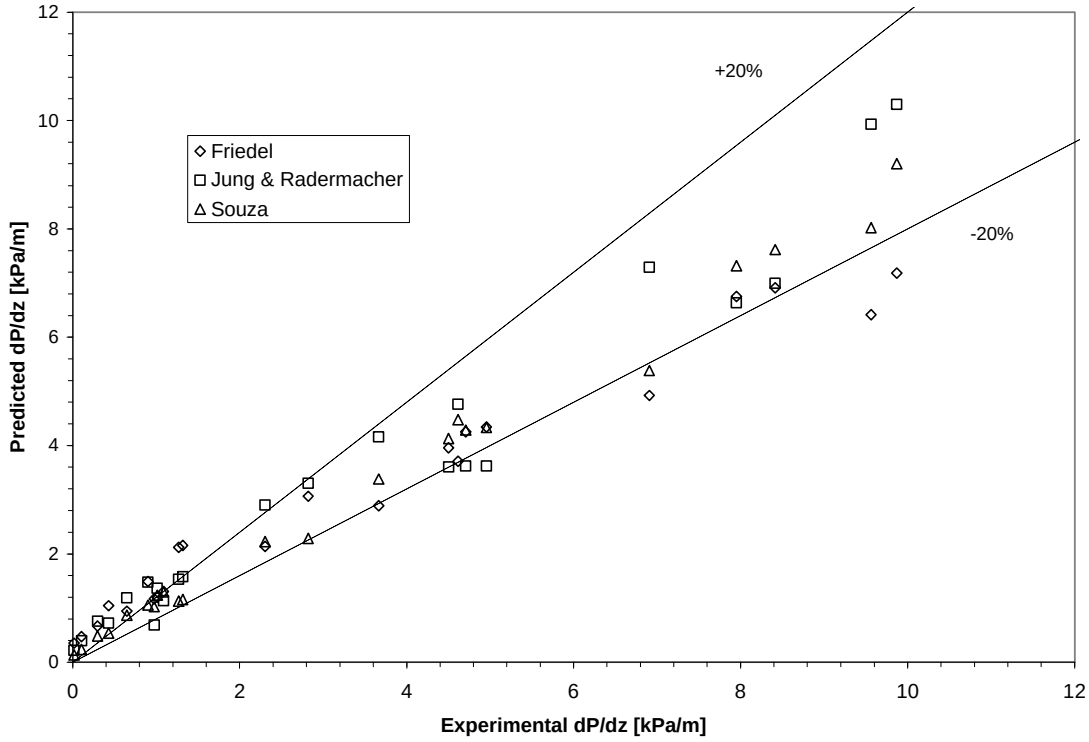

Figure 6.3 First set of ammonia data, uncorrected smooth tube correlation comparison

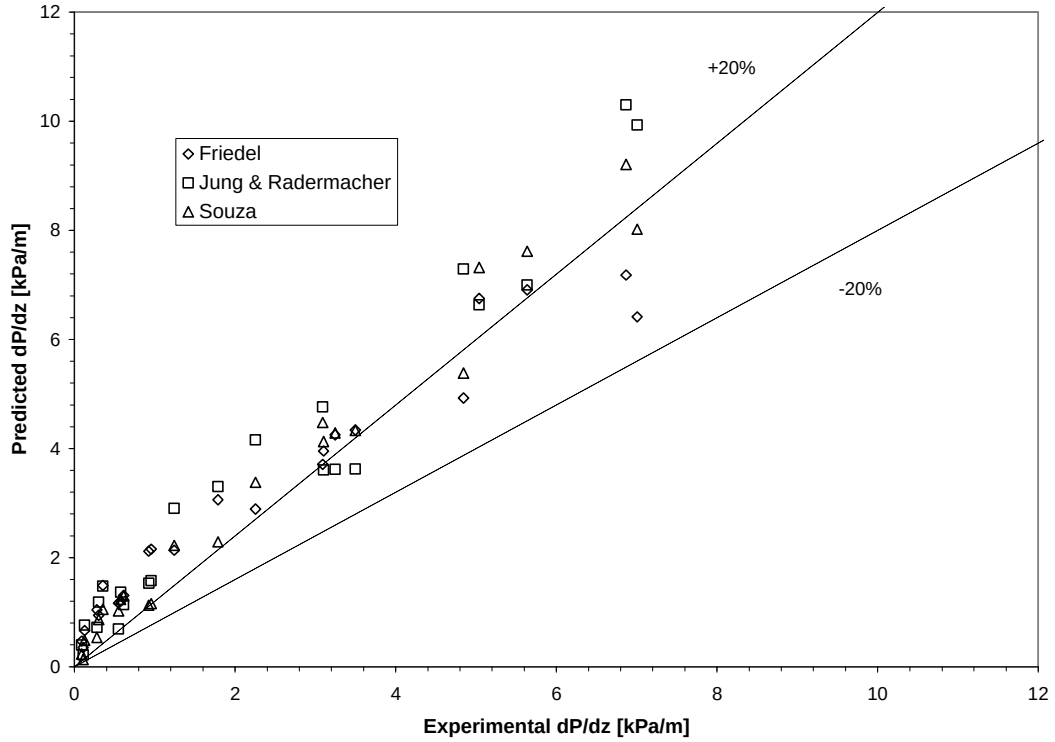

Figure 6.4 First set of ammonia data, corrected smooth tube correlation comparison

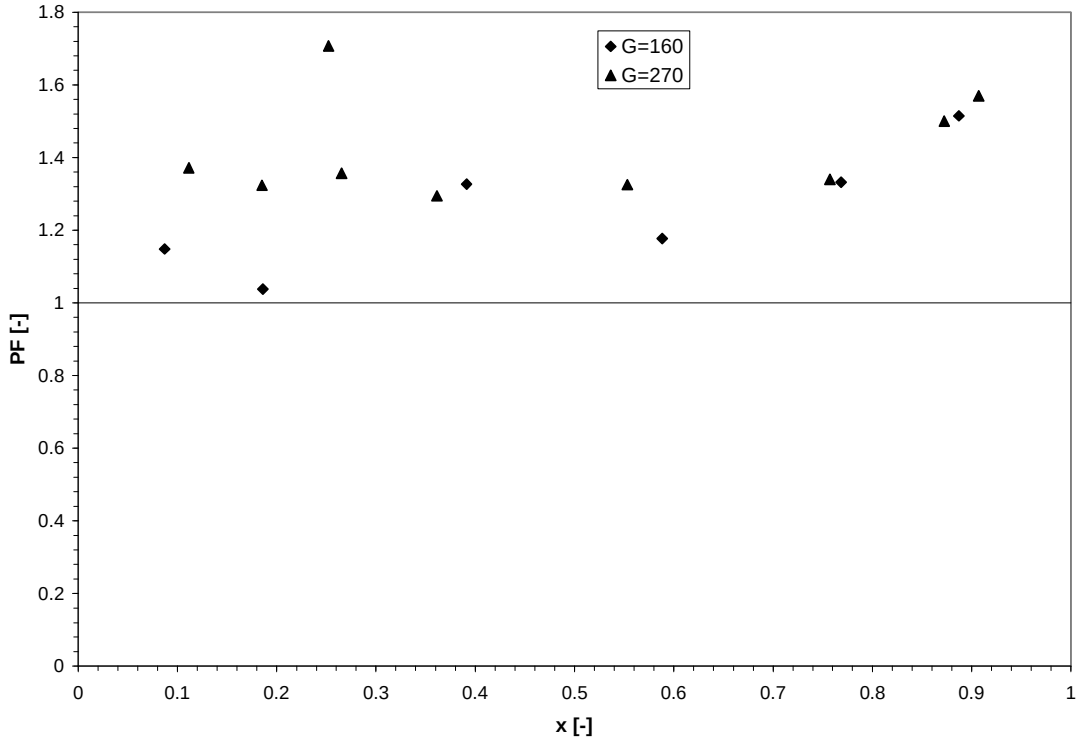

Figure 6.5 Penalty factor for first set of ammonia data (Mass Flux, G, in kg/m^2-s)

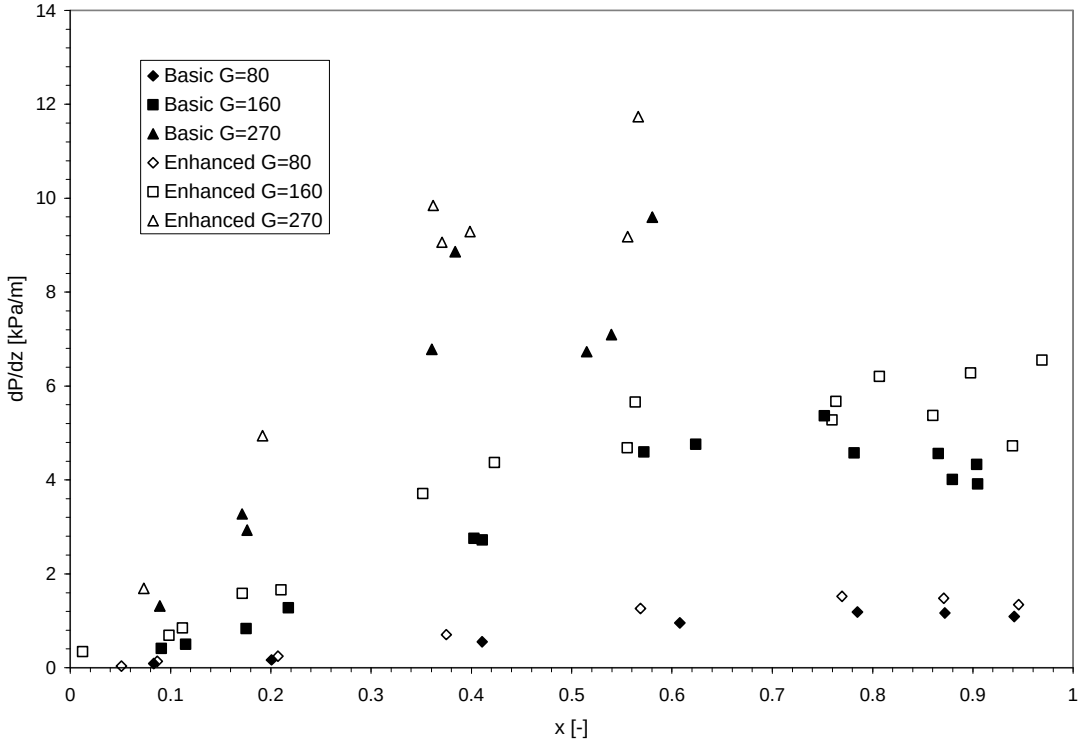

Figure 6.6 Second set of uncorrected experimental pressure gradient data for both smooth and enhanced tubes (Mass Flux, G, in kg/m^2-s)

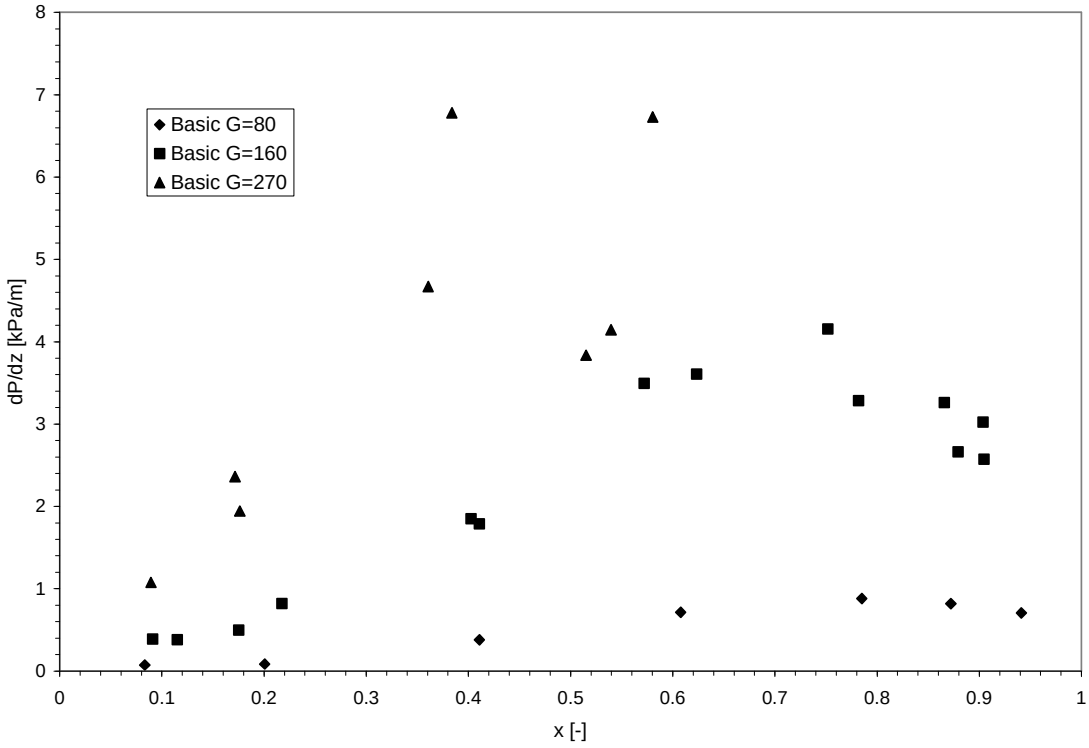

Figure 6.7 Second set of corrected experimental pressure gradient data for both smooth and enhanced tubes (Mass Flux, G, in kg/m^2-s)

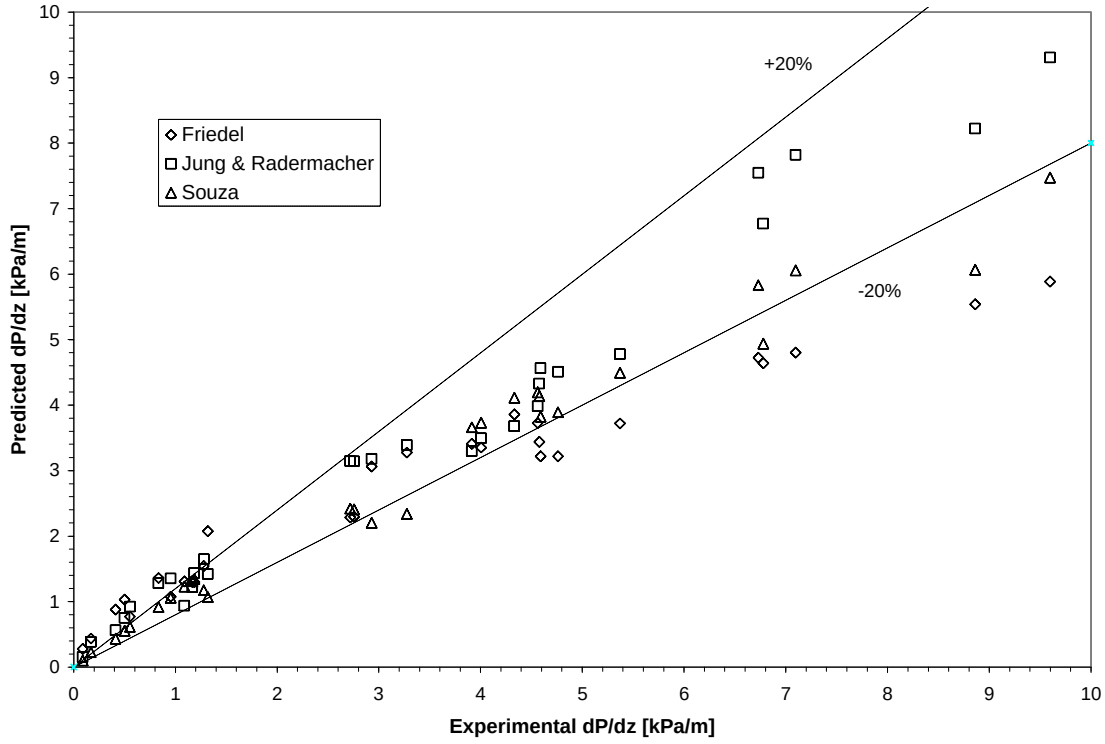

Figure 6.8 Second set of ammonia data, uncorrected smooth tube correlation comparison

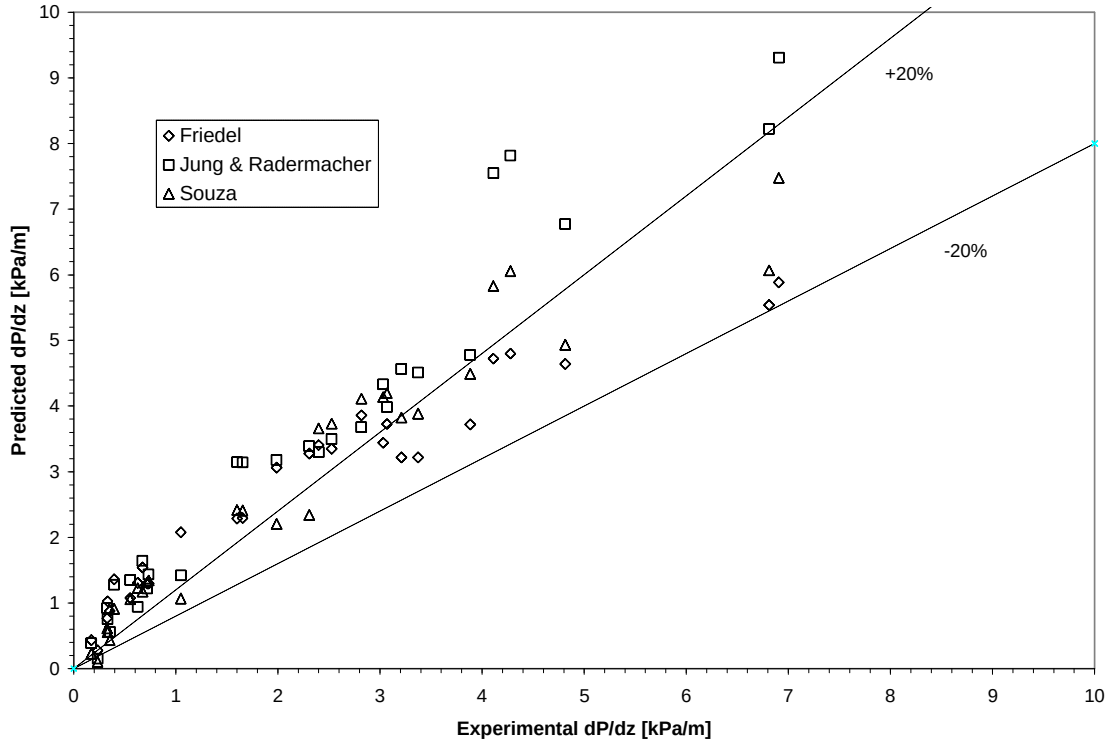

Figure 6.9 Second set of ammonia data, corrected smooth tube correlation comparison

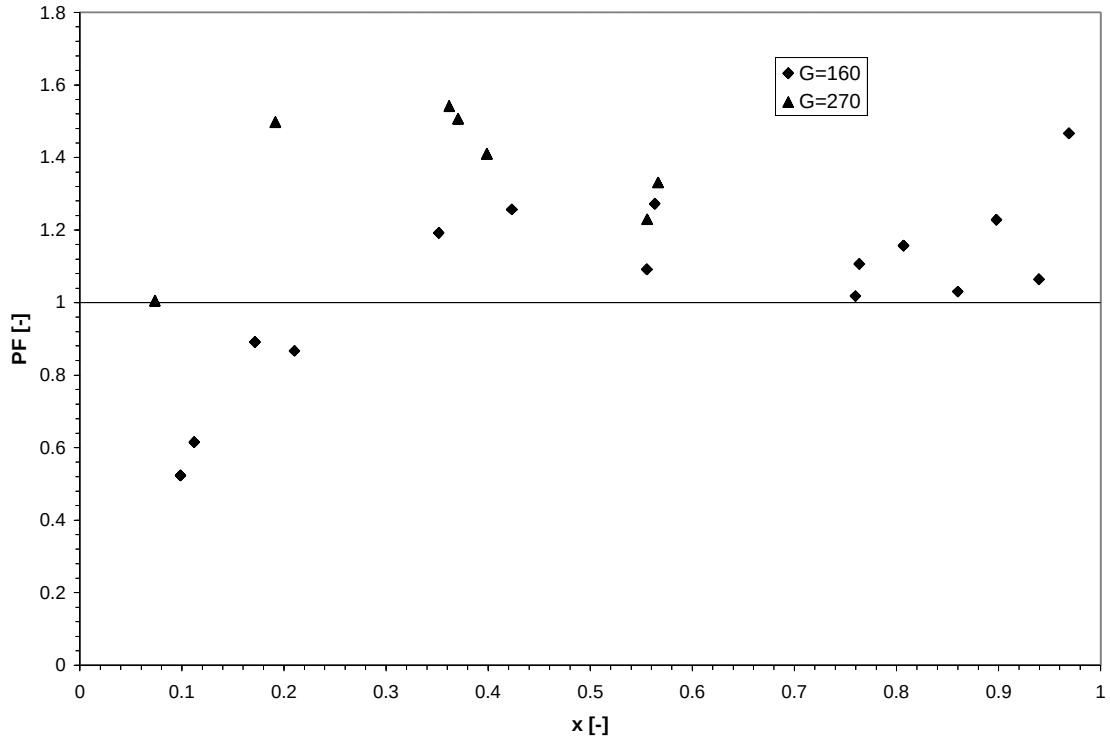

Figure 6.10 Penalty factor for second set of ammonia data (Mass Flux, G, in kg/m^2-s)

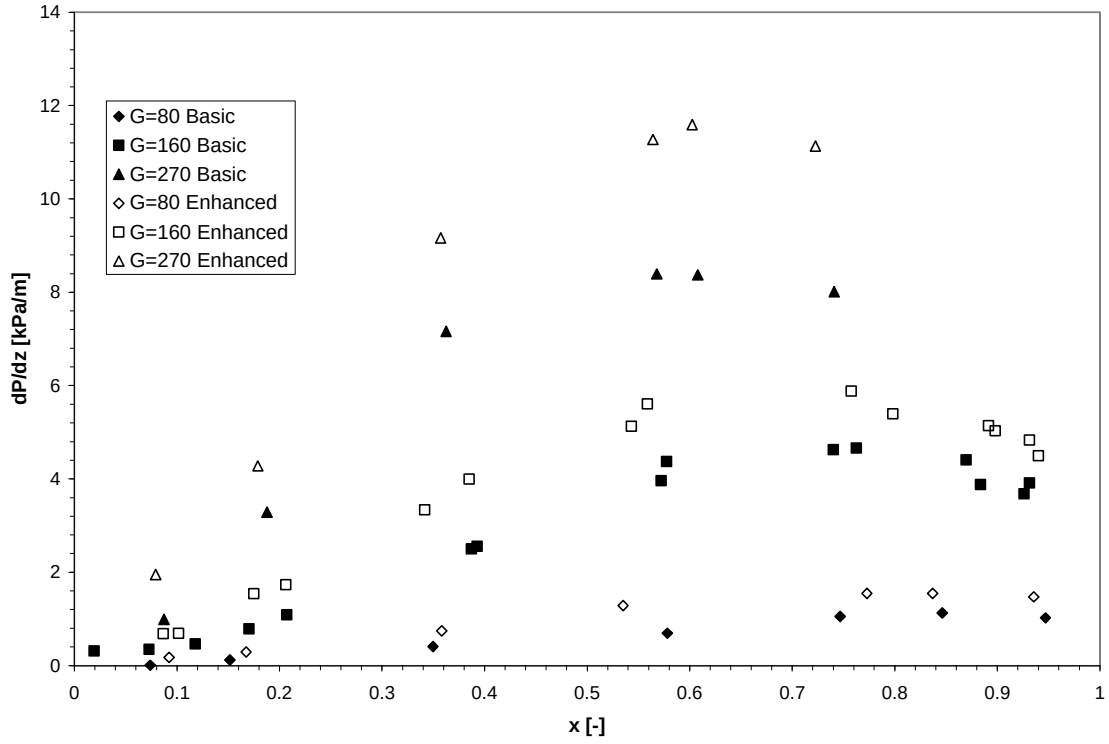

Figure 6.11 Third set of uncorrected experimental pressure gradient data for both smooth and enhanced tubes (Mass Flux, G, in kg/m^2-s)

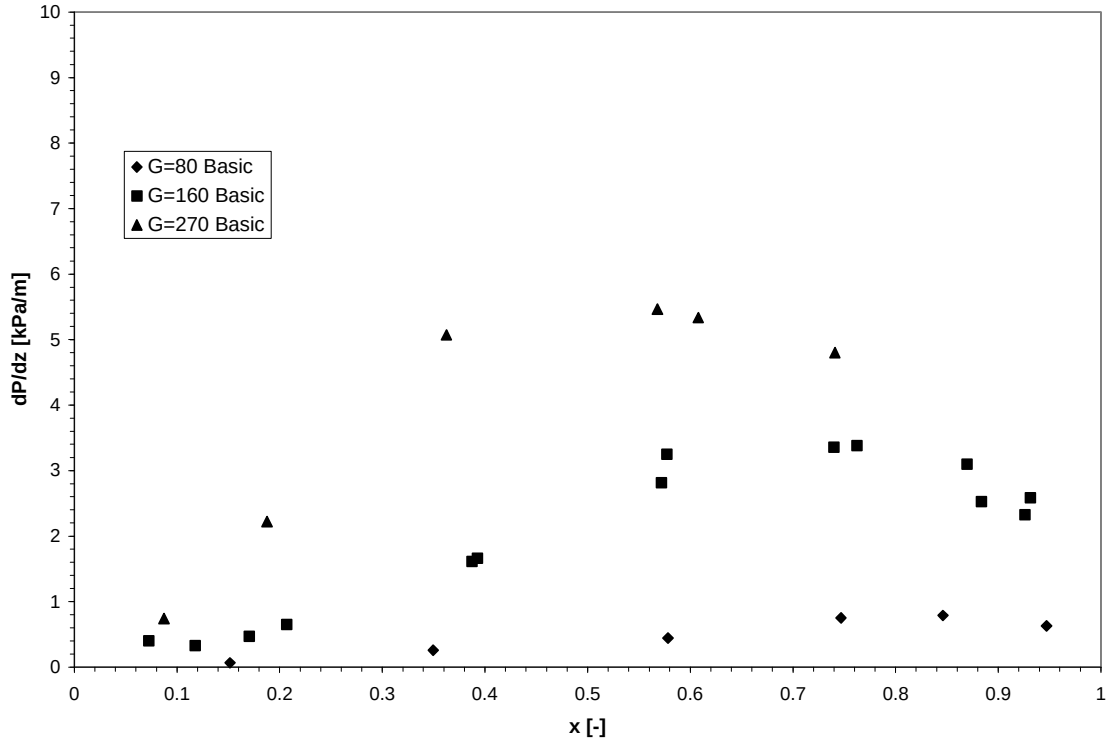

Figure 6.12 Third set of corrected experimental pressure gradient data for both smooth and enhanced tubes (Mass Flux, G, in kg/m^2-s)

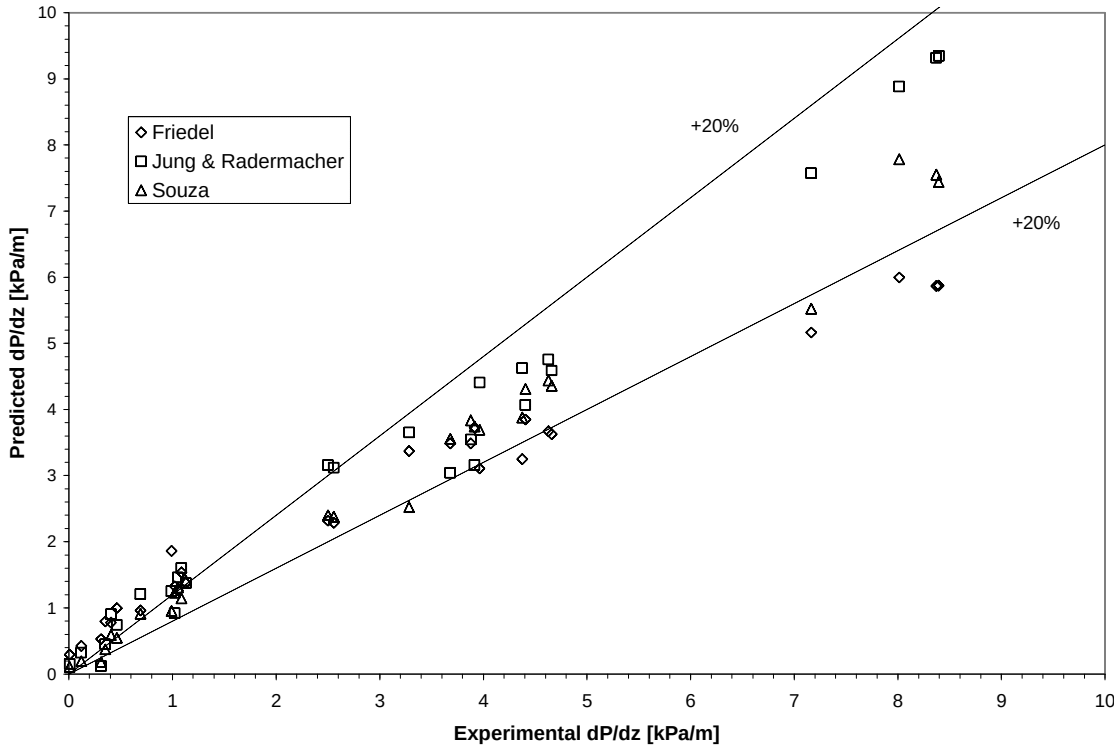

Figure 6.13 Third set of ammonia data, uncorrected smooth tube correlation comparison

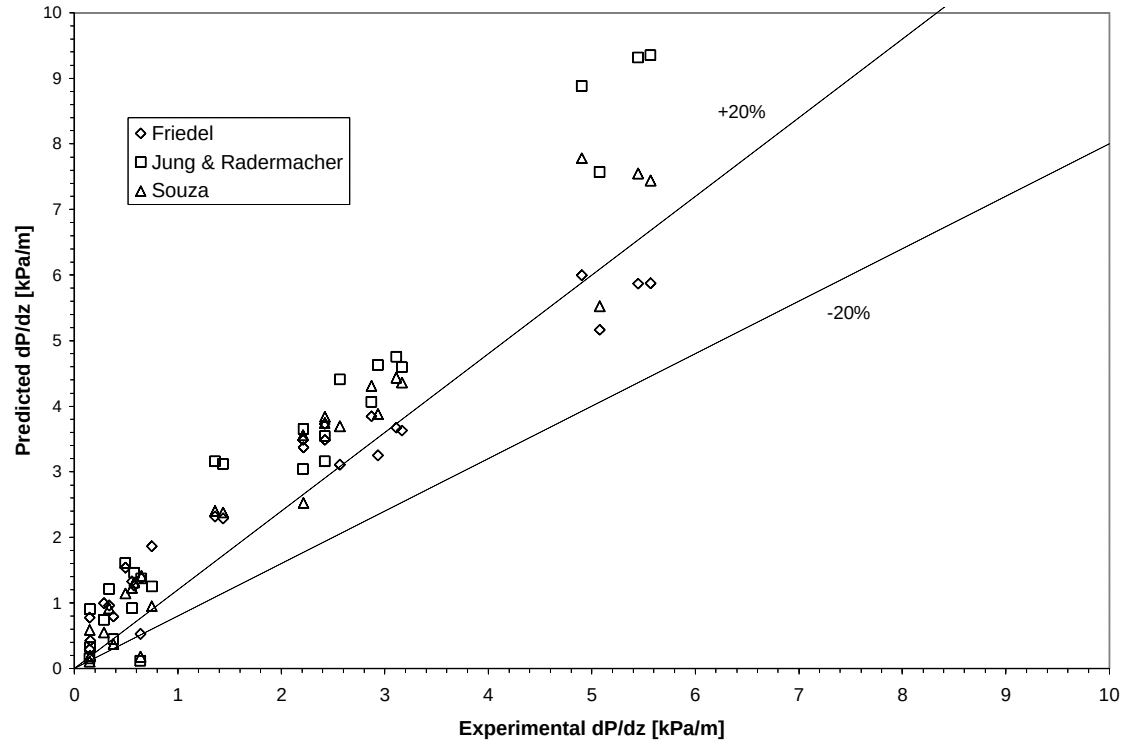

Figure 6.14 Third set of ammonia data, corrected smooth tube correlation comparison

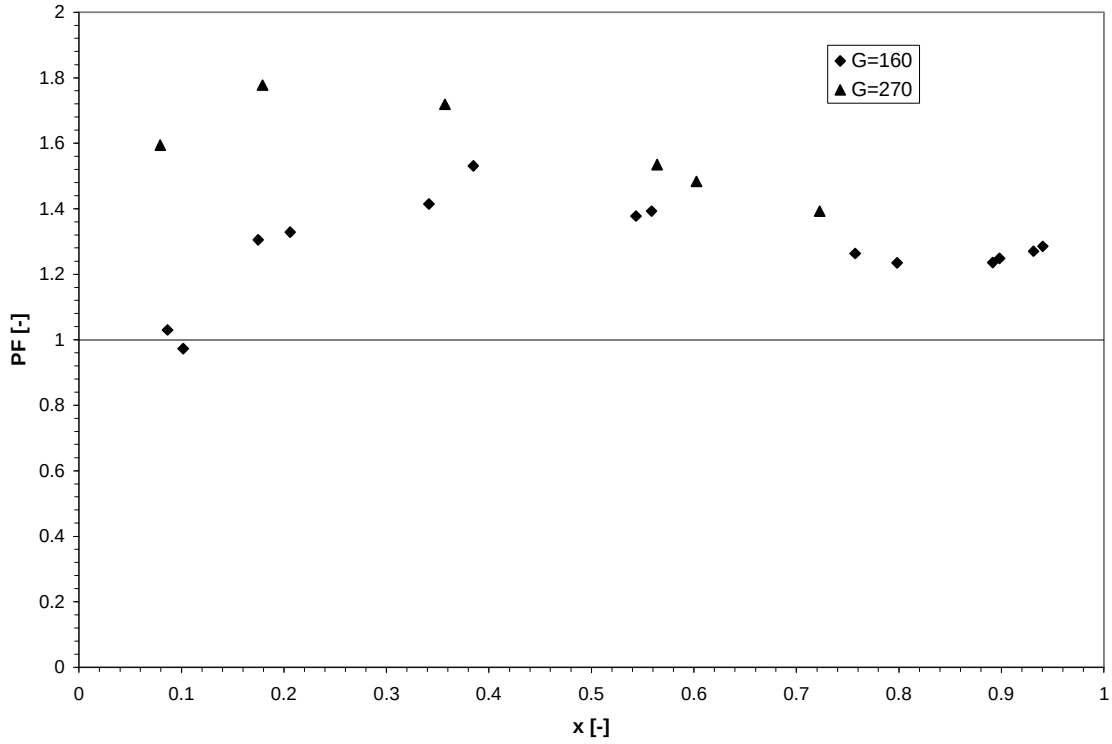

Figure 6.15 Penalty factor for third set of ammonia data (Mass Flux, G, in kg/m^2-s)

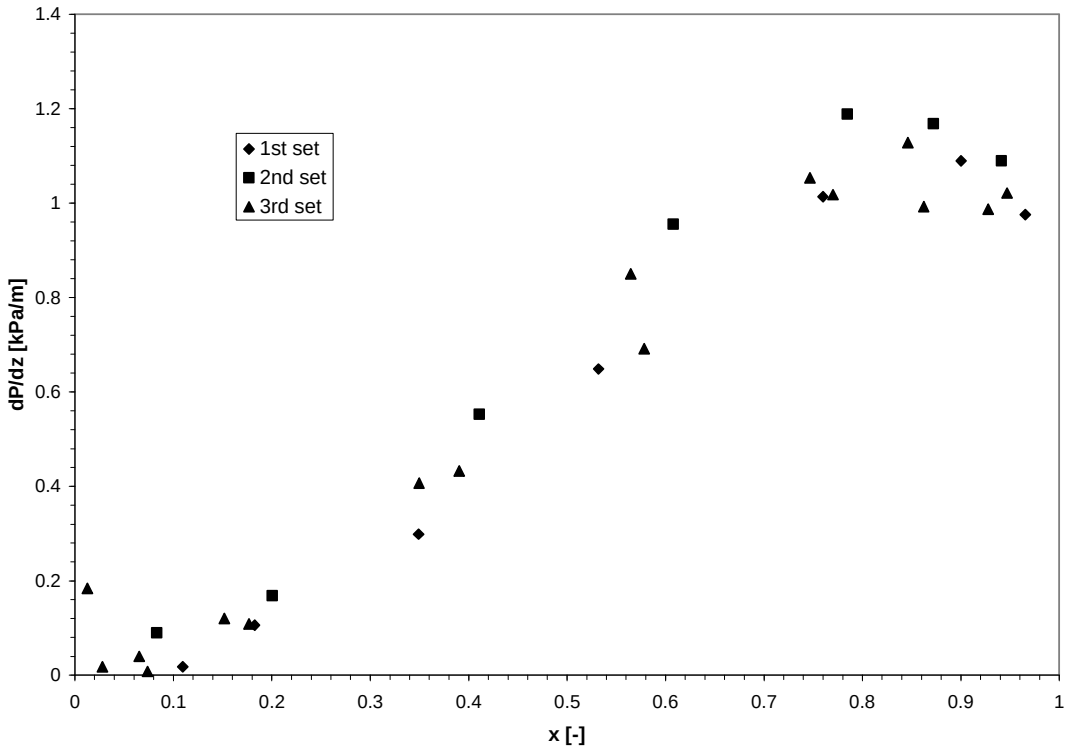

Figure 6.16 Smooth tube, comparison of pressure gradient sets, G=80 kg/m^2-s

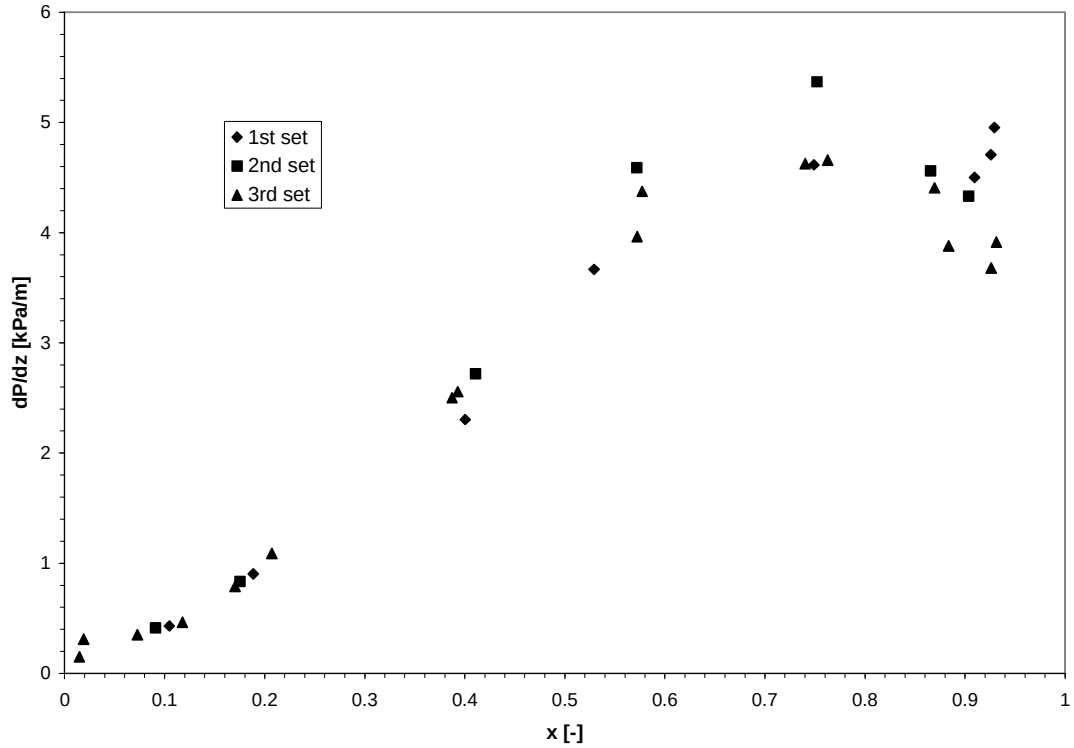

Figure 6.17 Smooth tube, comparison of pressure gradient sets, G=160 kg/m^2-s

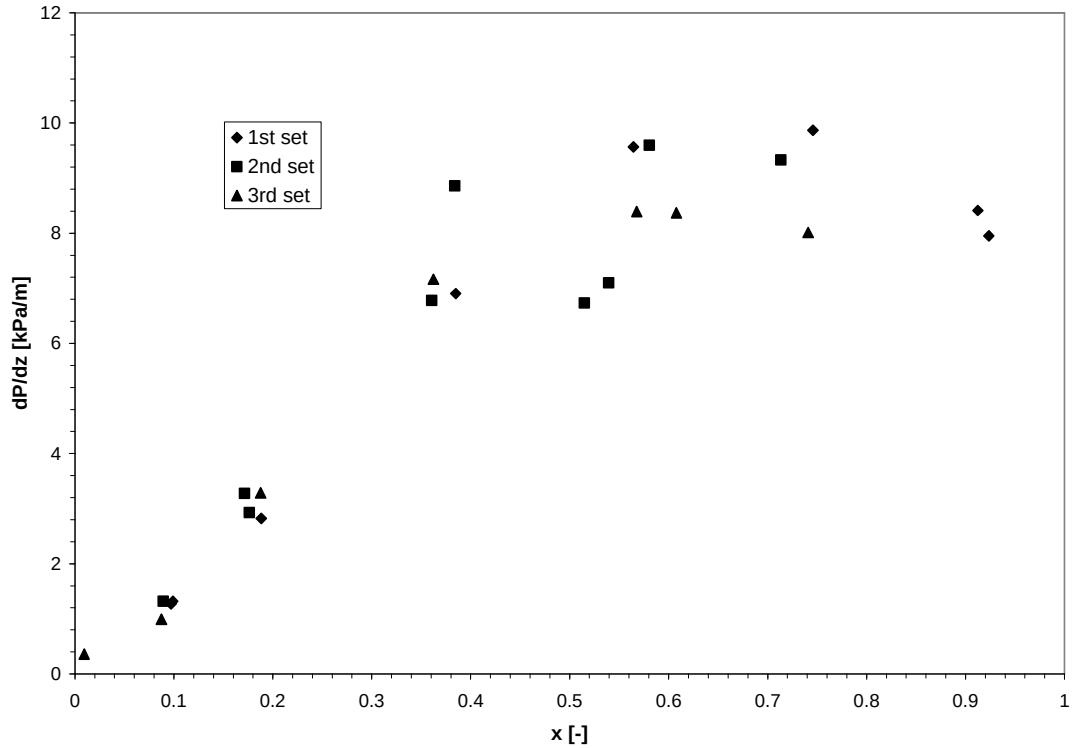

Figure 6.18 Smooth tube, comparison of pressure gradient sets, G=270 kg/m^2-s

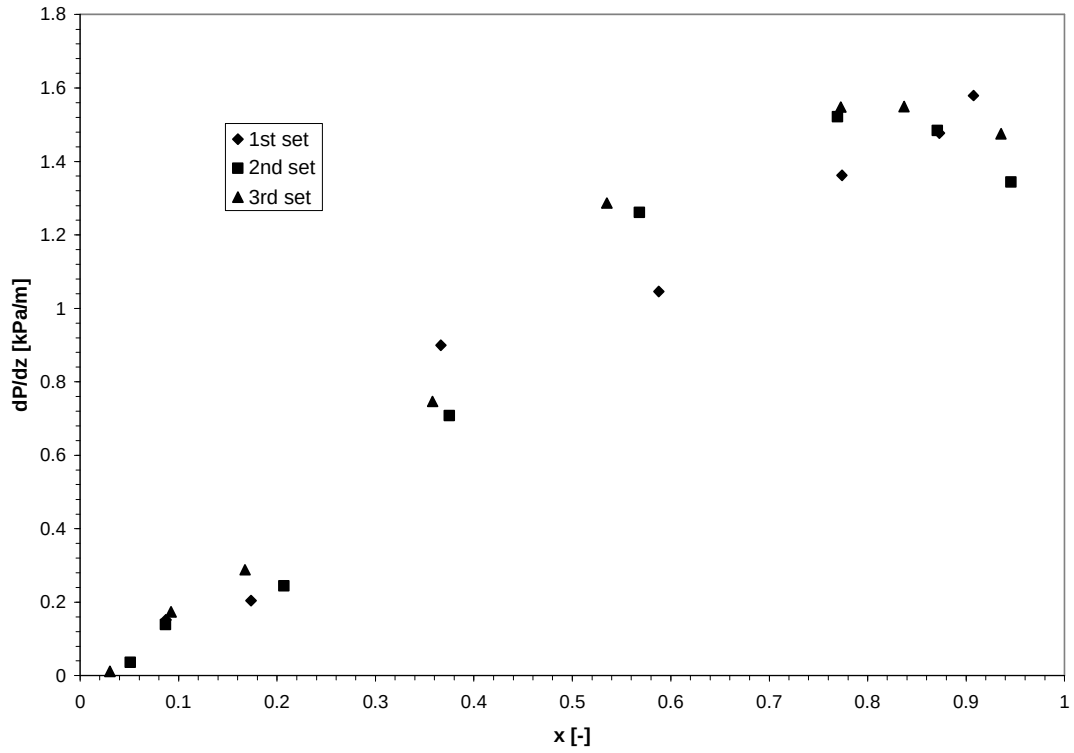

Figure 6.19 Enhanced tube, comparison of pressure gradient sets, G=80 kg/m^2-s

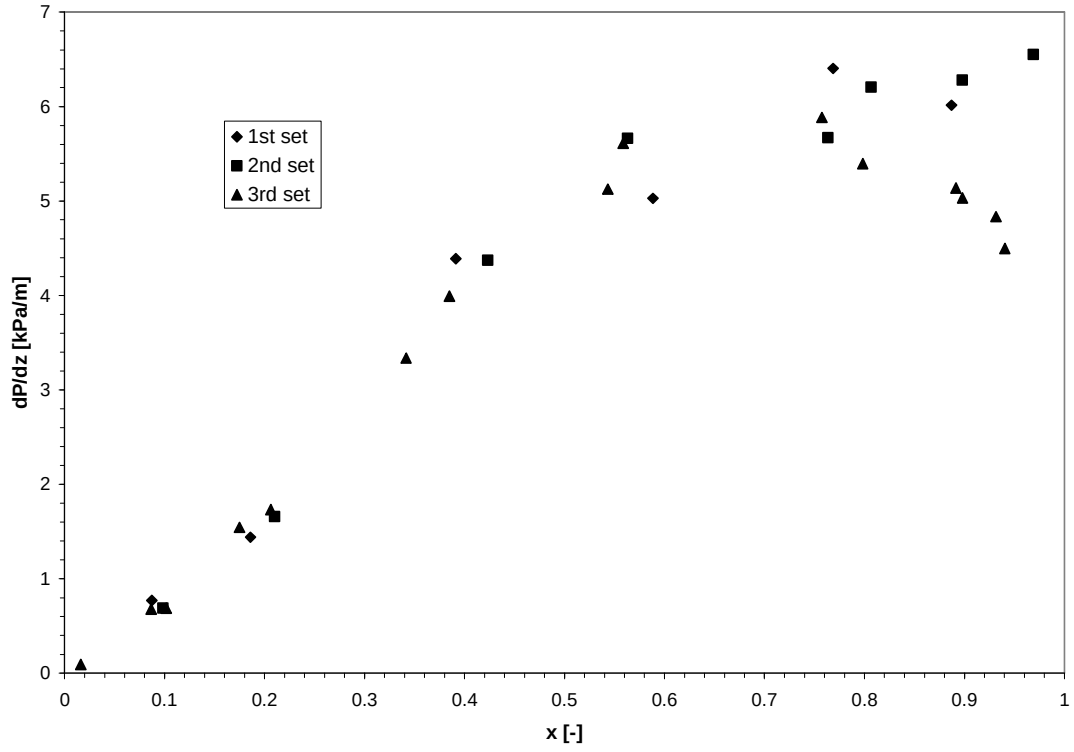

Figure 6.20 Enhanced tube, comparison of pressure gradient sets, G=160 kg/m^2-s

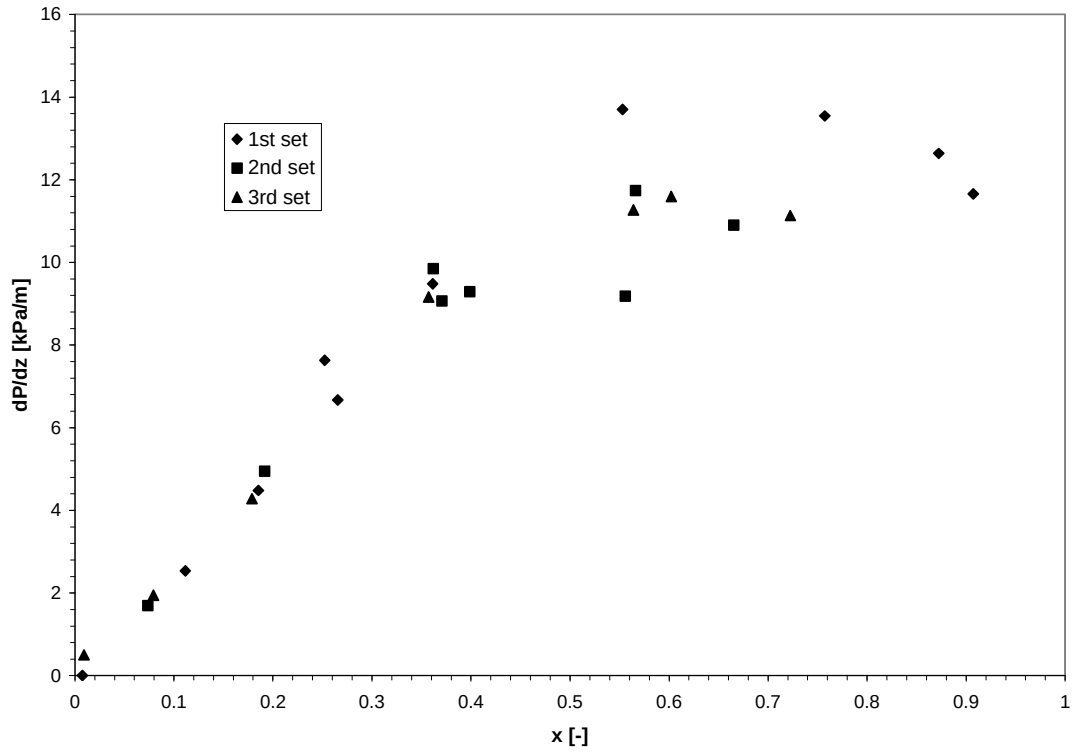

Figure 6.21 Enhanced tube, comparison of pressure gradient sets, G=270 kg/m^2-s

Chapter 7. Conclusion

Pressure drop and heat transfer experiments were conducted to investigate the effects of ammonia in an in-tube condensation system. Effects of tube geometry were also explored. The results of this project were presented and explained in the previous chapters.

Heat transfer results show that the smooth tube performs better than the enhanced tube in terms of heat transfer coefficients. In addition to this, the enhancement factor results show that the enhanced tube performs worse than the smooth tube in terms of heat flux transferred. Heat transfer correlations tend to consistently over predict the smooth tube data. The multiple flow regime correlations appear to more consistent than the single flow (annular) flow regimes in terms of predicting the data.

The pressure drop results show increased pressure gradients for condensation conditions in the enhanced test section. This increased pressure gradients, coupled with poorer heat transfer performance suggest that overall the enhanced tube performs worse than the smooth tube. Pressure drop correlations gave good prediction for the basic test section. For the uncorrected data, the correlations were both consistent and accurate. In terms of the corrected pressure gradient data, the Friedel correlation performed the best, while the other two used appeared to overpredict the data.

Bibliography

Ackers, W.W., H.A. Deans, and O.K. Crosser, "Condensation heat transfer within horizontal tubes," *Chemical Engineering Progress Symposium Series*, 55, 171-176, 1959.

Baker, O., "Simultaneous Flow of Oil and Gas", *Oil and Gas Journal*, Vol. 53, pp. 185-195, 1954.

Barnhart, J., "An Experimental Investigation of Flow Patterns and Liquid Entrainment in a Horizontal-Tube Evaporator," ACRC TR-28, Air Conditioning and Refrigeration Center, University of Illinois Urbana-Champaign IL, 1992.

Bivens D.B., and A. Yokozeki, "Heat Transfer Coefficients and Transport Properties for Alternative Refrigerants," *International Refrigerant Conference Proceedings*, Purdue University, July 1994.

Carpenter, E.F. and A.P. Colburn, "The effect of vapor velocity on condensation inside tubes," *Proceeding of General Discussion of Heat Transfer*, pp. 20-26, 1951.

Chato, J.C., "Laminar condensation inside horizontal and inclined tubes," *ASHRAE Journal*, Vol. 4, pp. 52-60, 1962.

Cavallini, A. and R. Zecchin, "A dimensionless correlation for heat transfer in forced convective condensation," *Proceedings of the Fifth International Heat Transfer Conference*, Japan Society of Mechanical Engineers, Vol. 3, pp. 309-313, 1974.

Cavallini, A., D. Del Col, L. Doretti, G.A. Longo, and L. Rossetto, "A New Computational Procedure for Heat Transfer and Pressure Drop during Refrigerant Condensation Inside Enhanced Tubes," *Journal of Enhanced Heat Transfer*, Vol. 6, pp. 441-456, 1999.

Cavallini, A., G. Censi, D. Del Col, L. Doretti, G.A. Longo, and L. Rossetto, "In-Tube Condensation of Halogenated Refrigerants," *ASHRAE Transactions*, Vol. 108, Part 1, pp. 146-161, 2002.

Chen, M.M., "An analytical study of laminar film condensation. Part II: Single and multiple horizontal tubes," *Journal of Heat Transfer*, Vol. 83, 55-60, 1961.

Chen, S.L., F.M. Gerner, and C.L. Tien, "General film condensation correlations," *Experimental Heat Transfer*, Vol. 1, pp. 93-107, 1987.

Churchill, S.W., "Comprehensive correlating equations for heat, mass, and momentum transfer in fully developed flow in smooth tubes," *Ind. Eng. Chem. Fundam.*, 16, 109-116, 1977(b).

Colburn, A.P., "A method of correlating forced convection heat transfer data and a comparison with fluid friction," *AIChE Transactions*, 19, 174-210, 1933.

Dittus, F.W., and L.M.K. Boelter, "Heat transfer in automobile radiators of the tubular type," *University of California Publications on Engineering*, 2, 443-461, 1930.

Dobson, M.K., J.P. Wattelet, and J.C. Chato, "Heat Transfer and Flow Regimes During Condensation in Horizontal Tubes," ACRC TR-57, Air Conditioning and Refrigeration Center, University of Illinois Urbana-Champaign IL, 1994.

F-Chart Software, "Engineering Equation Solver (EES)," version 6.575. Computer Software. 2002.

Friedel, L., "Improved friction pressure drop correlations for horizontal and vertical two phase pipe flow," Paper E2, European Two Phase Flow Group Meeting, Ispara, Italy, 1979.

Gnielinski, V., "New equations for heat and mass transfer in turbulent pipe and channel flow," *International Chemical Engineering*, 16, 359-368, 1976.

Graham, D.M., H.R. Kopke, M.J. Wilson, D.A. Yashar, J.C. Chato, and T.A. Newell "An Investigation of Void Fraction in the Annular/Stratified Flow Regions in Smooth, Horizontal Tubes," ACRC TR-144, Air Conditioning and Refrigeration Center, University of Illinois Urbana-Champaign IL, 1998.

Hurlburt, E.T. and T.A. Newell, "Characteristics of Refrigerant Film Thickness, Pressure Drop, and Condensation Heat Transfer in Annular Flow," *HVAC&R Research*, Vol. 5, No. 3, pp. 229-247, 1999.

Incropera, F.P. and D.P. Dewitt, *Fundamentals of Heat and Mass Transfer*, 4th edition, Wiley, New York, 1996.

Jaster, H., and P.G. Kosky, "Condensation in a mixed flow regime," *International Journal of Heat and Mass Transfer,* Vol. 19, pp. 95-99, 1976.

Jung, D.S. and R. Radermacher, "Prediction of pressure drop during horizontal annular flow boiling of pure and mixed refrigerants," *International Journal of Heat and Mass Transfer,* 32, 2435-2466, 1989.

Kopke, H.R., T.A. Newell, and J.C. Chato, "Experimental Investigation of Void Fraction during Refrigerant Mixtures in Horizontal Tubes," ACRC TR-142, Air Conditioning and Refrigeration Center, University of Illinois Urbana-Champaign IL, 1998.

Kosky, P.G. and F.W. Staub, "Local condensing heat transfer coefficients in the annular flow regime," *AlChE Journal,* Vol. 17, No. 5, pp. 1037-1043, 1971.

Lockhart, R.W. and R.C. Martinelli, "Proposed correlation of data for isothermal two-phase, two-component flow in pipes," *Chemical Engineering Progress,* 45, 39-48, 1949.

Mandhane, J.M., G.A. Gregory, and K. Aziz, "A flow pattern map for gas-liquid flow in horizontal and inclined pipes," *International Journal of Multiphase Flow,* 1, 537-553, 1974.

Moffat, R.J., "Describing the uncertainties in experimental results," *Experimental Thermal and Fluid Science,* Vol. 1, pp. 3-17, 1988.

Nozu S., H. Katayama, H. Nakata, and H. Honda, "Condensation of refrigerant CFC11 in horizontal microfin tubes (Proposal of a correlation equation for frictional pressure gradient)," *Journal of Enhanced Heat Transfer,* Vol. 18, pp. 82-96, 1998.

Rice, C.K., "The effect of void fraction correlation and heat flux assumption on refrigerant charge inventory predictions," *ASHRAE Transactions,* Vol. 93, Part 1, pp. 341-367, 1987.

Rosson, H.F., and J.A. Myers, "Point values of condensing film coefficients inside a horizontal tube," *Chemical Engineering Progress Symposium Series,* Vol. 61(59), pp.190-199, 1965.

Shah, M.M., "A general correlation for heat transfer during film condensation inside pipes," *International Journal of Heat and Mass Transfer,* Vol. 22, pp. 547-556, 1979.

Souza, A.L., J.C. Chato, J.P. Wattlet, and B.R. Christoffersen, "Pressure drop during two-phase flow of pure refrigerants and refrigerant-oil mixtures in horizontal smooth tubes," ASME-HTD-Vol. 243, Heat Transfer With Alternative Refrigerants, 1993.

Soliman, H.M., J.R. Schuster, and P.J. Benson, "A general heat transfer correlation for annular flow condensation," *Journal of Heat Transfer,* Vol. 90, pp. 267-276, 1968.

Soliman, H.M., "On the annular-to-wavy flow pattern transition during condensation inside horizontal tubes," *The Canadian Journal of Chemical Engineering,* Vol. 60, pp. 475-481, 1982.

Taitel, Y., and A. E. Dukler, "A model for predicting flow regime transitions in horizontal and near horizontal gas-liquid flow," *American Institute of Chemical Engineering Journal,* Vol. 22(1), pp. 47-55, 1976.

Tang, L., "Empirical Study of New Refrigerant Flow Condensation Inside Horizontal Smooth Tube and Micro-Fin Tubes," Ph.D. Thesis, University of Maryland at College Park, 1997.

Thome, J.R., and J. El Hajal, "Two-Phase flow pattern for evaporation in horizontal tubes: latest version," *1st Int. Conf. On Heat Transfer, Fluid Mechanics, and Thermodynamics*, Kruger Park, South Africa, April 8-10, Vol. 1, pp. 182-188, 2002a.

Thome, J.R., A. Cavallini, and J. El Hajal, "Condensation in Horizontal Tubes Parts 1 and 2", to appear, *ASHRAE Transactions,* 2003.

Traviss, D.P., W.M. Rohsenow, and A.B. Baron, "Forced convective condensation in tubes: A heat transfer correlation for condenser design," *ASHRAE Transactions,* Vol. 79(1), pp. 157-165, 1973.

Wattelet, J.P., J.C. Chato, B.R. Christoffersen, J.A. Gaibel, M. Ponchner, P.J. Kenney, R.L. Shimon, T.C. Villanueva, N.L. Rhines, K.A. Sweeney, D.G. Allen, and T.T. Hershberger, "Heat Transfer Flow Regimes of Refrigerants in a Horizontal-Tube Evaporator," ACRC Technical Report 55, 1994

Wilson, M.J., T.A. Newell, and J.C. Chato, “Experimental Investigation of Void Fraction during Horizontal Flow in Larger Diameter Refrigeration Applications,” ACRC TR-140, Air Conditioning and Refrigeration Center, University of Illinois Urbana-Champaign IL, 1998.

Wilson, M.J., T.A. Newell, and J.C. Chato, “A Study of Two-Phase Refrigerant Behavior in Flattened Tubes,” ACRC CR-35, Air Conditioning and Refrigeration Center, University of Illinois Urbana-Champaign IL, 2001.

Yashar, D.A., M.J.Wilson, H.R. Kopke, D.M. Graham, J.C. Chato, and T.A. Newell, “Experimental Investigation of Void Fraction during Horizontal Flow in Smaller Diameter Refrigeration Applications,” ARCR TR-141, Air Conditioning and Refrigeration Center, University of Illinois Urbana-Champaign IL, 1998.

Zivi, S.M., “Estimation of steady-state steam void-fraction by means of the principle of minimum entropy production,” *Transactions ASME, Journal of Heat Transfer*, Series C, Vol. 86, May, pp. 247-252, 1964.

Appendix A. R22 Heat Transfer Data

The units used in this table are: G (kg/m^2-s), x_{in} (-), T_{sat} (ºC), h (kW/m^2-K), P_{red} (-).

Tube Profile	G	x	T_{sat}	h	P_{red}
Basic	153	0.31	33.2	1.6	0.26
Basic	156	0.43	34.6	1.7	0.27
Basic	160	0.56	36.0	2.0	0.28
Basic	144	0.76	36.1	2.2	0.28
Basic	148	0.91	35.6	2.3	0.28
Basic	251	0.16	34.3	1.7	0.27
Basic	237	0.28	32.8	1.9	0.26
Basic	244	0.43	35.0	2.3	0.27
Basic	236	0.60	34.7	2.5	0.27
Basic	221	0.69	33.0	2.6	0.26
Basic	225	0.87	34.0	2.7	0.27
Basic	222	0.89	33.1	2.7	0.26
Basic	402	0.17	34.6	1.6	0.27
Basic	406	0.23	35.8	2.0	0.28
Basic	403	0.34	35.0	2.3	0.27
Basic	397	0.45	35.6	2.7	0.28
Basic	398	0.54	34.9	2.8	0.27
Basic	400	0.65	35.3	3.1	0.27
Basic	401	0.75	37.5	3.4	0.29
Basic	397	0.88	41.1	4.2	0.32
Enhanced	164	0.63	34.7	1.3	0.27
Enhanced	156	0.78	35.1	1.3	0.27
Enhanced	147	0.98	35.7	1.5	0.28
Enhanced	164	0.27	35.1	0.6	0.27
Enhanced	152	0.38	35.3	0.6	0.27
Enhanced	155	0.44	35.8	0.8	0.28
Enhanced	149	0.57	35.3	1.0	0.27
Enhanced	223	0.08	36.5	1.2	0.28
Enhanced	231	0.26	34.9	0.7	0.27
Enhanced	227	0.36	35.8	1.1	0.28
Enhanced	222	0.38	35.6	1.0	0.28
Enhanced	241	0.47	34.8	1.3	0.27
Enhanced	223	0.68	36.0	1.4	0.28
Enhanced	222	0.76	34.7	2.0	0.27
Enhanced	229	0.98	34.0	1.9	0.27
Enhanced	238	0.25	34.0	0.8	0.27
Enhanced	237	0.35	35.2	1.0	0.27
Enhanced	216	0.51	35.4	1.2	0.28
Enhanced	215	0.59	35.2	1.3	0.27

Tube Profile	G	x	T_{sat}	h	P_{red}
Enhanced	216	0.72	34.9	1.5	0.27
Enhanced	228	0.85	35.1	1.4	0.27
Enhanced	403	0.16	35.7	0.9	0.28
Enhanced	407	0.26	35.3	1.1	0.27
Enhanced	394	0.36	35.2	1.2	0.27
Enhanced	404	0.44	34.9	1.2	0.27
Enhanced	410	0.52	34.9	1.2	0.27
Enhanced	397	0.63	35.4	1.2	0.27
Enhanced	393	0.69	35.3	1.3	0.27
Enhanced	394	0.75	37.1	1.4	0.29
Enhanced	404	0.84	39.9	1.4	0.31
Enhanced	410	0.19	35.6	1.0	0.28
Enhanced	400	0.30	36.3	1.1	0.28
Enhanced	418	0.41	35.2	1.2	0.27
Enhanced	419	0.56	36.2	1.2	0.28
Enhanced	415	0.70	35.8	1.4	0.28

Appendix B. Ammonia Heat Transfer Data

The units used in this table are: G (kg/m^2-s), x_{in} (-), T_{sat} (ºC), h (kW/m^2-K), P_{red} (-).

Set #	Tube Profile	G	x	T_{sat}	h	P_{red}
1	Basic	24	0.00	21.8	3.2	0.08
1	Basic	24	0.10	22.2	6.2	0.08
1	Basic	24	0.16	22.4	5.5	0.08
1	Basic	22	0.39	35.7	5.7	0.12
1	Basic	21	0.59	36.0	6.0	0.12
1	Basic	23	0.71	36.3	6.7	0.12
1	Basic	20	0.93	34.9	6.5	0.12
1	Basic	21	0.97	36.1	6.7	0.12
1	Basic	33	0.00	22.7	4.3	0.08
1	Basic	35	0.07	22.5	5.1	0.08
1	Basic	45	0.19	34.9	7.5	0.12
1	Basic	42	0.31	34.7	6.1	0.12
1	Basic	42	0.40	34.4	8.6	0.12
1	Basic	43	0.55	34.9	7.2	0.12
1	Basic	40	0.76	36.4	6.9	0.12
1	Basic	41	0.86	35.0	7.1	0.12
1	Basic	37	0.87	34.5	8.1	0.12
1	Basic	41	0.92	35.9	7.7	0.12
1	Basic	78	0.00	23.3	3.0	0.08
1	Basic	81	0.11	34.2	7.8	0.12
1	Basic	81	0.18	35.1	7.6	0.12
1	Basic	77	0.35	35.5	6.9	0.12
1	Basic	80	0.53	35.8	6.6	0.12
1	Basic	80	0.76	36.4	8.2	0.12
1	Basic	80	0.90	37.2	11.0	0.13
1	Basic	76	0.97	37.0	9.0	0.13
1	Basic	161	0.02	22.0	2.2	0.08
1	Basic	167	0.10	35.3	6.6	0.12
1	Basic	168	0.19	36.3	6.1	0.12
1	Basic	153	0.40	36.3	8.6	0.12
1	Basic	164	0.53	37.2	10.4	0.13
1	Basic	161	0.75	36.9	12.4	0.13
1	Basic	157	0.91	37.1	13.9	0.13
1	Basic	163	0.93	37.2	11.7	0.13
1	Basic	165	0.93	36.9	12.0	0.13
1	Basic	260	0.01	23.9	3.2	0.09
1	Basic	269	0.10	35.8	5.1	0.12
1	Basic	270	0.10	35.7	4.9	0.12
1	Basic	264	0.19	36.2	6.2	0.12
1	Basic	264	0.38	36.5	11.1	0.12

Set #	Tube Profile	G	x	T_{sat}	h	P_{red}
1	Basic	262	0.56	37.5	15.1	0.13
1	Basic	274	0.75	45.4	13.4	0.16
1	Basic	265	0.91	50.6	15.5	0.18
1	Basic	273	0.92	54.7	13.9	0.20
1	Enhanced	21	0.00	24.1	0.6	0.09
1	Enhanced	19	0.10	23.8	0.8	0.09
1	Enhanced	18	0.21	23.7	0.9	0.09
1	Enhanced	20	0.36	34.5	1.0	0.12
1	Enhanced	20	0.31	33.5	0.9	0.11
1	Enhanced	19	0.45	35.5	1.0	0.12
1	Enhanced	22	0.45	34.4	1.0	0.12
1	Enhanced	20	0.60	35.6	1.0	0.12
1	Enhanced	21	0.75	36.5	1.1	0.13
1	Enhanced	21	0.85	36.0	1.1	0.12
1	Enhanced	19	1.00	35.1	1.2	0.12
1	Enhanced	40	0.00	22.2	0.6	0.08
1	Enhanced	45	0.13	36.1	1.0	0.12
1	Enhanced	40	0.18	35.2	0.8	0.12
1	Enhanced	41	0.39	35.7	1.2	0.12
1	Enhanced	36	0.55	36.2	1.3	0.12
1	Enhanced	39	0.72	35.3	1.7	0.12
1	Enhanced	42	0.85	34.8	2.0	0.12
1	Enhanced	41	0.89	36.1	2.1	0.12
1	Enhanced	82	0.00	22.7	0.6	0.08
1	Enhanced	77	0.09	36.2	1.1	0.12
1	Enhanced	75	0.17	35.2	1.3	0.12
1	Enhanced	87	0.37	35.5	1.7	0.12
1	Enhanced	73	0.59	34.7	2.0	0.12
1	Enhanced	76	0.77	36.2	2.2	0.12
1	Enhanced	80	0.87	35.4	2.2	0.12
1	Enhanced	79	0.91	35.4	2.2	0.12
1	Enhanced	161	0.01	22.7	0.7	0.08
1	Enhanced	172	0.09	35.0	1.2	0.12
1	Enhanced	160	0.19	36.6	1.6	0.13
1	Enhanced	164	0.39	35.9	2.0	0.12
1	Enhanced	155	0.59	35.3	2.1	0.12
1	Enhanced	161	0.77	36.5	2.3	0.13
1	Enhanced	157	0.89	36.4	2.2	0.12
1	Enhanced	279	0.01	22.8	0.8	0.08
1	Enhanced	267	0.11	35.8	1.5	0.12
1	Enhanced	265	0.19	35.2	1.7	0.12
1	Enhanced	254	0.25	35.5	2.0	0.12
1	Enhanced	267	0.27	37.8	2.2	0.13
1	Enhanced	269	0.36	35.2	1.9	0.12
1	Enhanced	268	0.55	36.7	2.0	0.13
1	Enhanced	269	0.76	45.4	2.3	0.16
1	Enhanced	271	0.87	49.9	2.6	0.18
1	Enhanced	269	0.91	50.9	2.6	0.18
2	Basic	21	0.01	17.8	5.9	0.07
2	Basic	22	0.16	19.9	7.8	0.08

Set #	Tube Profile	G	x	T_{sat}	h	P_{red}
2	Basic	20	0.09	16.3	6.5	0.07
2	Basic	21	0.17	16.6	5.2	0.07
2	Basic	19	0.34	35.9	5.3	0.12
2	Basic	20	0.55	35.5	6.0	0.12
2	Basic	20	0.72	36.5	6.4	0.13
2	Basic	20	0.82	35.9	7.2	0.12
2	Basic	20	0.85	35.0	7.2	0.12
2	Basic	43	0.08	17.4	5.6	0.07
2	Basic	46	0.09	24.2	6.3	0.09
2	Basic	41	0.16	35.1	5.2	0.12
2	Basic	41	0.36	34.8	6.7	0.12
2	Basic	38	0.64	35.9	7.1	0.12
2	Basic	39	0.78	36.9	7.2	0.13
2	Basic	41	0.84	36.6	8.2	0.13
2	Basic	42	0.87	36.5	8.1	0.13
2	Basic	79	0.08	35.8	5.9	0.12
2	Basic	76	0.20	36.6	5.9	0.13
2	Basic	78	0.41	35.0	6.4	0.12
2	Basic	82	0.61	35.8	6.4	0.12
2	Basic	81	0.78	34.9	7.6	0.12
2	Basic	79	0.87	35.9	8.4	0.12
2	Basic	79	0.94	36.1	8.3	0.12
2	Basic	160	0.09	36.3	5.0	0.12
2	Basic	160	0.18	34.7	5.2	0.12
2	Basic	158	0.41	36.3	7.8	0.12
2	Basic	162	0.57	34.0	9.2	0.12
2	Basic	163	0.75	37.3	10.4	0.13
2	Basic	161	0.87	40.8	11.9	0.14
2	Basic	163	0.90	41.0	12.2	0.14
2	Basic	265	0.00	23.2	4.4	0.08
2	Basic	273	0.09	35.4	6.0	0.12
2	Basic	267	0.18	35.1	7.7	0.12
2	Basic	283	0.17	35.4	6.3	0.12
2	Basic	266	0.36	37.9	10.4	0.13
2	Basic	276	0.38	34.2	9.2	0.12
2	Basic	261	0.51	48.9	11.1	0.18
2	Basic	270	0.54	52.2	10.7	0.19
2	Basic	268	0.58	44.0	11.3	0.15
2	Basic	269	0.71	50.8	12.1	0.18
2	Enhanced	21	0.00	17.4	1.1	0.07
2	Enhanced	20	0.04	16.4	1.0	0.07
2	Enhanced	20	0.05	17.4	1.0	0.07
2	Enhanced	20	0.22	33.7	1.0	0.12
2	Enhanced	18	0.44	34.5	1.1	0.12
2	Enhanced	19	0.59	34.7	1.1	0.12
2	Enhanced	22	0.76	35.9	1.2	0.12
2	Enhanced	19	0.89	36.3	1.2	0.12
2	Enhanced	20	0.99	34.7	1.3	0.12
2	Enhanced	44	0.10	31.1	1.2	0.11
2	Enhanced	39	0.19	36.8	1.1	0.13

Set #	Tube Profile	G	x	T_{sat}	h	P_{red}
2	Enhanced	38	0.41	36.0	1.3	0.12
2	Enhanced	38	0.58	36.5	1.5	0.13
2	Enhanced	41	0.76	35.4	2.0	0.12
2	Enhanced	40	0.88	34.8	2.1	0.12
2	Enhanced	40	0.99	36.4	1.9	0.12
2	Enhanced	80	0.00	20.2	1.0	0.08
2	Enhanced	81	0.05	27.3	0.9	0.10
2	Enhanced	81	0.09	35.9	1.2	0.12
2	Enhanced	77	0.21	34.5	1.4	0.12
2	Enhanced	82	0.38	36.6	1.6	0.13
2	Enhanced	82	0.57	35.5	1.8	0.12
2	Enhanced	80	0.77	34.5	1.9	0.12
2	Enhanced	83	0.87	34.8	2.2	0.12
2	Enhanced	79	0.95	35.1	2.2	0.12
2	Enhanced	167	0.10	36.8	1.3	0.13
2	Enhanced	157	0.21	34.5	1.7	0.12
2	Enhanced	161	0.42	35.2	2.1	0.12
2	Enhanced	160	0.56	34.6	2.0	0.12
2	Enhanced	158	0.76	37.6	2.4	0.13
2	Enhanced	163	0.81	38.4	2.4	0.13
2	Enhanced	155	0.90	35.2	2.4	0.12
2	Enhanced	173	0.97	40.0	2.7	0.14
2	Enhanced	271	0.00	20.3	1.1	0.08
2	Enhanced	267	0.07	36.4	1.7	0.12
2	Enhanced	271	0.19	36.0	2.0	0.12
2	Enhanced	265	0.37	37.0	2.4	0.13
2	Enhanced	272	0.40	38.4	2.3	0.13
2	Enhanced	267	0.56	47.8	2.2	0.17
2	Enhanced	276	0.36	34.9	1.6	0.12
2	Enhanced	275	0.57	41.7	1.5	0.14
2	Enhanced	268	0.67	47.0	2.8	0.17
3	Basic	21	0.18	32.8	5.1	0.11
3	Basic	19	0.32	35.7	5.2	0.12
3	Basic	21	0.55	35.5	5.3	0.12
3	Basic	21	0.75	35.4	4.3	0.12
3	Basic	21	0.70	35.3	5.4	0.12
3	Basic	22	0.82	34.9	4.5	0.12
3	Basic	20	0.87	35.4	5.6	0.12
3	Basic	18	1.00	34.9	4.4	0.12
3	Basic	20	0.93	34.6	4.8	0.12
3	Basic	41	0.05	33.9	7.1	0.12
3	Basic	40	0.11	36.8	5.7	0.13
3	Basic	43	0.15	35.7	6.1	0.12
3	Basic	36	0.31	36.5	6.8	0.12
3	Basic	39	0.53	34.7	7.4	0.12
3	Basic	42	0.70	35.2	6.6	0.12
3	Basic	41	0.83	35.4	5.6	0.12
3	Basic	40	0.84	34.5	5.7	0.12
3	Basic	40	0.88	35.6	5.4	0.12
3	Basic	85	0.03	36.1	5.8	0.12

Set #	Tube Profile	G	x	T_{sat}	h	P_{red}
3	Basic	80	0.10	35.9	6.1	0.12
3	Basic	77	0.31	36.1	5.7	0.12
3	Basic	79	0.51	36.3	5.9	0.12
3	Basic	79	0.80	36.9	8.1	0.13
3	Basic	79	0.84	35.7	9.1	0.12
3	Basic	79	0.88	36.5	9.0	0.12
3	Basic	157	0.02	35.2	5.6	0.12
3	Basic	164	0.12	35.9	5.5	0.12
3	Basic	156	0.32	36.3	7.8	0.12
3	Basic	163	0.55	34.8	10.5	0.12
3	Basic	158	0.75	36.6	12.3	0.13
3	Basic	156	0.77	36.3	12.1	0.12
3	Basic	165	0.83	40.2	20.0	0.14
3	Basic	168	0.87	40.3	16.4	0.14
3	Basic	271	0.03	35.7	6.9	0.12
3	Basic	279	0.05	36.6	6.6	0.13
3	Basic	277	0.10	35.8	7.2	0.12
3	Basic	274	0.30	35.7	10.8	0.12
3	Basic	269	0.49	42.4	11.4	0.15
3	Enhanced	23	0.00	20.2	1.4	0.08
3	Enhanced	19	0.08	19.8	1.3	0.08
3	Enhanced	20	0.22	33.7	1.3	0.12
3	Enhanced	20	0.39	34.7	1.4	0.12
3	Enhanced	20	0.61	35.0	1.5	0.12
3	Enhanced	22	0.83	35.1	1.6	0.12
3	Enhanced	18	0.90	34.5	1.5	0.12
3	Enhanced	19	0.92	35.2	1.6	0.12
3	Enhanced	38	0.09	29.6	1.4	0.10
3	Enhanced	41	0.15	35.2	1.5	0.12
3	Enhanced	42	0.33	36.0	1.8	0.12
3	Enhanced	39	0.54	36.0	2.1	0.12
3	Enhanced	41	0.74	35.1	2.7	0.12
3	Enhanced	41	0.80	35.8	2.7	0.12
3	Enhanced	38	0.93	35.5	2.7	0.12
3	Enhanced	41	0.00	18.7	1.4	0.07
3	Enhanced	39	0.17	35.3	1.3	0.12
3	Enhanced	39	0.33	35.4	1.5	0.12
3	Enhanced	41	0.55	36.0	1.9	0.12
3	Enhanced	40	0.77	35.6	2.3	0.12
3	Enhanced	39	0.86	34.7	2.5	0.12
3	Enhanced	42	0.91	35.4	2.7	0.12
3	Enhanced	73	0.03	17.2	1.2	0.07
3	Enhanced	83	0.09	35.4	1.6	0.12
3	Enhanced	84	0.17	36.9	1.8	0.13
3	Enhanced	80	0.36	36.0	2.3	0.12
3	Enhanced	82	0.54	36.2	2.5	0.12
3	Enhanced	81	0.77	34.9	2.8	0.12
3	Enhanced	79	0.84	35.0	2.8	0.12
3	Enhanced	79	0.94	34.5	3.0	0.12
3	Enhanced	154	0.02	17.3	1.3	0.07

Set #	Tube Profile	G	x	T_{sat}	h	P_{red}
3	Enhanced	167	0.09	35.6	1.8	0.12
3	Enhanced	164	0.17	35.6	2.2	0.12
3	Enhanced	165	0.34	35.8	2.5	0.12
3	Enhanced	166	0.56	35.6	2.9	0.12
3	Enhanced	160	0.80	40.8	2.7	0.14
3	Enhanced	161	0.90	43.9	2.8	0.15
3	Enhanced	159	0.94	45.8	2.7	0.16
3	Enhanced	162	0.02	18.6	1.4	0.07
3	Enhanced	160	0.10	36.1	1.8	0.12
3	Enhanced	160	0.21	36.4	2.3	0.12
3	Enhanced	164	0.38	36.5	2.5	0.12
3	Enhanced	164	0.54	36.7	2.7	0.13
3	Enhanced	162	0.76	37.9	2.9	0.13
3	Enhanced	159	0.89	42.0	2.8	0.15
3	Enhanced	161	0.93	43.9	2.8	0.15
3	Enhanced	280	0.01	17.6	1.4	0.07
3	Enhanced	277	0.08	35.1	2.0	0.12
3	Enhanced	264	0.18	36.2	2.2	0.12
3	Enhanced	265	0.36	35.3	2.4	0.12
3	Enhanced	271	0.56	46.0	2.3	0.16
3	Enhanced	274	0.60	47.0	2.8	0.17
3	Enhanced	279	0.72	54.8	2.8	0.20

Appendix C. Ammonia Pressure Drop Data

The units used in this table are: G (kg/m^2-s), x_{in} (-), T_{sat} (ºC), dP_{raw} (kPa), $dP_{corrected}$ (kPa), P_{red} (-).

Set #	Tube Profile	G	x	T_{sat}	dPraw	$dP_{corrected}$	P_{red}
1	Basic	81	0.13	34.2	0.02	0.01	0.12
1	Basic	81	0.20	35.1	0.12	0.03	0.12
1	Basic	77	0.37	35.5	0.34	0.15	0.12
1	Basic	80	0.56	35.8	0.74	0.44	0.12
1	Basic	80	0.79	36.4	1.16	0.74	0.12
1	Basic	80	0.92	37.2	1.25	0.76	0.13
1	Basic	76	0.99	37.0	1.11	0.60	0.13
1	Basic	167	0.11	35.3	0.49	0.37	0.12
1	Basic	168	0.20	36.3	1.03	0.55	0.12
1	Basic	153	0.41	36.3	2.63	1.44	0.12
1	Basic	164	0.54	37.2	4.19	2.70	0.13
1	Basic	161	0.76	36.9	5.28	3.52	0.13
1	Basic	157	0.92	37.1	5.15	3.39	0.13
1	Basic	163	0.94	37.2	5.38	3.63	0.13
1	Basic	165	0.94	36.9	5.66	3.91	0.13
1	Basic	269	0.10	35.8	1.45	0.99	0.12
1	Basic	270	0.11	35.7	1.51	1.02	0.12
1	Basic	264	0.20	36.2	3.22	1.80	0.12
1	Basic	264	0.39	36.5	7.89	4.91	0.12
1	Basic	262	0.57	37.5	10.93	7.11	0.13
1	Basic	274	0.75	45.4	11.28	7.18	0.16
1	Basic	265	0.92	50.6	9.62	5.78	0.18
1	Basic	273	0.94	54.7	9.09	5.28	0.20
1	Enhanced	77	0.11	36.2	0.17	0.15	0.12
1	Enhanced	75	0.20	35.2	0.23	0.15	0.12
1	Enhanced	87	0.39	35.5	1.03	0.82	0.12
1	Enhanced	73	0.62	34.7	1.20	0.86	0.12
1	Enhanced	76	0.81	36.2	1.56	1.13	0.12
1	Enhanced	80	0.90	35.4	1.69	1.22	0.12
1	Enhanced	79	0.94	35.4	1.81	1.32	0.12
1	Enhanced	172	0.10	35.0	0.88	0.84	0.12
1	Enhanced	160	0.20	36.6	1.65	1.17	0.13
1	Enhanced	164	0.41	35.9	5.02	3.84	0.12
1	Enhanced	155	0.61	35.3	5.75	4.15	0.12
1	Enhanced	161	0.78	36.5	7.32	5.55	0.13
1	Enhanced	157	0.90	36.4	6.87	5.10	0.12
1	Enhanced	279	0.01	22.8	0.01	0.62	0.08
1	Enhanced	267	0.12	35.8	2.90	2.28	0.12
1	Enhanced	265	0.19	35.2	5.12	3.73	0.12

Set #	Tube Profile	G	x	T_{sat}	dPraw	$dP_{corrected}$	P_{red}
1	Enhanced	254	0.26	35.5	8.72	6.72	0.12
1	Enhanced	267	0.27	37.8	7.63	5.51	0.13
1	Enhanced	269	0.37	35.2	10.84	8.01	0.12
1	Enhanced	268	0.56	36.7	15.66	11.87	0.13
1	Enhanced	269	0.77	45.4	15.48	11.39	0.16
1	Enhanced	271	0.89	49.9	14.45	10.50	0.18
1	Enhanced	269	0.92	50.9	13.32	9.47	0.18
2	Basic	79	0.11	35.8	0.10	0.08	0.12
2	Basic	76	0.23	36.6	0.19	0.09	0.13
2	Basic	78	0.44	35.0	0.63	0.40	0.12
2	Basic	82	0.63	35.8	1.09	0.75	0.12
2	Basic	81	0.81	34.9	1.36	0.93	0.12
2	Basic	79	0.90	35.9	1.34	0.86	0.12
2	Basic	79	0.97	36.1	1.25	0.74	0.12
2	Basic	160	0.10	36.3	0.47	0.41	0.12
2	Basic	160	0.19	34.7	0.95	0.52	0.12
2	Basic	158	0.42	36.3	3.11	1.88	0.12
2	Basic	162	0.58	34.0	5.25	3.68	0.12
2	Basic	163	0.77	37.3	6.14	4.38	0.13
2	Basic	161	0.89	40.8	5.21	3.44	0.14
2	Basic	163	0.92	41.0	4.95	3.19	0.14
2	Basic	273	0.10	35.4	1.51	1.13	0.12
2	Basic	267	0.18	35.1	3.35	2.05	0.12
2	Basic	283	0.18	35.4	3.74	2.49	0.12
2	Basic	266	0.37	37.9	7.75	4.92	0.13
2	Basic	276	0.39	34.2	10.13	7.15	0.12
2	Basic	261	0.54	48.9	7.69	4.04	0.18
2	Basic	270	0.56	52.2	8.11	4.37	0.19
2	Basic	268	0.59	44.0	10.97	7.10	0.15
2	Basic	269	0.73	50.8	10.67	6.58	0.18
2	Enhanced	80	0.01	20.2	0.73	0.76	0.08
2	Enhanced	81	0.06	27.3	0.04	0.04	0.10
2	Enhanced	81	0.11	35.9	0.16	0.13	0.12
2	Enhanced	77	0.23	34.5	0.28	0.17	0.12
2	Enhanced	82	0.40	36.6	0.81	0.60	0.13
2	Enhanced	82	0.59	35.5	1.44	1.12	0.12
2	Enhanced	80	0.79	34.5	1.74	1.31	0.12
2	Enhanced	83	0.89	34.8	1.70	1.22	0.12
2	Enhanced	79	0.97	35.1	1.54	1.03	0.12
2	Enhanced	167	0.11	36.8	0.79	0.69	0.13
2	Enhanced	157	0.22	34.5	1.90	1.33	0.12
2	Enhanced	161	0.44	35.2	5.00	3.74	0.12
2	Enhanced	160	0.58	34.6	6.47	4.92	0.12
2	Enhanced	158	0.78	37.6	6.48	4.71	0.13
2	Enhanced	163	0.82	38.4	7.09	5.31	0.13
2	Enhanced	155	0.91	35.2	7.18	5.41	0.12
2	Enhanced	173	0.99	40.0	7.49	5.77	0.14
2	Enhanced	267	0.08	36.4	1.93	1.74	0.12
2	Enhanced	271	0.20	36.0	5.65	4.20	0.12
2	Enhanced	265	0.38	37.0	10.36	7.46	0.13

Set #	Tube Profile	G	x	T_{sat}	dPraw	$dP_{corrected}$	P_{red}
2	Enhanced	272	0.41	38.4	10.62	7.55	0.13
2	Enhanced	267	0.57	47.8	10.50	6.70	0.17
2	Enhanced	276	0.37	34.9	11.26	8.42	0.12
2	Enhanced	275	0.57	41.7	13.42	9.58	0.14
2	Enhanced	268	0.68	47.0	12.46	8.41	0.17
3	Basic	166	0.02	17.9	0.17	0.48	0.07
3	Basic	156	0.13	35.8	0.53	0.34	0.12
3	Basic	165	0.22	36.1	1.24	0.68	0.12
3	Basic	163	0.40	36.4	2.86	1.70	0.12
3	Basic	160	0.59	34.9	4.53	2.96	0.12
3	Basic	160	0.78	37.8	5.33	3.56	0.13
3	Basic	156	0.90	41.7	4.43	2.66	0.14
3	Basic	158	0.94	43.3	4.21	2.45	0.15
3	Basic	161	0.03	18.3	0.36	0.64	0.07
3	Basic	163	0.09	36.7	0.40	0.42	0.13
3	Basic	162	0.19	35.6	0.90	0.49	0.12
3	Basic	161	0.41	36.2	2.92	1.75	0.12
3	Basic	164	0.59	35.2	5.00	3.43	0.12
3	Basic	161	0.75	36.9	5.29	3.54	0.13
3	Basic	163	0.89	40.6	5.04	3.26	0.14
3	Basic	161	0.95	42.2	4.48	2.73	0.15
3	Basic	273	0.01	18.3	0.41	1.00	0.07
3	Basic	259	0.10	35.9	1.13	0.78	0.12
3	Basic	276	0.19	34.9	3.75	2.34	0.12
3	Basic	278	0.37	36.4	8.19	5.35	0.12
3	Basic	272	0.58	44.7	9.60	5.76	0.16
3	Basic	272	0.62	46.9	9.57	5.63	0.17
3	Basic	271	0.75	53.3	9.16	5.06	0.20
3	Enhanced	73	0.04	17.2	0.01	0.03	0.07
3	Enhanced	83	0.13	35.4	0.20	0.17	0.12
3	Enhanced	84	0.21	36.9	0.33	0.25	0.13
3	Enhanced	80	0.40	36.0	0.85	0.65	0.12
3	Enhanced	82	0.58	36.2	1.47	1.17	0.12
3	Enhanced	81	0.81	34.9	1.77	1.34	0.12
3	Enhanced	79	0.88	35.0	1.77	1.31	0.12
3	Enhanced	79	0.98	34.5	1.69	1.19	0.12
3	Enhanced	154	0.02	17.3	0.11	0.41	0.07
3	Enhanced	167	0.10	35.6	0.78	0.73	0.12
3	Enhanced	164	0.19	35.6	1.77	1.34	0.12
3	Enhanced	165	0.36	35.8	3.81	2.79	0.12
3	Enhanced	166	0.58	35.6	6.41	4.87	0.12
3	Enhanced	160	0.81	40.8	6.17	4.39	0.14
3	Enhanced	161	0.92	43.9	5.75	3.99	0.15
3	Enhanced	159	0.96	45.8	5.14	3.40	0.16
3	Enhanced	160	0.12	36.1	0.79	0.68	0.12
3	Enhanced	160	0.22	36.4	1.98	1.43	0.12
3	Enhanced	164	0.40	36.5	4.57	3.41	0.12
3	Enhanced	164	0.56	36.7	5.86	4.34	0.13
3	Enhanced	162	0.78	37.9	6.73	4.96	0.13
3	Enhanced	159	0.91	42.0	5.87	4.10	0.15

Set #	Tube Profile	G	x	T_{sat}	dPraw	$dP_{corrected}$	P_{red}
3	Enhanced	161	0.95	43.9	5.53	3.78	0.15
3	Enhanced	280	0.01	17.6	0.58	1.17	0.07
3	Enhanced	277	0.09	35.1	2.23	1.97	0.12
3	Enhanced	264	0.19	36.2	4.89	3.56	0.12
3	Enhanced	265	0.37	35.3	10.48	7.67	0.12
3	Enhanced	271	0.58	46.0	12.88	9.06	0.16
3	Enhanced	274	0.62	47.0	13.25	9.32	0.17
3	Enhanced	279	0.74	54.8	12.73	8.63	0.20